UNIVERISTY OF BELGRADE
FACULTY OF TECHNOLOGY AND METALLURGY

Houda Ali Madani Gamoudi

SYNTHESIS AND CHARACTERIZATION OF DENTAL COMPOSITE IMPLANTS WITH ZIRCONIUM-BASED REINFORCEMENTS

Doctoral Dissertation

Belgrade, 2026

UNIVERZITET U BEOGRADU
TEHNOLOŠKO METALURŠKI FAKULTET

Houda Ali Madani Gamoudi

SINTEZA I KARAKTERIZACIJA DENTALNIH KOMPOZITNIH IMPLANTATA SA OJAČANJIMA NA BAZI CIRKONIJUMA

Doktorska Disertacija

Beograd, 2026

Supervisors

Dr Vesna Radojević, full professor, University of Belgrade
Faculty of Technology and Metallurgy

Dr Ivana Stajčić, Associate Research Professor, University of Belgrade
Vinča Nuclear Institute

Member of Committes

Dr Petar Uskoković, associate professor, University of Belgrade
Faculty of Technology and Metallurgy

Dr Dušica Stojanović, Associate Research Professor, University of Belgrade
Faculty of Technology and Metallurgy

Dr Miloš Petrović, AssociateProfessor, University of Belgrade
Faculty of Technology and Metallurgy

Dr Aleksandar Kojović, associate professor, University of Belgrade
Faculty of Technology and Metallurgy

Dr Aleksandar Stajčić, Associate Research Professor, University of Belgrade,
Institute of Chemistry, Technology and Metallurgy

Date:_____

Candidate:

Houda Ali Madani Gamoudi

ACKNOWLEDGEMENTS

I am deeply grateful to everyone who supported me throughout this work. My sincere thanks go to my supervisor, Prof. Dr. Vesna Radojević, for her generous support and guidance.

I am especially indebted to my co-advisor, Dr. Ivana Stajčić of the Vinča Nuclear Institute, University of Belgrade, whose enthusiasm for research and persistent help were essential to the completion of this dissertation. It has been an honor to be their PhD student.

I also thank the other members of my committee, Prof. Dr. Petar Uskoković and Dr. Dušica Stojanović, for their interest in my research and for their valuable suggestions and comments.

My appreciation extends to Prof. Dr. Miloš Petrović, Prof. Dr. Aleksandar Kojović, and the teaching staff of the Faculty of Materials Science and Engineering, University of Belgrade, whose broad expertise helped me progress and complete my studies.

I was fortunate to work with Dr. Aleksandar Stajčić, who patiently taught me numerous laboratory techniques and assisted with analyses.

Finally, I thank all colleagues and collaborators not already mentioned for creating a friendly, cooperative environment and for their helpful feedback and encouragement.

SUMMARY

Synthesis and characterization of dental composite implants with zirconium-based reinforcements

The development of advanced polymer-based composites for dental and biomedical applications requires a careful balance between mechanical performance, thermal stability, and biological compatibility. Polyetherimide (PEI), as a high-performance thermoplastic polymer, offers excellent thermal and chemical resistance, but its mechanical properties can be further enhanced through the incorporation of engineered ceramic reinforcements. In this doctoral thesis, two distinct reinforcement strategies were investigated: high-aspect-ratio zirconia (ZrO_2) nanofibers and nanostructured $BaZrO_3/Y_2O_3/SrTiO_3$ hybrid ceramic particles. The research aimed to establish structure-property relationships by comparing the influence of reinforcement morphology, dispersion state, and interfacial interactions on the performance of PEI-based composites. Zirconia nanofibers were fabricated via electrospinning followed by calcination, and subsequently fragmented into whisker-like structures through ultrasonication to improve dispersion. $BaZrO_3/Y_2O_3/SrTiO_3$ particles were synthesized through mechanochemical processing, resulting in submicron agglomerates composed of nanoscale crystallites with defect-modified perovskite structure. Composite films were prepared using solution-based methods with controlled filler content, and their properties were evaluated using field-emission scanning electron microscopy (FESEM), X-ray diffraction (XRD), Fourier transform infrared spectroscopy (FTIR), differential scanning calorimetry (DSC), microindentation and nanoscratch testing, UV-vis spectroscopy, and in vitro cytotoxicity assays. The results demonstrate that reinforcement morphology plays a critical role in determining composite performance. ZrO_2 whisker-like structures provided superior mechanical reinforcement, achieving hardness improvements exceeding 140% due to efficient stress transfer and high aspect ratio. $BaZrO_3/Y_2O_3/SrTiO_3$-reinforced composites also exhibited significant enhancements (up to ~83%), governed by particle dispersion and interfacial constraint effects. Both reinforcement systems increased the glass transition temperature, indicating restricted polymer chain mobility, although a saturation effect was observed at higher filler loadings. Microstructural analysis revealed that optimal performance is achieved when fillers are well dispersed, while excessive agglomeration reduces reinforcement efficiency. Optical transparency decreased with increasing filler content due to light scattering. Cytotoxicity evaluation showed a concentration-dependent response, with full recovery of cell viability upon dilution, confirming the cytocompatibility of the composites under realistic conditions.

This thesis demonstrates that the properties of PEI-based composites are governed by a complex interplay between reinforcement morphology, dispersion quality and interfacial interactions. The comparative analysis of nanofiber and hybrid nanoparticle systems provides valuable insight into the design of multifunctional polymer composites, contributing to the development of next-generation materials for dental and biomedical applications.

Keywords: PEI, nanoparticles, ceramic nanofibers, mechanical properties

Field of Academic Expertise:

UDC:

REZIME

Sinteza i karakterizacija dentalnih kompozitnih implantata sa ojačanjima na bazi cirkonijuma

Razvoj naprednih polimernih kompozita za stomatološke i biomedicinske primene zahteva pažljivo usklađivanje mehaničkih svojstava, termičke stabilnosti i biološke kompatibilnosti. Polieterimid (PEI), kao termoplastični polimer visokih performansi, poseduje izuzetnu termičku i hemijsku otpornost, ali se njegova mehanička svojstva mogu dodatno unaprediti uvođenjem inženjerski dizajniranih keramičkih ojačanja. U okviru ove doktorske disertacije istražene su dve različite strategije ojačanja: nanovlakna cirkonijum-dioksida (ZrO_2) sa visokim odnosom dužine i prečnika, i nanostrukturisane hibridne keramičke čestice $BaZrO_3/Y_2O_3/SrTiO_3$. Cilj istraživanja bio je uspostavljanje odnosa struktura-svojstva kroz poređenje uticaja morfologije ojačanja, stanja disperzije i međufaznih interakcija na performanse kompozita na bazi PEI. Nanovlakna cirkonijuma dobijena su tehnikom elektropredenja, nakon čega su kalcinisana, a zatim fragmentisana u strukture nalik viskerima ultrazvučnom obradom radi poboljšanja disperzije. Čestice $BaZrO_3/Y_2O_3/SrTiO_3$ sintetisane su mehanokemijskom obradom, pri čemu su formirani submikronski aglomerati sastavljeni od nanokristalita sa perovskitnom strukturom modifikovanom defektima. Kompozitni filmovi pripremljeni su metodama iz rastvora sa kontrolisanim sadržajem punila, a njihova svojstva ispitivana su pomoću skenirajuće elektronske mikroskopije sa iz emisijom polja (FESEM), rendgenske difrakcije (XRD), infracrvene spektroskopije sa Furijeovom transformacijom (FTIR), diferencijalne skenirajuće kalorimetrije (DSC), mikroindentacije i nanoscratch testova, UV-vis spektroskopije, kao i *in vitro* citotoksičnih ispitivanja. Rezultati pokazuju da morfologija ojačanja ima ključnu ulogu u određivanju performansi kompozita. Strukture nalik viskerima na bazi ZrO_2 obezbedile su superiorno mehaničko ojačanje, sa povećanjem tvrdoće većim od 140%, zahvaljujući efikasnom prenosu naprezanja i visokom odnosu dužine i prečnika. Kompoziti ojačani $BaZrO_3/Y_2O_3/SrTiO_3$ česticama takođe su pokazali značajna poboljšanja (do ~83%), pri čemu su dominantni faktori bili disperzija čestica i efekti međufaznog ograničenja pokretljivosti lanaca. Oba sistema ojačanja dovela su do povećanja temperature staklastog prelaza, što ukazuje na smanjenu pokretljivost polimernih lanaca, pri čemu je uočen efekat zasićenja pri većim udelima ojačanja. Mikrostrukturna analiza pokazala je da se optimalne performanse postižu pri dobroj disperziji ojačanja, dok prekomerna aglomeracija njihovu smanjuje efikasnost. Optička transparentnost opada sa povećanjem sadržaja punila usled rasipanja svetlosti. Ispitivanja citotoksičnosti pokazala su zavisnost od koncentracije, uz potpuni oporavak vijabilnosti ćelija nakon razblaženja, čime je potvrđena citokompatibilnost kompozita u realnim uslovima.

Ova disertacija pokazuje da su svojstva kompozita na bazi PEI određena složenom međuzavisnošću morfologije ojačanja, kvaliteta disperzije i međufaznih interakcija. Komparativna analiza sistema zasnovanih na nanovlaknima i hibridnim nanočesticama pruža značajan uvid u projektovanje multifunkcionalnih polimernih kompozita, doprinoseći razvoju materijala nove generacije za stomatološke i biomedicinske primene.

Ključne reči: PEI, nanočestice, keramička nanovlakna, mehanička svojstva

Naučna oblast: Tehnološko inženjerstvo: Nauka o materijalima i inženjerstvo materijala

UDC:

Contents

1. INTRODUCTION

Dental composite implants represent an important field within dental research and development [1]. Zirconia nanofibers have garnered considerable interest as a reinforcement material for these implants, owing to their remarkable mechanical properties and biocompatibility. This research focuses on developing and analyzing dental composite implants reinforced with zirconia nanofibers, aiming to improve their mechanical strength and longevity, while ensuring they meet key biocompatibility criteria for effective use in the oral environment. The synthesis process entails integrating zirconia nanofibers into the dental composite matrix using sophisticated techniques to achieve uniform dispersion and optimal interfacial bonding. Subsequent comprehensive characterization assesses the mechanical, chemical, and biological attributes of the reinforced implants. The findings from this research hold significant potential for advancing dental implant materials, thereby improving clinical outcomes and patient satisfaction. This thesis explores the principal methods and experimental procedures employed for synthesizing zirconia-reinforced dental composite implants, offering insights into the intricate processes involved in optimizing composition and structural integrity. In contemporary dentistry, dental implants are essential for replacing lost teeth and regaining both function and aesthetics in the mouth [2]. But a major factor in their success is the materials used in their construction. Due to the strength, durability, and biocompatibility limits of traditional dental implant materials, research into substitute materials and manufacturing techniques has been spurred [3]. Zirconia nanofibers have emerged as a promising reinforcement material for dental composites due to their outstanding mechanical properties, including high strength and toughness, alongside their essential biocompatibility for long-term implant viability. Integrating zirconia nanofibers into the dental composite matrix presents an opportunity to augment load-bearing capacity and resilience while ensuring compatibility with surrounding oral tissues. This study aims to address the existing challenges in dental implant materials by focusing on the synthesis and characterization of zirconia-reinforced dental composite implants. By systematically exploring the synthesis process and evaluating the properties of the resulting implants, this research seeks to contribute to the advancement of dental implant technology, ultimately benefiting both dental practitioners and patients. The process of creating zirconia-reinforced dental composite implants involves a number of complex steps that require close supervision of the placement and alignment of nanofibers in the composite matrix. In order to achieve the required mechanical performance and biocompatibility of the implants, it is essential to comprehend and optimise these processes. Beginning with the synthesis of zirconia nanofibers for reinforcement purposes, recent advancements in nanofabrication technologies have facilitated the production of zirconia nanofibers with exceptional mechanical properties and biocompatibility. These nanofibers can be synthesized using various techniques such as electrospinning or sol-gel methods, enabling precise control over fiber morphology and composition. Additionally, integrating these zirconia nanofibers into the dental composite matrix requires careful consideration of factors such as fiber dispersion, orientation and bonding with the matrix material. To address these challenges, researchers have proposed various approaches, including surface modification of zirconia nanofibers to enhance their compatibility with the composite matrix and optimize the fiber-matrix interface [1]. Furthermore, recent developments in materials science suggest that reinforcement based on a single ceramic phase may not be sufficient to fully optimize composite performance. Increasing attention has been directed toward hybrid and multicomponent oxide systems, which enable additional control over structural and interfacial

properties. Among these, perovskite-type oxides and rare-earth-modified ceramic systems are of particular interest due to their structural flexibility, defect tolerance, and ability to accommodate multiple cation substitutions. Hybrid oxide systems based on $BaZrO_3$, Y_2O_3 and $SrTiO_3$ combine several advantageous characteristics. $BaZrO_3$ contributes chemical and structural stability, $SrTiO_3$ introduces functional versatility associated with dielectric and lattice-responsive behavior, while Y_2O_3 plays a role in defect engineering and structural modification. When these oxides are subjected to mechanochemical processing, they form nanostructured ceramic agglomerates composed of nanoscale crystallites, resulting in a hierarchical morphology that differs significantly from conventional single-phase fillers. Such systems provide not only stiffness enhancement, but also improved interfacial interaction through defect-assisted mechanisms and increased surface activity. Despite these promising features, the incorporation of hybrid oxide systems into high-performance polymer matrices remains insufficiently explored. In particular, a systematic comparison between fiber-based reinforcement (high-aspect-ratio nanofibers) and particle-based hierarchical ceramic agglomerates within the same polymer system is largely absent in the literature. Understanding how reinforcement morphology and composition influence structure-property relationships is therefore essential for the rational design of next-generation composite materials. Accordingly, this thesis investigates two fundamentally different reinforcement strategies within a polyetherimide matrix: zirconia nanofibers, representing anisotropic, high-aspect-ratio reinforcement, and mechanochemically synthesized $BaZrO_3/Y_2O_3/SrTiO_3$ hybrid ceramic particles, representing hierarchical, defect-engineered reinforcement systems. By comparing these approaches, the present work aims to establish how reinforcement dimensionality, dispersion state, and interfacial interactions govern the thermal, mechanical, and functional behavior of polymer-based composites. Therefore, this thesis aims to provide important insights into designing and producing advanced composites specifically optimized for biomedical applications in addition to developing a novel dental implant material.

The following important topics will be covered in this examination in order to meet thesis goal:

- The process of creating zirconia nanofibers and incorporating them into the dental composite matrix.
- Evaluating the mechanical properties and biocompatibility of dental composite implants enhanced with zirconia reinforcement.
- Examining how zirconia-reinforced dental composite implants perform in comparison to current dental implant materials.
- The synthesis of $BaZrO_3/Y_2O_3/SrTiO_3$ hybrid ceramic particles via mechanochemical processing and their incorporation into the dental composite matrix.
- Evaluating the influence of $BaZrO_3/Y_2O_3/SrTiO_3$ nanoparticle reinforcement on the mechanical properties and biocompatibility of PEI-based dental composite systems.
- Investigating the effect of hierarchical particle morphology, dispersion state, and interfacial interactions on the performance of $BaZrO_3/Y_2O_3/SrTiO_3$-reinforced composites in comparison to zirconia nanofiber-reinforced systems and conventional dental materials.

A variety of characterization methods will be used to assess the mechanical characteristics and biocompatibility of dental composite implants reinforced with zirconia. In order to evaluate mechanical strength, stiffness, and toughness, these methods may include tensile testing, compression testing, and flexural testing. In addition, the microstructure of the implants will be examined using transmission and scanning electron microscopy to ascertain the placement and alignment of zirconia nanofibers inside the composite matrix. Furthermore, biocompatibility assessments, including cell adhesion studies and viability assays, will be carried out to evaluate the relationship between implant materials and living tissues [2].

Furthermore, the potential clinical applications and advantages of zirconia-reinforced dental composite implants will be evaluated. This assessment will involve considering factors such as implant stability and longevity, aesthetic appearance, and ability to promote osseointegration while preventing bacterial colonization. Achieving effective synthesis and characterization of dental composite implants with nanofiber and nanoparticles reinforcement requires precise control of morphology and surface properties. This entails utilizing techniques like electrospinning or sol-gel methods to produce nanofibers with desired properties. Moreover, achieving uniform dispersion of zirconia nanofibers throughout the composite matrix is essential for maximizing both mechanical strength and biocompatibility. Thorough characterization of the resulting implants is essential to assess their mechanical properties, biocompatibility and potential application.

The Theoretical part provides literature background necessary for understanding the experimental work. It introduces the structure and function of dental materials, discusses the limitations of conventional systems, and presents the principles of polymer composites with emphasis on reinforcement mechanisms. Particular attention is given to zirconia-based nanofibers and hybrid oxide systems, including their synthesis, structural characteristics, and potential role in polymer reinforcement.

The Experimental chapter describes the materials, synthesis procedures, and composite fabrication methods used in this study. Zirconia nanofibers are produced via electrospinning and subsequent calcination, while $BaZrO_3/Y_2O_3/SrTiO_3$ particles are obtained through mechanochemical processing. Composite films are prepared using solution-based techniques, and the influence of reinforcement type and content on material behavior is systematically investigated.

The Results and Discussion chapter presents a comprehensive analysis of the obtained materials, focusing on structure-property relationships. Morphological characterization is performed using electron microscopy, structural properties are evaluated by X-ray diffraction and infrared spectroscopy, thermal behavior is analyzed using differential scanning calorimetry, and mechanical performance is assessed through microindentation techniques. Optical and biological properties are also examined to provide a complete evaluation of material performance.

The Conclusion summarizes the main findings of the thesis, identifies the most effective reinforcement strategies, and highlights the implications of the results for the design of advanced polymer composites. Future research directions are also proposed, particularly in relation to improving dispersion control, optimizing interfacial interactions, and extending the application of hybrid ceramic systems in biomedical and dental materials.

2. THEORETICAL PART

2.1. Composite materials

Materials are the foundation of all manufacturing industries; they include a wide variety of materials such as alloys, composites, and pure metals. Composite materials have become the preferable option, as pure metals are limited in their ability to match modern product requirements [3]. Because of their promising properties, including high specific resistance, strong damping capacity, and enhanced specific modulus, these materials are widely used in both conventional and non-traditional production techniques. Fibers were initially used as reinforcement in the 1940s, which is when composite materials were first developed [4]. Since then, there has been a noticeable development in composite materials, which are distinguished by their multiphase nature and consist of two or more components with separate properties. Reinforcement and matrices are the basic building blocks of all composite materials, as seen in Figure 1. Composites are used in many different fields because of their lightweight characteristics, high strength-to-weight ratio, wear resistance, and capacity to support large loads [5].

Figure 1. Constituents of a composite.

By mixing two or more components, new materials are created that have entirely different properties from the original ones. These novel materials are referred to as composites. Composite materials have become increasingly prevalent across numerous industries. In essence, composites consist of one or more continuous processes integrated into a single, coherent process. This integration makes it possible to manufacture materials with particular properties that can endure the rigorous requirements of modern applications. Composites are versatile and perform well in a variety of application scenarios, such as enhancing the structural integrity of aviation components, enabling complex medical implants, or providing strong yet lightweight solutions for the automobile industry. Composites enable the development of creative solutions that push the boundaries of engineering and design by utilizing the complimentary properties of their constituent materials. Composites play a critical role in shaping the technologies of the future, from improving patient outcomes in medical operations to maximizing aviation fuel efficiency [3].

2.1.1. Classification of composite materials

Composites are categorized according to a number of factors as shown in Figure 2. The matrix functions as a binder, holding the reinforcing material together, giving it shape, and protecting it from environmental and mechanical degradation. A general overview of composites categorized by matrix material:

- Polymer Matrix Composites (PMCs)
- Ceramic Matrix Composites (CMCs)
- Metal Matrix Composites (MMCs)
- Carbon Matrix Composites (CAMCs)

Composites can be particle- or fiber-reinforced, depending on the type of reinforcement used. As a result, the shape of the scattered phase particles distinguishes the first two groups the most. Particulate particles are typically spherical in shape, but fiber-type particles have an irregular geometry but a higher length-to-diameter ratio, similar to natural fibers [6].

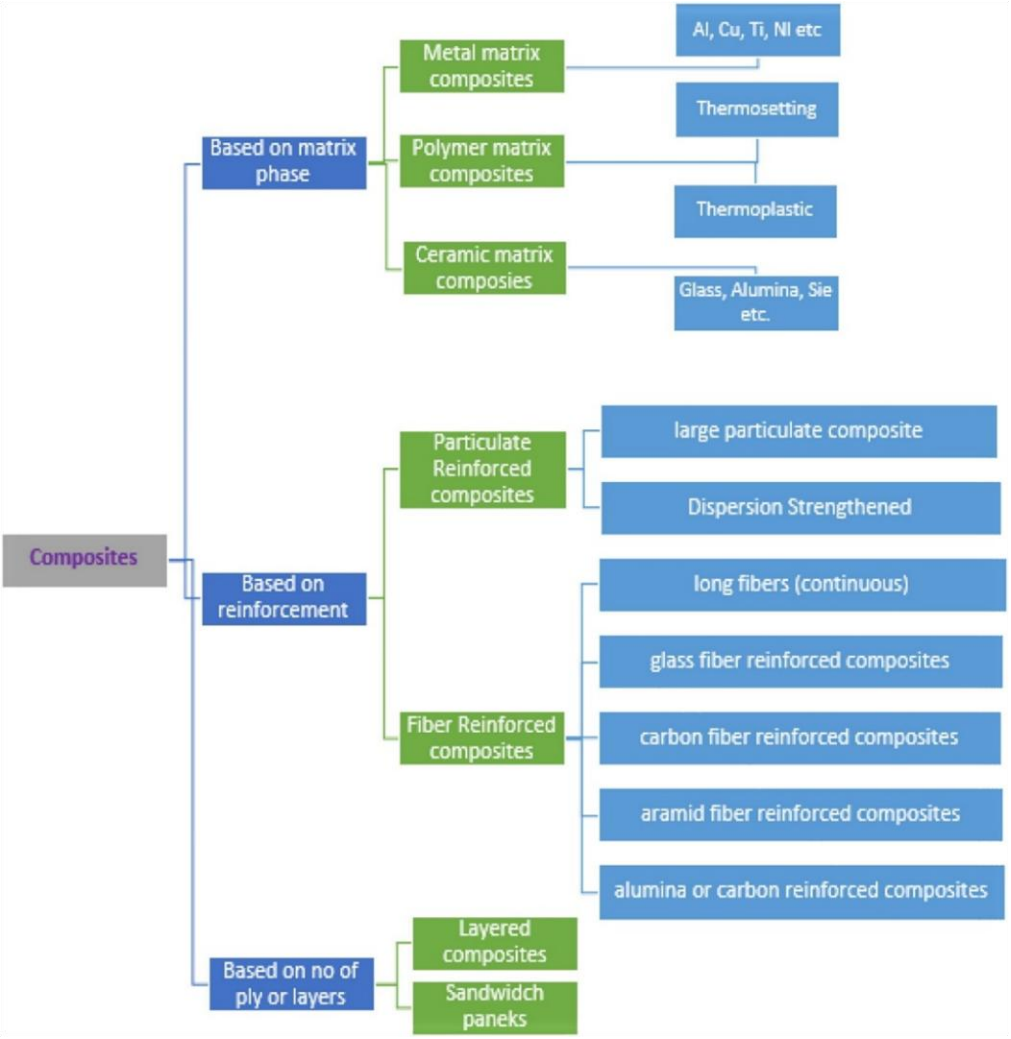

Figure 2. Classification according to their component parts [5]

Polymer Matrix Composites (PMC) - are a large class of composite materials made up of a polymer resin matrix reinforced by fibers or other reinforcing elements. These composites are widely employed in a variety of industries due to their lightweight, high strength, and customizability. The polymer matrix binds the reinforcing elements, maintaining the

composite's shape and structural stability while shielding it from mechanical stress and environmental damage.

There are various polymer matrices that can be used in composite materials. Thermoset matrix composites outnumber thermoplastic composites in terms of polymer matrix composition. Thermosets and thermoplastics may sound similar, but they have quite different characteristics and applications. Understanding performance differences can help to improve sourcing decisions and composite product design [7].

1) When thermoset resins are heated or given chemical additives, they become permanently cured. They cannot be melted or changed after they have set. The thermoset resins most often used are [7]:

- ✓ Epoxy is well-renowned for its remarkable mechanical and adhesive properties. It is commonly found in cars, airplanes, and sports equipment.
- ✓ Because of its exceptional mechanical properties and affordable price, polyester is a widely used material in the building, automotive, and marine industries.
- ✓ When used in harsh environments, vinyl ester offers a greater chemical resistance over polyester and an excellent balance between cost and performance.

2) Thermoplastic polymers differ from thermosetting materials in that they can be melted and reformed, offering benefits in recyclability and the ability to reshape the material. Notable examples include:

- ✓ Polypropylene (PP): Renowned for its durability and flexibility.
- ✓ Polyethylene (PE): Valued for its chemical resistance and wide range of applications.
- ✓ Polyamide (Nylon): Known for its superior strength and resistance to high temperatures.

Advanced materials known as Ceramic Matrix Composites (CMC) are made of high-performance fibres bonded to a ceramic matrix. These composites are perfect for demanding applications in a range of sectors because of their exceptional mechanical, thermal, and chemical properties.

CMCs are resistant to high temperatures and adverse environments because of their ceramic matrix, which guarantees structural integrity and thermal stability. The most widely used ceramic matrix components are [8]:

- ✓ The exceptional heat conductivity, high strength, and resistance to oxidation and corrosion of silicon carbide (SiC) are well recognized.
- ✓ High stiffness, electrical insulation, and resistance to wear and corrosion are well-known properties of alumina (Al_2O_3).
- ✓ The properties of zirconia (ZrO_2) include great hardness, resistance to heat shock, and biocompatibility is known for its high hardness, thermal shock resistance, and biocompatibility.

Metal Matrix Composites (MMC) - are advanced materials made up of a metal matrix with reinforcing components like fibers, particles, or whiskers. These composites combine metal ductility and toughness with the reinforcing phase's high strength, stiffness, and wear resistance, resulting in improved mechanical and thermal qualities over traditional metals and alloys [9].

2.1.2. Polymers in dental composites

The inception of dental composites dates back to the mid-1950s, when formulations consisting of dual monomers and macro-sized silicate particles were introduced to enhance mechanical performance [10]. Subsequent breakthroughs in micro- and nano-manufacturing have enabled the synthesis of highly defined fillers with diverse morphologies, including rods, tubes, fibers, and hollow spheres, allowing for the development of multi-functional composite systems (Figure 3). To optimize the mechanical integrity of these materials, physical or chemical surface modifications are applied to the fillers, which improves their dispersion within the resin matrix and strengthens interfacial adhesion [11]. Over the last decade, there has been a growing emphasis on bioactive composites capable of facilitating the remineralization of early caries[12] and providing antibacterial functionality [13]. Consequently, a comprehensive understanding of each constituent's properties is vital for establishing design and processing frameworks that elevate the overall quality of modern dental restorative materials.

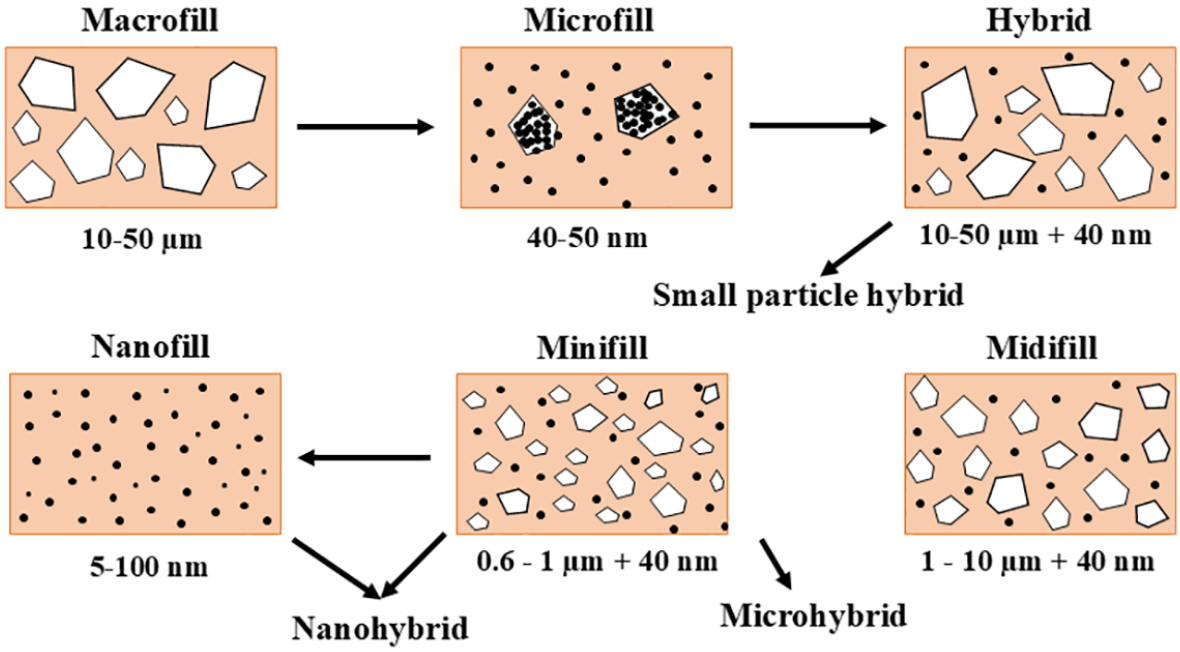

Figure 3. Dental Composite Types Grouped by Filler Particle Dimensions [14]

Macro-filled composites, often referred to as traditional or conventional types, are characterized by inorganic filler particles with dimensions exceeding 1 µm. These fillers are generally integrated into a BisGMA/TEGDMA resin matrix at a volume concentration of approximately 55–65% to form a workable paste. Upon completion of chemical polymerization, these materials typically exhibit flexural strength values between 110 and 135 MPa[15].

The addition of these macro-fillers provides substantial improvements over unfilled acrylics, particularly regarding hardness, elastic modulus, and compressive strength; furthermore, they help mitigate thermal expansion and polymerization shrinkage [16]. Despite these benefits, larger filler sizes introduce several drawbacks. The interfacial tension between the resin and the filler can lead to crack propagation and particle loss, resulting in poor wear

resistance and a surface that is difficult to polish. Moreover, the inherent surface roughness of these composites often leads to premature staining and yellowing. Commonly utilized fillers for these applications include ground quartz, strontium, and barium-containing heavy metal glasses [17].

Micro-filled resin composites composites were developed to address the limitations of macro-filled systems, specifically focusing on the aesthetic demand for high polishability. These materials are characterized by the use of ultra-fine particles, such as amorphous spherical silica, which typically measure approximately 40 nm. While these fillers significantly alter polymer rheology by increasing viscosity, their high specific surface area restricts the maximum filler loading, leading to a higher resin-to-filler ratio. Consequently, when compared to their macro-filled counterparts, micro-filled composites exhibit increased water sorption, a higher coefficient of thermal expansion, and a diminished elastic modulus. Furthermore, they are characterized by lower stiffness, reduced fatigue strength, and inferior fracture resistance [18].

To mitigate these drawbacks, pre-polymerized fillers (PPRF) were introduced. These larger filler complexes consist of ground, cured composite containing various submicron particles, which effectively increases the overall filler volume fraction. The integration of PPRF improves the material's polishability and minimizes polymerization shrinkage relative to traditional formulations. However, a significant disadvantage of PPRF is the lack of active binding sites for surface coupling; this results in weakened interfacial bonding with the surrounding resin matrix, ultimately compromising the composite's mechanical integrity [19].

Hybrid resin composites utilize a combination of micro- and nano-fillers to integrate the advantages of both particle sizes. Developed to mitigate the finishing difficulties, mechanical weaknesses, and significant shrinkage characteristic of macro-filled systems [16], early hybrid formulations typically paired large particles (10–50 μm) with 40 nm colloidal silica. These "universal" composites bridge the gap between aesthetics and durability; the smaller fillers provide the optical translucency and polishability required for anterior restorations, while the larger particles ensure the mechanical strength necessary for posterior load-bearing fillings. Despite their versatility, hybrid composites generally do not achieve the same level of long-term surface quality or translucency as micro-filled resins [14].

Nanocomposites represent a more recent advancement, featuring filler particles ranging from 5 to 100 nm, often organized into larger "nanoclusters" alongside particles sized between 0.6 and 1.4 μm [20]. These materials exhibit superior polishability, exceptional surface smoothness, and high translucency compared to traditional systems. The nanocluster architecture provides unique reinforcement, resulting in a significant increase in strength relative to micro-filled or standard nanohybrid systems. Consequently, nanocomposites are suitable for both aesthetic and high-stress applications, as they maintain the mechanical, physical, and wear-resistant attributes of hybrid composites [21].

The inclusion of fillers within the polymer matrix fundamentally enhances the tensile strength, elastic modulus, and fracture toughness of the material. Particle size is a critical factor influencing these mechanical properties, particularly fracture toughness. Fillers strengthen dental restoratives by obstructing crack propagation through several micromechanical processes, including crack deflection, crack bridging, matrix–filler interactions, and pinning/bowing mechanisms [22].

2.1.2.1. Methacrylate-Based Systems (PMMA, Bis-GMA, UDMA)

Dental resin composites (DRCs) are sophisticated materials designed for dental restoration, combining an organic resin matrix, inorganic fillers, and a coupling agent. This trio

ensures the filler bonds well to the resin, enhancing the composite's overall properties. DRCs also include initiators to start the polymerization process, inhibitors to prevent unwanted side reactions, and pigments to match the natural color of teeth. Their development marks a significant advancement in restorative dentistry, offering benefits such as an alternative to traditional amalgam fillings, easier clinical application, less tooth structure removal, improved fracture toughness over dental ceramics, and excellent color matching capabilities. As a result, DRCs have become a widely adopted solution for fillings and repairs, embodying a blend of functionality and aesthetic appeal [16].

In order to get the perfect viscosity for appropriate clinical use, dental resin composites (DRCs) combine base and diluent monomers using a dynamic organic monomer system. Inhibitors (also known as stabilizers) are used in this system to prevent the monomers from oxidising in the presence of air, while photo-initiators are used to initiate the free radical polymerization process. Pre- and post-polymerization, the mechanical and physical properties of the composites depend on the particular monomers utilized and their proportionate balance. Bisphenol A glycidyl methacrylate (Bis-GMA), urethane dimethacrylate (UDMA), and ethoxylated bisphenol A dimethacrylate (Bis-EMA) are important monomers in DRC formulations, as shown in Figure 4.

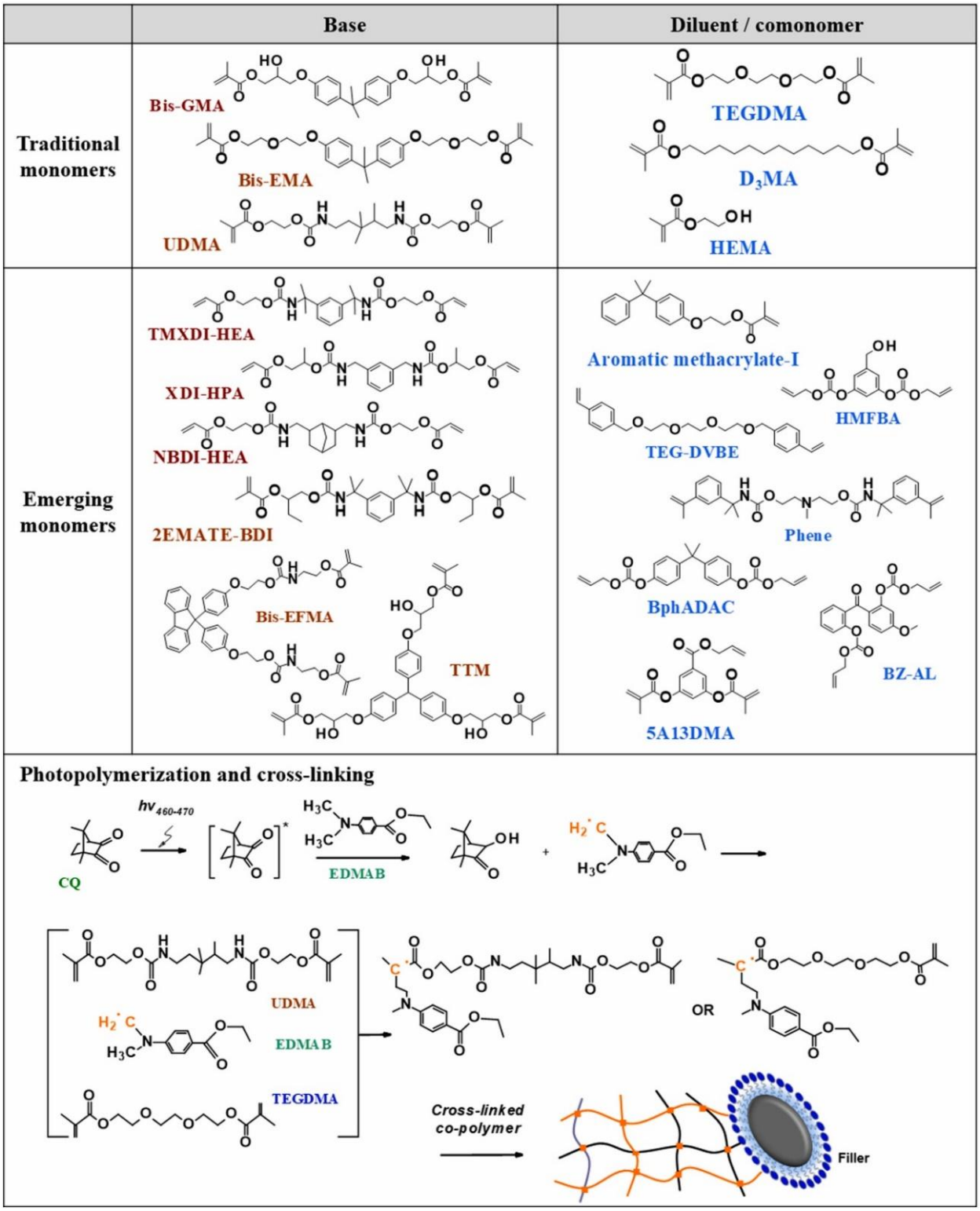

Figure 4. Dental monomer molecular structures and photopolymerization kinetics [23]

The mixture's viscosity is adjusted by adding cross-linking diluents including triethylene glycol dimethacrylate (TEGDMA), decanediol dimethacrylate (D3MA), and 2-hydroxyethyl methacrylate (HEMA). These methacrylate monomers are distinguished by their alkene groups due to the presence of carbon-carbon double bonds (C=C), which are critical for accelerating cross-linking and chain polymerization. These reactive methacrylate groups can be polymerized by a cross-linking reaction that can be catalyzed by light or chemical catalysts,

as well as an initial chain-reaction polymerization phase. This complex process defines the mechanical and physical properties of the composite, such as its elasticity, shrinkage, fracture strength, and dimensional stability, all of which affect how long the dental repair lasts and functions [24].

For decades, polymerized methacrylate has been widely employed in the production of denture bases [25]. PMMA (poly(methyl methacrylate)), is a polymer used in a variety of sectors, including paper, paint, automobiles, and dentistry (the production of dentures and orthodontic appliances) [26,27]. PMMA polymer is produced using free radical polymerization, with little batch variance when compared to other natural or raw polymers [28]. PMMA has been employed in a wide range of applications due to its low manufacturing costs and ease of maintenance [29]. PMMA polymer is made from methyl methacrylate monomer, a liquid. To improve its physical qualities and appearance, the polymer has been mixed with a variety of additives, including colors and synthetic fibers [30].

2.1.2.2. High-Performance Polymers in Dentistry - Polyetherimide (PEI)

Polyetherimide (PEI) is recognized as a high-performance material with broad applicability in contemporary engineering and industrial sectors. Its molecular framework is depicted in Figure 5.

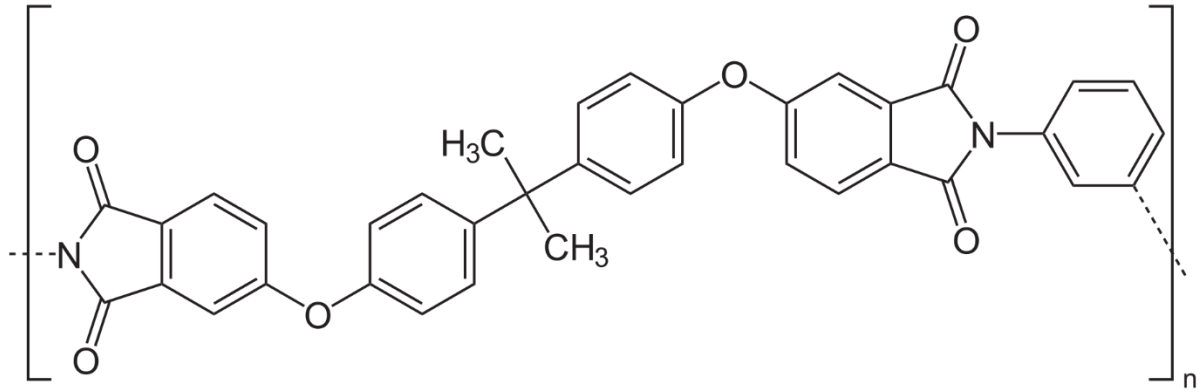

Figure 5. Simplified chemical structure of polyetherimide [31]

Polyetherimide (PEI) is a high-performance thermoplastic polymer distinguished by the incorporation of aromatic units, which strengthen its mechanical properties through imide groups (–CO–N–CO–) linked by ether bonds (–O–). The rigid aromatic segments embedded in the polymer backbone are largely responsible for its outstanding resistance to chemicals and its ability to withstand high temperatures. PEI is generally synthesized via a step-growth polymerization reaction between bisphenol-A dianhydride (BPADA) and diamine monomers, producing a highly stable and rigid polyamide structure. This molecular arrangement results in a notably high glass transition temperature, typically between 170 °C and 340 °C, while also ensuring excellent dimensional stability and electrical insulation. Owing to these properties, PEI is widely employed in advanced engineering applications that require superior thermal endurance, chemical resistance, and mechanical reliability [32].

PEI is acknowledged as a high-performance thermoplastic because of its balanced combination of mechanical durability, thermal resistance, and chemical stability. It possesses strong tensile and impact properties, which allow it to maintain structural integrity under demanding environmental conditions. Withstanding temperatures of approximately 170 °C,

PEI is well suited for applications in high-temperature settings. Its minimal moisture absorption and excellent electrical insulation further enhance its suitability for aerospace and electronic components, where dimensional precision and insulation are essential. Alongside its inherent flame-retardant nature and chemical resilience, these qualities emphasize PEI's importance in the production of advanced industrial and engineering materials [32]. In addition, its biocompatibility and ability to endure sterilization processes make PEI a valuable choice for medical devices, including surgical instruments, dental equipment, and housings for medical technologies [33].

These materials demonstrate remarkable mechanical strength, ensuring stability under demanding loads. Their thermal endurance allows them to retain properties even at high operating temperatures. With inherent flame-retardant behavior, they provide enhanced safety in applications exposed to fire risks. Their electrical characteristics remain consistent across a broad range of frequencies and temperatures, making them suitable for advanced electronic uses. Additionally, they exhibit robust resistance to chemicals and environmental stressors, which guarantees long-term reliability [34].

PEI can be manufactured using several thermoplastic processing methods, each tailored to specific requirements. Injection molding transforms the resin into a viscous melt that is injected into molds, allowing the creation of complex and detailed geometries. Extrusion shapes the molten polymer into continuous profiles such as sheets, rods, or tubes by pushing it through a precision die. Compression molding relies on heat and pressure to form the resin into solid parts within a mold cavity. A critical step before any processing is drying the resin thoroughly, since residual moisture can compromise mechanical integrity and reduce uniformity in the final product. By applying these techniques, industries can reliably produce PEI components with exceptional resistance to heat, mechanical stress, and environmental challenges, ensuring their suitability for demanding engineering applications [32].

In conservative dentistry, composite resins were introduced to overcome the limitations of acrylic resins, which themselves had replaced silicate cements in the 1940s. Today, these resin-based restorative materials are considered essential in biomaterials research due to their ability to replicate the mechanical and aesthetic qualities of natural dental tissues. Their advantages include a natural tooth-like appearance, straightforward handling during clinical procedures, and resistance to dissolution in oral fluids. Continued innovation in this area requires a detailed understanding of the individual components of composite resins and a systematic approach to modifying them for improved performance [35]. To enhance their clinical utility, researchers have incorporated silver particles to provide antimicrobial protection and titanium particles to improve biocompatibility [36]. The antimicrobial effect can be achieved either through direct microbial contact or via controlled release of active agents [35]. Composites containing 1% (w/w) quaternary ammonium polyethylenimine (PEI) nanoparticles have been tested, demonstrating antibacterial activity primarily through leaching mechanisms. Importantly, the inclusion of PEI nanoparticles did not compromise the mechanical integrity of the composites, and the antimicrobial effect persisted for at least one month [37].

A variety of materials have been employed in restorative dentistry [38], and selecting the most appropriate option for each clinical scenario is critical. This decision should consider not only aesthetic outcomes but also mechanical performance, durability, and the material's capacity to support functional rehabilitation [39]. To enhance the properties of restorative materials, innovations such as composite resins, fiber-reinforced resins, and polymer matrices reinforced with fibers have been introduced into the field of dental materials [40]. The mechanical behavior of these advanced materials often results from the synergistic interaction between the reinforcing fibers and the polymer matrix. Key factors influencing this performance include the volume fraction of incorporated fibers, the quality of the fiber–matrix

adhesion, and the diameter of the reinforcing fibersall of which significantly affect the overall properties of the final material [41].

Continuous carbon and glass fiber-reinforced polyetherimide (PEI) composites have been investigated as promising materials for the development of advanced bone prostheses. Additionally, PEI-based composites incorporating 4 wt. % of titanium dioxide nanoparticles have demonstrated antibacterial efficacy against both Gram-positive and Gram-negative bacterial strains. Over the past decade, PEI and PEI-based blend filaments, commercially known as ULTEM, have garnered increasing interest for additive manufacturing (AM) applications, signaling a significant shift toward their use in orthopedic innovations [42].

2.2. Ceramic Nanoparticles in dental composites

Particle-reinforced composites are made up of short particles that are classified based on their average size. This classification is divided into two categories: big particle composites and dispersion-strengthened composites. Large particle composites, which typically contain millimeter-sized or bigger particles, serve as the principal load bearers. They efficiently limit matrix deformation around common surfaces and act as the principal strengthening mechanism. In contrast, dispersion-strengthened composites use nanometer-sized particles. In these composites, unlike large-particle, the majority of the load under mechanical stress is supported by the matrix. Strengthening occurs at the atomic level, when scattered particles hinder the propagation of dislocation lines through the matrix.

A variety of inorganic fillers are used, including glass, quartz, and silica. Strontium, quartz, and barium glasses were once common fillers in composites [43]. However, glass particles have supplanted quartz because to their superior optical qualities, accessibility, and acceptable mechanical properties. However, the hardness of glass particles has been shown to induce substantial wear on antagonist teeth. Currently, composites commonly contain silicate particles generated from barium oxide, strontium oxide, zinc oxide, aluminum oxide, or zirconium oxide. These fillers typically make up 50-80% of the composite's weight, with particle sizes ranging from 5 nm to 85 μm [44]. Various filler-related parameters, including filler loading, size, shape, and particle distribution, have a substantial impact on composite physical and mechanical properties. Several investigations have found connections between filler parameters and mechanical qualities, higher radiopacity, improved aesthetics, and improved handling [14].

2.2.1. Conventional nanoparticles in dentistry

The evolution of materials science has led to the development of nanocomposites, defined as multiphase solid materials where at least one, two, or three dimensions of the reinforcing phase are less than 100 nm. The integration of nanoparticles as reinforcement in polymer-based composite materials is a fundamental strategy for achieving superior mechanical, thermal, and functional properties that cannot be attained with traditional micro-fillers. Unlike conventional composites, nanocomposites are distinguished by an exceptionally high surface-area-to-volume ratio and a vast interfacial area, which serve as the primary drivers of their superior performance [45,46].

The fundamental objective of engineering these materials is to synergize the intrinsic properties of diverse constituents, thereby creating unique nanomaterials with enhanced physical and chemical characteristics that surpass those of their individual components. Due to

this high surface-area-to-volume ratio, even low weight percentages of nanoparticles can significantly alter the overall performance of the composite [47]. This is primarily achieved by creating an extensive interphase region between the filler and the polymer matrix, which facilitates efficient load transfer and restricts polymer chain mobility. Consequently, these nano-scale interactions allow for the tailoring of specific material properties, such as increased stiffness, enhanced toughness, and improved thermal stability, essential for advanced industrial and biomedical applications [45,48].

The most common types of composites utilize microscopic or nanoscopic particles as reinforcements to enhance the base matrix (Figure 6). By integrating these fillers, manufacturers can significantly boost the material's overall strength and stiffness. As particle sizes are reduced to the nanoscale, the resulting composites exhibit superior properties that are not found in traditional materials. While nanoparticles are highly favored for large-scale industrial production due to their processing efficiency, they present a specific technical hurdle: their natural tendency to clump together. Because of intense attractive forces at the atomic level, achieving a perfectly uniform distribution (dispersion) within the matrix is critical to ensuring the high performance of the final product. Figure 8 shows a schematic illustration showing a composite structure reinforced with nanoparticles according to the literature [49].

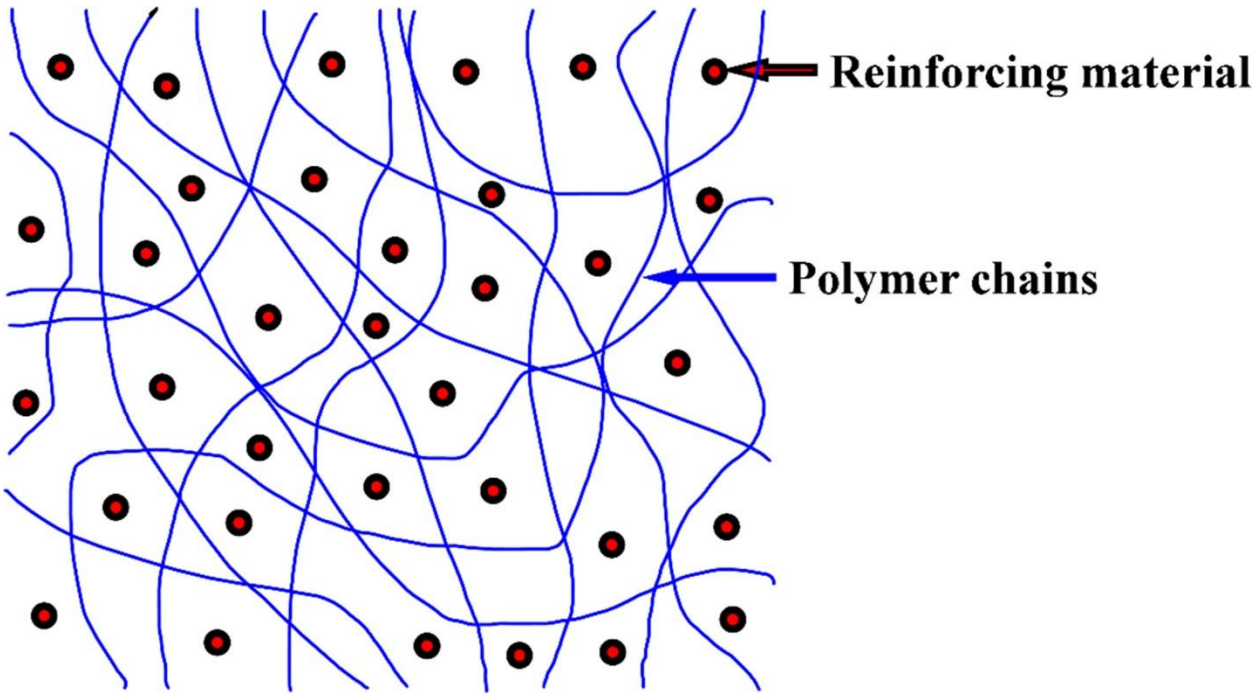

Figure 6. A schematic illustration depicting a nanoparticle-reinforced composite structure

Composite materials offer substantial functional advantages over traditional structural materials such as wood and metals, primarily due to their optimized strength-to-weight and stiffness-to-weight ratios. In high-performance applications, weight reduction is a critical factor; for instance, carbon-fiber-reinforced composites can exhibit five times the strength of 1020-grade steel while constituting only 5 wt. %. Similarly, these systems can achieve up to seven times the strength and double the modulus of 6061-grade aluminum, despite the inherent lightness of the metallic alloy. These properties are instrumental in the aerospace, automotive, and energy sectors, where reduced mass directly correlates with improved acceleration, fuel efficiency, and, in the case of wind turbines, increased electricity generation capacity [45,50].

While the primary focus of this dissertation involves the synthesis and characterization of zirconium dioxide (ZrO_2) nanofibers, a broader analysis of other ceramic oxide systems is necessary to understand the synergistic effects of multi-component reinforcement in complex physiological environments:

- ***Zirconium Dioxide (ZrO_2):*** Nano-zirconia is distinguished by its high fracture toughness, governed by the stress-induced transformation-toughening mechanism. This involves a martensitic-type transformation of metastable tetragonal grains into a monoclinic structure when subjected to localized stress at a crack tip. The resulting 3-5 vol. % expansion generates a compressive stress field that effectively shields the crack tip, preventing further propagation and increasing the overall energy absorption of the composite. The use of ZrO_2 in the form of nanofibers, as investigated in this work, further optimizes the aspect ratio, allowing for enhanced load transfer efficiency between the organic matrix and the inorganic phase [51,52]
- ***Silica (SiO_2):*** Silica is the most frequently utilized inorganic filler in dental composites due to its ability to improve surface smoothness and reduce polymerization shrinkage [53]. Recent studies have shown that nano-silica particles significantly enhance the optical translucency of resin-based materials [54].
- ***Aluminum Oxide (Al_2O_3)*:** Alumina is utilized for its extreme Vickers hardness and chemical durability. It functions as a primary load-bearing element in hybrid composites, protecting the softer polymer matrix from abrasive wear during repetitive masticatory cycles [55].
- ***Titanium Dioxide (TiO_2):*** Nano-TiO_2 is incorporated for its photocatalytic and antibacterial properties. Under ambient light, the surface of TiO_2 generates reactive oxygen species (ROS) that disrupt bacterial cell membranes, thereby inhibiting the formation of biofilms, such as Streptococcus mutans, and reducing the risk of peri-implantitis [56,57]

2.2.2. Bioactive ceramics

Bioactive ceramics represent a paradigm shift in restorative dentistry. Unlike traditional bioinert materials, which are designed to elicit minimal host response, bioactive ceramics are engineered to actively participate in tissue repair by triggering specific biological responses at the material-tissue interface. This interaction results in the formation of a robust chemical bond between the implant and the living host tissue [58].

Based on their chemical composition and interaction mechanisms, bioactive ceramics are primarily categorized into several key groups:

- *Bioactive Glasses (BG) and Glass-Ceramics*: These consist of a network of SiO_2, Na_2O, CaO, and P_2O_5. Their primary advantage is the high rate of surface reactions. Upon contact with physiological fluids, a rapid ion exchange occurs (primarily Na^+ and Ca^{2+} for H^+), leading to the formation of a silica-rich gel layer that serves as a template for calcium phosphate precipitation [59,60].
- *Calcium Phosphate (CaP) Ceramics***:** The most significant representatives are Hydroxyapatite (HA) and β-tricalcium phosphate (β-TCP). Given that the mineral phase of human bone and teeth is chemically similar to HA, these materials are inherently osteoconductive. While HA provides stable scaffolding, β-TCP is often preferred for regenerative applications due to it resorb ability, allowing it to be gradually replaced by natural bone [61,62].

- *Calcium Silicate (CS) Ceramics*: Materials such as tricalcium silicate (C_3S) form the basis of modern endodontic cements (e.g., MTA). These are critical for the regeneration of the pulp-dentin complex; during hydration, they release calcium hydroxide, creating a highly alkaline environment (pH ≈12.5) that exhibits strong antibacterial properties and stimulates the formation of a dent in bridge [63,64].

The hallmark of bioactivity is the process of biomineralization. Upon immersion in physiological environments, a layer of carbonated hydroxyapatite (CHA) forms on the ceramic surface [65]. This layer facilitates:

- *Bone induction*: The ability of the material to recruit undifferentiated mesenchymal stem cells and promote their differentiation into bone-forming osteoblasts [66].
- *Protein Adsorption*: The bioactive surface specifically binds proteins from blood and interstitial fluids, providing "anchoring points" for cell attachment and subsequent tissue growth [67].

Despite their biological superiority, pure bioactive ceramics suffer from inherent brittleness and low fracture toughness, making them unsuitable for high-load-bearing applications as monolithic structures. To address these limitations, contemporary research focuses on two strategies directly relevant to this dissertation:

- *Ionic Doping*: The incorporation of therapeutic ions such as strontium (Sr) to enhance bone formation, or zinc (Zn) and silver (Ag) to provide sustained antibacterial activity [66,68].
- *Hybrid Nanocomposites*: The integration of bioactive phases into polymer matrices (such as polyetherimide) reinforced with zirconia (ZrO_2) nanofibers. This dual approach combines the exceptional mechanical toughness of zirconia with the regenerative potential of calcium phosphates or silicates, resulting in a "smart" material capable of both structural integrity and biological integration [58].

2.2.3. Functional and advanced ceramic oxides

The transition from micro-scale to nano-scale reinforcements in polymer-based biomaterials addresses the critical limitations of traditional fillers, such as brittle fracture and interfacial debonding. Nanoparticles, characterized by an exceptionally high surface-area-to-volume ratio, facilitate extensive mechanical interlocking and molecular interactions with the polymer chains. In dental and prosthetic applications, ceramic oxides are prioritized due to their chemical inertness, high refractive index, and extreme hardness.While the primary focus of this dissertation involves the synthesis and characterization of zirconium dioxide (ZrO_2) nanofibers, a broader analysis of other ceramic oxide systems is necessary to understand the synergistic effects of multi-component reinforcement in complex physiological environments:

- ***Yttrium(III) Oxide (Y_2O_3):*** The significance of Y_2O_3 lies in its dual role as a phase stabilizer and a thermal-mechanical dopant. In zirconia-based systems, yttria occupies vacant sites in the crystal lattice, stabilizing the tetragonal phase and preventing spontaneous transformation in the absence of external stress. Furthermore, Y_2O_3 improves the hydrothermal stability of the composite by mitigating the diffusion of water molecules into the ceramic structure, which is the primary cause of low-temperature degradation (LTD) in moist oral and physiological environments [69,70].

2.2.3.1 Perovskite-type oxides ABO_3

- ***Barium Zirconate ($BaZrO_3$):*** his perovskite-structured ceramic is integrated into resin matrices primarily to achieve the required levels of radiopacity. In clinical diagnostics,

radiopacity is essential for the non-destructive assessment of restoration integrity and the detection of secondary caries. $BaZrO_3$ nanoparticles are particularly advantageous because their refractive index ($n \approx 1.50$ - 1.55) is closely matched to those of typical dental monomers, such as Bis-GMA and TEGDMA. This compatibility ensures that high filler loading can be achieved without compromising the optical translucency or the polymerization depth of the material, which are critical for aesthetic outcomes [71,72].

- ***Barium Titanate ($BaTiO_3$):*** In recent years, barium titanate ($BaTiO_3$) has emerged as a significant advancement among dental ceramics. This material possesses piezoelectric properties comparable to those of natural bone, which is a critical factor for successful osseointegration. Due to its affordability, chemical stability, and non-toxicity, $BaTiO_3$ has seen extensive use across the biomedical field. Its adoption in dentistry is further driven by the limitations of traditional metal alloys, which often exhibit poor esthetics and undesirable chemical interactions within the oral cavity. Compared to conventional biomaterials, BaTiO3-based ceramics offer superior corrosion resistance, improved color matching for enhanced esthetics, greater mechanical strength, and excellent radiopacity [73,74].
- ***Strontium Titanate ($SrTiO_3$):*** Beyond its function as a rigid reinforcement that increases the elastic modulus, $SrTiO_3$ provides a specific bioactive response through an ion-release mechanism. The presence of Sr^{2+} ions in the ceramic lattice allows for controlled leaching into the surrounding biological fluid, which has been shown to stimulate osteoblast differentiation and accelerate the mineralization of the extracellular matrix. Structurally, these nanoparticles serve as pinning sites that obstruct the mobility of polymer chains, thereby enhancing the resistance of the composite to plastic deformation and surface indentation [75].

2.2.4. Processing of oxide powders

- ***Thermal treatments****:* Hydrothermal synthesis represents a highly significant and promising technique for the development of nanocomposite materials. This method is particularly valued because it is conducted at moderate temperatures, which facilitates the enhancement of crystallinity, crystal size, and shape. Furthermore, the surface chemistry of the resulting materials can be precisely tuned by adjusting several parameters, including sol composition, reaction temperature and pressure, solvent type, the nature of additives, and aging time. This approach is also characterized by its use of environmentally benign procedures and relatively simple equipment [76]. The hydrothermal method operates through a heterogeneous reaction within an aqueous medium to generate nanostructured materials [77]. These reactions are typically performed in closed systems to maintain the necessary pressure and temperature. Recently, the microwave-assisted hydrothermal approach has gained substantial interest in the field of nanomaterial engineering, as it successfully combines the rapid heating advantages of microwave techniques with the structural control of hydrothermal synthesis. Ultimately, the hydrothermal technique provides an intriguing and practical methodology for the production of diverse nanomaterials [78].
- ***Sol-gel****:* The sol–gel technique is a bottom-up synthesis method that produces advanced materials through a series of irreversible chemical reactions [79,80]. This approach is highly favored for preparing nanocomposites due to its numerous advantages, including low external energy consumption, the use of cost-effective precursors—such as metal

alkoxides or nitrates—and the ability to achieve high purity and consistency in the final products at reduced calcination times and temperatures [76]. A primary benefit of the sol–gel process is the creation of stable surfaces with a high surface area, where the final physical and chemical properties are directly influenced by the specific experimental settings applied during synthesis [81]. The procedure begins by dispersing precursors into a solvent and stirring the mixture at low temperatures to produce a suspension known as a "sol." Through subsequent hydrolysis and condensation reactions, colloidal particles gradually form a network of metal hydroxide or oxide bridges, resulting in a "gel." Finally, after a crystallization and annealing stage, the desired nanocomposites are obtained [76]. Ultimately, sol–gel chemistry serves as a versatile platform for material science, enabling the engineering of a wide variety of nano- and microstructures with diverse chemical compositions and unique morphologies that are unattainable through other methods [80].

- ***Mechanochemical activation****:* High-temperature mechanochemical technology (HTMT) has emerged as an efficient "short-process" synthesis route for producing high-reactivity nano-ZrO_2 powders, significantly enhancing the densification and mechanical properties of ceramic composites such as boron carbide (B_4C). Unlike traditional multi-stage methods, mechanochemical activation utilizes the synergy of high-energy ball milling and thermal energy to induce atomic rearrangement and structural defects, which effectively lowers the phase transition temperature and produces ultra-fine nanoparticles with a narrow size distribution [82]. When integrated into a ceramic matrix, these activated powders promote in situ chemical reactions during sintering, forming secondary phases like ZrB_2 and W_2B_5, which inhibit grain growth and facilitate near-theoretical densification [83,84]. Consequently, the resulting microstructure exhibits superior mechanical integrity, characterized by a substantial increase in both Vickers hardness and fracture toughness [82].

2.3. Nanofibers as advanced reinforcements

Fiber-reinforced composites (FRCs) are widely established, produced, and utilized across various industries. These materials consist of a metal, polymer, or ceramic matrix that encapsulates fibrous reinforcements characterized by superior mechanical properties, including high tensile strength and a high modulus of elasticity. The overall stiffness and strength of the resulting composite are governed not only by the intrinsic properties of the constituent materials but also by a critical dimensionless parameter: the aspect ratio (the length-to-diameter ratio) of the fibrous phase [85].

Fibers are defined as elongated reinforcements with a transverse cross-sectional diameter or thickness not exceeding 250 μm. Generally, these materials maintain an aspect ratio (the ratio of length to diameter/thickness) of 100 or greater [43]. However, this ratio may fall below 100 in specific instances, such as with whiskers, staple fibers, or chopped and short fibers. The mechanical performance of fiber-reinforced resin composites is determined by the specific type, length, and orientation of the fibers, as well as their volume fraction. In dental applications, glass fibers are predominantly used due to their cost-effectiveness and chemical similarity to silica. Furthermore, they exhibit superior mechanical properties and enhanced interfacial bonding with the polymer matrix compared to alternative reinforcements like polyaramid, carbon/epoxy, or ultra-high molecular weight polyethylene [86].

Based on the aspect ratio and spatial arrangement, fiber-reinforced composites are categorized into three primary groups: continuous (long) and aligned, discontinuous (short) and aligned, and discontinuous with random orientation (Figure 7).

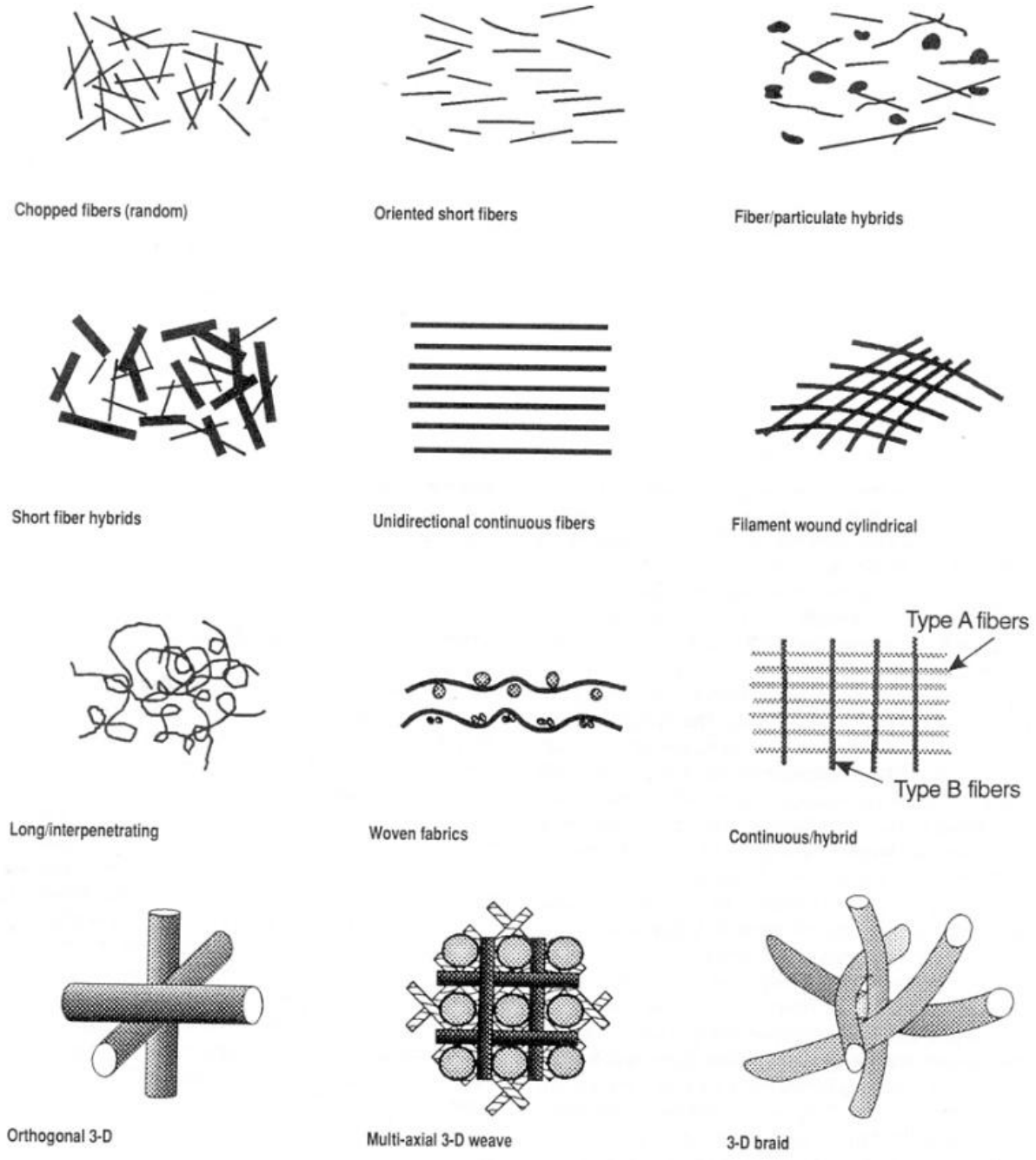

Figure 7. Examples of reinforcement types, combinations, fiber orientations, and arrangements in composites [87]

Studies have demonstrated that, in comparison to more widely used materials, short glass fiber resin composite structures, which are utilized for temporary dental crowns and bridges, display greater flexural strength and compressive load-bearing capacity [40]. In dental resin-based composites, the combination of bio ceramic (nHA) and high-strength (E-glass fiber) materials has demonstrated good results in terms of degree of conversion (DC); however, higher loading of nHA/E-glass fiber can impact water sorption behavior and impair resin-filler adhesion. Although different reinforcing element concentrations exhibit inconsistent impacts

on hardness and flexural strength, all experimental composites satisfy ISO 4049's standards for flexural strength in resin-based materials [88].

Nano-sized electrospun fibers have been found to improve composite properties like flexural strength and modulus when incorporated in low weight fractions (1–5%) with spheroidal silica fillers. In contrast, micron-sized fibers can degrade material properties at higher concentrations by aggregating and causing voids in the matrix. As co-fillers, nanofibers can improve wear resistance and decrease polymerization shrinkage by encircling other particle fillers in a protective layer. Nanofibers improve strength and modulus during fiber pull-out by bridging cracks and absorbing energy. The predominant types of glass fibers employed in dental practice are E-glass and S-glass. S-glass has a lower lifespan than E-glass but a higher tensile strength and elastic modulus [89].

2.3.1. Zirconia-based nanofibers

Zirconium, a resilient transition metal, boasts an array of applications when harnessed in its oxide state, commonly referred to as zirconia or zirconium oxide. Recognized as ceramic steel, zirconia stands out for its innate toughness, abrasion resistance, high melting point, and low frictional coefficient. At the nanoscale, its value skyrockets due to exceptional thermal stability, luminescence, refractive index, chemical resilience, expansive surface area, biocompatibility, and pronounced antibacterial, antioxidant, and antifungal attributes. These remarkable traits have spurred intensive exploration within the scientific community, leading to the integration of zirconia-based nanomaterials across diverse technological domains. From functional materials like catalysts and sensors to structural components such as coatings for cutting tools, ceramics, and implants, zirconia finds extensive utility. Furthermore, its utility extends to applications as a dielectric, electro-optic, and piezoelectric substance, owing to its favorable optical and electrical characteristics [90].

The physicochemical properties of ZrO_2 are inextricably connected to its crystal structure, which is highly impacted by the manufacturing method used. At ambient pressure, ZrO_2 exists in three polymorphic forms: monoclinic below 1150 °C, tetragonal between 1150 °C and 2300 °C, and cubic above 2300 °C; additionally, an orthorhombic phase appears under high-pressure conditions [91]. Recent advances in nanotechnology have enabled the successful fabrication of one-dimensional zirconium oxide nanostructures using a variety of techniques, including the hydrothermal method [92], sol-gel [93], ablation [94], chemical vapor deposition (CVD) [95], template synthesis [96], direct electrochemical anodization [97], and electrospinning [98]. According to previous research, electrospinning is a simple, scalable, and reproducible method for creating one-dimensional nanostructures [99].

Zirconium dioxide (ZrO_2) fiber materials, encompassing both fiber films and fiber aerogels, have attracted considerable attention due to their favorable attributes, including low density, low thermal conductivity, and consistent physical and chemical properties [100]. These qualities have positioned them as highly desirable in various applications such as high-temperature air filtration, thermal insulation, sound absorption, noise reduction, catalyst carriers, battery separators, and ceramic matrix composite materials [101]. However, the brittleness inherent in ZrO_2 fiber materials has constrained their practical usability. Consequently, researchers have been actively engaged in the pursuit of flexible and compressible ZrO_2 fiber materials, emerging as a prominent focus of investigation [102]. Numerous endeavors have been initiated to achieve this objective, aiming to expand the range of applications for these materials.

Currently, the primary technologies for producing ZrO_2 fibers are electrospinning [103,104], centrifugal spinning [105], and solution blow spinning [106]. Electrospinning is the most widely used process for synthesizing ZrO_2 fibers. Nonetheless, because to the limitations of electrospinning, it often produces ZrO_2 fiber films [107]. Although it is possible to transform ZrO_2 fibers produced by electrospinning into ZrO_2 fiber aerogels using suspension preparation and freeze-drying methods, this method is complex and inefficient [108,109]. Centrifugal spinning is also a common process for producing ZrO_2 fibers, however it frequently produces fibers with greater diameters and less flexibility [110]. Unlike electrospinning and centrifugal spinning, solution blow spinning addresses their limitations by enabling the production of fibers with comparable diameters while also allowing for the direct fabrication of three-dimensional fiber aerogel structures [101].

Ceramic fiber aerogels have recently gained popularity due to their outstanding features, which include low thermal conductivity, great chemical stability, and low density. These aerogel materials typically consist of one-dimensional components such as nanowires or nanofibers, and include both oxide fiber aerogels (e.g., SiO_2, ZrO_2) and non-oxide fiber aerogels (e.g., Si_3N_4 and SiC). Compared to SiO_2, ZrO_2 has a higher thermal tolerance, making it ideal for application in harsher environments [111]. Non-oxide ceramic fibers are often created by processes such as chemical vapor deposition, which are less efficient and require more rigorous conditions [112]. Furthermore, non-oxide ceramic fibers frequently require oxygen-free environments for use because their temperature resistance under oxidative conditions is poor. ZrO_2 fiber aerogels, on the other hand, can be manufactured using technologies such as solution blow spinning, which are more efficient and offer superior temperature resistance under oxidative circumstances, making them promising for use in a variety of applications.

Ceramic fibers are typically produced by using polymers to create spinning solutions that aid in fiber development. Polyvinyl alcohol (PVA) [113,114], polyethylene oxide (PEO) [115,116], and polyvinylpyrrolidone (PVP) [117,118] are some of the most often used polymer templates. These polymers are derived from nonrenewable petrochemical sources. These polymers must be deleted during the ceramic fiber preparation process, thus getting them from low-cost and ecologically benign products is desirable. Cellulose, a naturally occurring and renewable polymer substance, is a possible alternative. Carboxymethyl cellulose (CMC) and hydroxypropyl methylcellulose (HPMC) are examples of water-soluble cellulose derivatives that can be generated by altering cellulose [119,120]. Substituting these cellulose derivatives for the currently employed polymers as templates in ceramic fiber manufacture would greatly reduce reliance on nonrenewable resources while also accelerating ceramic fiber development.

The electrospinning technique was first documented to be used by C. Shao et al. [121]. The PVA/$ZrOCl_2$ solution was used to create nanofibers with diameters varying from 50 to 200 nm. Tetragonal ZrO_2 nanofibers were obtained by calcining the nanofibers at 800°C. ZrO_2 nanofibers stabilized with Y_2O_3 were synthesized and studied by A. M. Azad et al. [122]. PVP, zirconyl chloride, and yttrium nitrate nanofibers were calcined at 1500 °C for one hour, producing YSZ nanofibers with a cubic form as a consequence of Y_2O_3 stabilization. ZrO_2 nanofibers were synthesized from a solution of PVP and zirconium acetylacetonate by E. Formo et al. [123]. Furthermore, ZrO_2 and ZrO_2/TiO_2 nanofiber production using single and double jet electrospinning was shown by M. Su et al. [124]. PVP/$ZrOCl_2$ and PVP/$ZrOCl_2$/$Ti(C_4H_9O)_4$ as-spun nanofibers were calcined in air at 600 °C for 3 h, yielding m-ZrO_2 and t-ZrO_2/a-TiO_2 nanofibers, respectively. The ZrO_2/TiO_2 nanofibers in particular showed excellent detection qualities, including good repeatability, high sensitivity, and quick reaction and recovery times.

Usama et al. [125] explored the fabrication of three types of nanofibers — inorganic zirconia (ZrO_2), organic polymeric (Bis-GMA, TEGDMA, PEGDMA), and hybrid nanofibers

(ZrO_2 + Bis-GMA + TEGDMA) — to investigate how these affect the mechanical behavior of PMMA resin.

- Zirconia Nanofibers [125]:

The production process began by dissolving polyvinyl alcohol (PVA) in water to prepare a 12% solution. The solution was heated at 85 °C for complete dissolution and then stirred for a day. To make the spinning solution, zirconium oxychloride and water were mixed with the PVA in a specific ratio (20:1:2). Electrospinning was done with precise conditions, including a flow rate of 0.1 ml/h and a set distance of 10 cm between the spinneret and collector. The fibers were dried at 70 °C and calcined gradually to 1000 °C to form stable ZrO_2 nanofibers.

- Organic Nanofibers (Bis-GMA/TEGDMA/PEGDMA):

These fibers were fabricated by dissolving equal parts of the three monomers, stirring at 40 °C, and spinning them at 24 kV with a flow rate of 0.4 ml/h. The resulting fibers were dried in vacuum at room temperature for two days.

- Hybrid Nanofibers (ZrO_2 + Bis-GMA/TEGDMA):

Equal amounts of Bis-GMA and TEGDMA were blended, combined with varying percentages of ZrO_2 (1–20 wt.%), and processed similarly. The spinning used a higher voltage (28 kV) and a lower flow rate (0.2 ml/h). Fibers were again air-dried under vacuum. Çetinkaya et al. [126] produced ZrO_2–SnO_2 composite nanofibers using electrospinning. Separate solutions of zirconium nitrate and tin chloride were prepared, mixed in various volume ratios, spun at 18 kV with a feed rate of 0.8 ml/h, and heat-treated at 550 °C. SEM analysis showed bead-free, smooth fibers that retained continuity after annealing, with diameters decreasing slightly due to calcination. Sun et al. [127] developed zirconia nanofibers by dissolving zirconium carbonate and using PVP as a spinning aid. Electrospun fibers were sintered at 1200 °C. Li et al. [128] created ZrO_2/ZnO nanofibers to study their combined effects on gas sensing. They used zinc acetate and $ZrOCl_2$, spun fibers under optimal conditions, and calcined them at 500 °C. Yasin et al. [129], Yu et al. [130], Song et al. [131], and Barakat et al. [132] studied $Zr_xTi_{1-x}O_2$ nanofibers with various zirconium-to-titanium ratios, noting how these ratios influence the crystalline phases formed after annealing. Lower Zr/Ti ratios tended to produce anatase TiO_2, while higher ratios led to mixed or tetragonal ZrO_2 phases. Rodaev et al. [133] electrospun ZrAA/PAN composite fibers, then thermally treated them to form bead-free zirconia fibers. Careful heating preserved the fibrous structure while removing organics. Finally, other researchers used PVP and zirconium alkoxides to make high-quality zirconia nanofibers with mean diameters around 98 nm. The fibers maintained their morphology after calcination at 850 °C [134]. A completely homogenized combination of dental composite components with uniform filler dispersion in the matrix and flawless air bubble removal can be achieved using a variety of techniques [135]. In order to do this, centrifugal planetary mixers [136], mechanical mixers [137], sonication [138], solution-evaporation mixing method [139], mixing at a somewhat increased temperature [139], and a hand spatula were used to homogenize the filler and matrix phase. Three roller mixers [140] were utilized to further disperse the filler phase in the matrix. In order to eliminate air bubbles, these mixing procedures are typically done under vacuum and/or after vacuuming the paste mixture. The features of dental composites are greatly influenced by the filler's quality of dispersion in the matrix, which is examined under a microscope. Furthermore, voids, also known as trapped air bubbles, in the

matrix are mostly created during the manufacturing and clinical manipulation processes, and they have the potential to adversely impact the mechanical properties of dental composites.

Electrospinning has emerged as a versatile and robust technique for the fabrication of continuous one-dimensional (1D) nanostructures, particularly nanofibers, with diameters ranging from a few nanometers to several micrometers. This technique is uniquely positioned in the field of dental materials science due to its ability to produce high-aspect-ratio reinforcements that mimic the hierarchical structure of natural tissues. Unlike conventional mechanical fiber-drawing methods, electrospinning utilizes electrostatic forces to stretch a polymer or composite solution into ultra-fine filaments.The fundamental appeal of electrospinning in the context of zirconia (ZrO_2) synthesis lies in its adaptability to the sol-gel process. By incorporating ceramic precursors into a carrier polymer solution, this method allows for the production of green fibers which, upon subsequent thermal treatment, yield pure ceramic nanofibers. These nanofibers possess a high surface-area-to-volume ratio and superior mechanical properties, making them ideal candidates for reinforcing dental matrices such as polyetherimide.The process is governed by a complex interplay of several parameters, which can be broadly categorized into solution properties (viscosity, conductivity, and surface tension), processing conditions (applied voltage, flow rate, and tip-to-collector distance), and ambient parameters. Understanding and fine-tuning these variables is critical for controlling the fiber morphology, preventing beads formation, and achieving the desired mechanical integrity of the composite implants.

In next chapter, the principles of electrospinning are detailed, focusing on the optimization of parameters necessary to achieve defect-free zirconia nanofibers suitable for high-performance biomedical applications.

2.4. Electrospinning technique

In recent years, electrospinning has gained popularity as a versatile technology for a range of biomedical and dental applications, including dental caries prevention, wound healing, and tooth regeneration. Unique features of electrospun materials include a high surface-to-volume ratio, enhanced cellular contacts, and protein absorption that makes it easier for cellular receptors to bind. The potential of electrospun nanofibers for the regeneration and repair of several dental and oral tissues, such as the dentin, dental pulp, periodontal tissues, oral mucosa, and skeletal tissues, has been thoroughly studied. However, there are a number of electrospinning-related drawbacks that prevent these materials from being used in practical or medical settings. To overcome the constraints with regard to the biomaterial elements, a deeper comprehension of the characteristics, regulated manufacture, and operation of electrospun materials is required. It is clear that additional in vivo research is required to assess the biocompatibility of electrospun scaffolds. In order to survive mechanical stresses encountered in tissue regeneration applications, these scaffolds' mechanical qualities also need to be strengthened. Furthermore, a number of electrospun materials' features were examined in light of their possible dental uses [141].

Numerous disciplines have found electrospinning to be remarkably popular, which has led to a dramatic increase in scholarly papers in recent years.

2.4.1. Fundamental Electrospinning Principle and Method

The electrospinning approach includes creating a significant potential difference between a polymer solution flowing through a capillary tip and a metallic collector [142]. A standard electrospinning system includes a high-voltage power source, a syringe fitted with a flat-tip needle, and a conductive collector (see Figure 8a) [143]. However, this basic configuration can be modified for specialized purposes — for example, using a dual-needle setup to produce mixed fibers or a rotating mandrel collector to generate hollow, tube-like structures. Traditionally, electrospun materials feature an unwoven arrangement of nanofibers. Electrospinning with two electrode strips (Figure 8b) can be employed to gather aligned fibers [144].

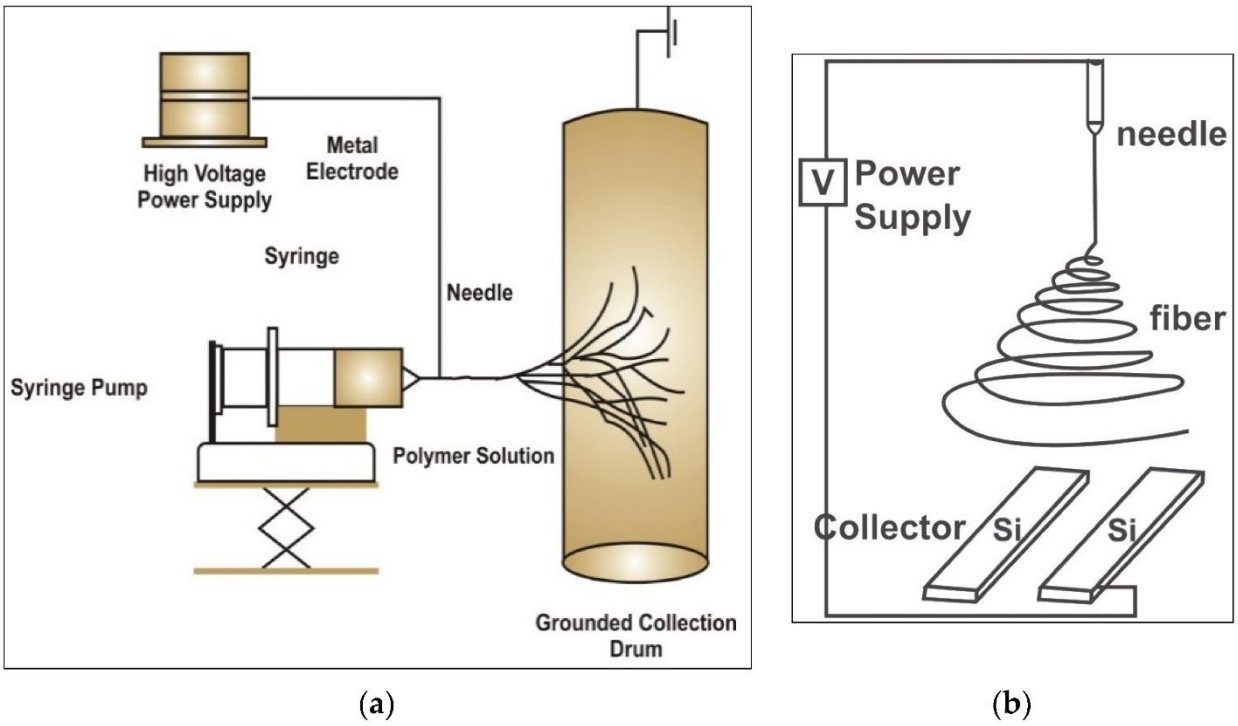

Figure 8. Schematic representation of the electrospinning process (a) a standard electrospinning apparatus and its components (b) collector modifications for aligning electrospun nanofibers [141]

Electrostatic forces exceed the surface tension of the polymer solution due to the potential voltage difference, causing a jet of charged fluid to break into nanofibers that fall towards the collection plate and solidify [145]. During electrospinning, the polymer jet splits into multiple streams that form numerous nanofibers, which settle on the collector. As this happens, the solvent evaporates, resulting in dry nanofibers being deposited on the collector surface [146].

2.4.2. Elements Influencing Electrospinning

Continuous nanofibers can be created by electrospinning from a variety of materials. However, the morphology and properties of electrospun fibers are affected by numerous factors, including physical, system-related, processing, and solution parameters.. Table 1 shows the important variables influencing electro-spun fibers [147].

Table 1. List of variable parameters influencing the qualities of electrospun fibers [147]

Process Parameters	Systemic Parameters	Solution Parameters	Physical Parameters
Voltage	Polymer type	Viscosity	Humidity
Flow rate	Molecular weight	Concentration	Temperature
Collection plate	Polymer	Conductivity	Air velocity
Distance	Architecture	Dielectric constant	-
Angle	Solvent used	Surface tension	-
Motion	-	Charge of jet	

2.4.2.1 Solution Related Parameters

To keep the jet from breaking up into droplets before the solvent fully evaporates, the solution must have optimal properties, specifically, low surface tension along with adequate charge density and viscosity [148]. The molecular weight, concentration, surface tension, solution viscosity, and solution conductivity of polymers affect the form and features of nanofibers. Higher molecular weight solutions are more viscous than lower molecular weight solutions because molecular weight is a measure of the polymer chain length, which in turn affects the entanglements. During the process, these entanglements keep the jet from breaking too soon. A low viscosity polymer solution jet can form beaded fibers or fragment into tiny droplets [149]. Viscous solutions produce uniform fibers free of beads and increase chain entanglements. The fluid may dry up or drop at the tip if the viscosity is too high, making it harder to pump through the capillary [15].

The solution's surface area is reduced by surface tension, which also compels it to form spherical droplets. High ratios of solvent molecules have a stronger propensity to combine and take the form of beads or spheres at low concentrations [149]. It is best to employ low surface tension solvents to achieve homogeneous fibers free of beads. When solutions with higher conductivity, those that include ions, have a lot of electrostatic charge in the jet. For instance, increasing the jet stretching and helping to generate smooth fibers rather than beaded fibers can be achieved by adding a small amount of polyelectrolyte or salt to the electrospinning fluid.

2.4.2.2. Polymer Concentration

When the concentration of the fluid falls below the threshold value, droplets rather than fibers will develop. Viscose solutions are produced by high solution concentrations, which might cause processing issues. Higher viscosity, for instance, produces a bigger fiber diameter by resisting jet elongation and thinning. The association between bead formation and the viscosity of polyethylene oxide (PEO) solutions was investigated in a prior work. Their findings suggested a relationship between solution viscosity and bead density and size. Less spherical and more spindle-like beads were produced by viscous solution, which was followed by the production of nanofibers and sporadic flaws in the beads [149].

2.4.2.3. Processing Conditions

The electrospinning process can be impacted by processing parameters like voltage, collector type, distance, flow rate, and needle gauge. For the jet to form and exit the needle, a high voltage is needed to generate sufficient charges within the solution. With a comparatively smaller Taylor cone, higher voltage accelerates a larger volume of electrospinning fluid [142]. The feed rate controls the amount of solution that is accessible between the needle and the electrospinning target. Because of the increased feed rate brought on by the voltage rise, the solution stretches more and gains diameter. Increased feed rates can also result in inappropriate solvent evaporation before the fiber is collected, which can fuse the fibers together. The jet's flight time is shortened due to the decreased distance. As a result, the jet could not have enough time to harden, which would cause the fibers to fuse. The orifice's diameter has an impact as well. Because the jet is exposed to the environment for a shorter period of time, clogging is reduced by smaller internal diameter. A smaller droplet results from an increase in the solution's surface tension caused by a reduction in the needle's internal diameter. As a result, the jet's acceleration drops. Jet hence experiences greater stretching and elongation and more flight time prior to deposition; this leads to fibers with a reduced diameter [141].

The primary variables influencing the fiber morphology and web characteristics during electrospinning are the aforementioned parameters. The collector's design is an additional consideration. Conventional electrospinning typically yields nanofibers with a random orientation. By altering the collectors' design, it is possible to control the fiber's deposition geometry and obtain different desired fiber patterns.

2.4.2.4. Voltage's Effect

Higher amounts of drawing stress would result from the polymer jet being discharged with stronger repulsion when the applied voltage was increased. The outcome is a drop in fiber diameter, which raises the probability of a progressively higher fiber diameter distribution and complicates process control. To start the polymer jet from the Taylor cone apex, the ideal voltage is needed. Before the jet formed, the droplet shape was significantly influenced by the applied voltage. Faster electrospinning and a higher solution flowrate are the outcomes of higher voltage [142].

2.4.2.5. Rate of Volumetric Flow

The flow rate must be adjusted within the proper range in order to stabilize the Taylor cone. Vacuum typically forms as a result of the needle's slow flow rate, which makes the Taylor cone vanish and momentarily halts the electrospinning process. Solution may accumulate at the needle tip with a faster flow. The duration that ions remain in contact with the needle affects how quickly charges are transferred into the solution, as higher flow rates reduce the surface charge density. The diameter, porosity, and shape of nanofibers are influenced by the solution flow rate [142]. To minimize bead formation in electrospun fibers, it is essential to maintain a stable and uniform flow rate [150]. The diameter of electrospun nanofibers was decreased by a slow flow rate. Furthermore, compared to a quicker flow rate, a slow flow rate produced fewer beads and smaller diameters [151].

2.4.2.6. The collector's distance

The collector's distance has a negative power connection because it reduces the width of the polymer jet and elongates bending instabilities and whipping action. Surface charge density decreases exponentially. The surface charge density decreases as the gap distance increases. The electric field between the charged solution and collector weakens with increasing distance between them, resulting in the formation of fewer charged ions [43,86]. The needle tip's diameter is an additional process parameter, since it has been observed that a larger needle tip diameter increases fiber diameter [152]. On the other hand, it has been noted that there is no relationship between the diameter of the needle and the fiber that results [153].

2.4.2.7. Conductivity's Effect

Compared to poor conductivity, high conductivity allows polymer solutions to transport more charge. Therefore, increased conductivity results in decreased nanofiber diameter and increased tensile stresses in proportion to applied voltage [154]. In their investigation into the impact of adding sodium chloride to a polymer for the creation of electrospun nanofibers, Fong et al. [149] found that the electrospinning jet's net charge density was greater. Uniform and smooth nanofibers are formed as a result of the higher charge density. Zong et al. [154] investigated the impact of incorporating salts into solutions of poly-DL-lactic acid (PDLLA) and electrospun smooth, bead-free, and fine-diameter nanofibers. As an alternative, surfactants can be used to increase the conductivity of a polymer solution [155]. Similar outcomes were obtained when surfactants were included in the modifications to create homogenous nanofibers with smaller diameters [156].

2.4.2.8. The effects of the solvent

Prior to electrospinning, the solvent's solubility and boiling point should be considered. The quick evaporation and dehydration of the nanofibers makes volatile solvents the best choice [157]. Avoiding a very low boiling temperature that promotes fast evaporation is advised to avoid obstructing or blocking the needle aperture before electrospinning. In contrast, solvents with high boiling points may fail to evaporate entirely before the fibers land on the collector, leading to the formation of flat, ribbon-shaped fibers instead of cylindrical ones. It is important to exercise extra caution when evaluating and choosing electrospinning solvents since the solvent's volatility can have an impact on the microscopic characteristics of the fibers, such as their porosity, shape, and size [156].

2.4.3. Electrospun fibers in biomedical application

The primary applications of electrospun materials remain focused on tissue engineering and the functional regeneration of dental and oral structures. The electrospinning technique has proven exceptionally effective for fabricating biomimetic scaffolds that facilitate cellular growth and structural repair [158,159]. By mimicking the architecture of the natural extracellular matrix (ECM), these scaffolds provide essential topographical cues for the regeneration of periodontal tissues and alveolar bone. For instance, fibers based on poly(L-lactic acid) (PLLA) or polycaprolactone (PCL) reinforced with hydroxyapatite have demonstrated significant success in promoting the osteogenic differentiation of dental pulp stem cells [160]. A wide range of materials has been successfully processed via electrospinning for dental applications, including natural polymers such as silk, collagen, and chitosan, as well as synthetic polymers like polyvinyl alcohol (PVA) and polydioxanone. To further enhance bioactivity, nanocomposites incorporating hydroxyapatite blends or bioactive glass are

frequently integrated into the fiber matrix to promote mineralization and osteoconduction [161]. Beyond their role as structural scaffolds, electrospun nanofibers have found extensive usage in broader biomaterials and biomedical frameworks, specifically:

- Localized Drug Delivery: Nanofibers serve as high-capacity reservoirs for the controlled release of therapeutic agents. This approach allows for the sustained delivery of antibiotics, such as metronidazole or tetracycline, directly into periodontal pockets. This localized treatment significantly reduces the need for high systemic doses and minimizes potential side effects [162,163].
- Implant Surface Modification: Coating metallic or ceramic implants with electrospun layers provides a bioactive interface that enhances osseointegration. Recent research indicates that coating implants with zirconia-based nanofibers improves surface wettability and promotes faster bone-to-implant contact, which is critical for long-term clinical success [163].
- Advanced Restorative Nanocomposites: As an alternative to conventional spherical fillers, integrated nanofibers are utilized to overcome the inherent brittleness of dental resins. These fibers provide reinforcement through mechanisms such as crack bridging and crack deflection, which are essential for increasing the fracture toughness and longevity of posterior restorations [164,165].

Figure 9 graphically depicts the standard protocol for dental tissue regeneration utilizing electrospun scaffolds. There has been discussion on the advancements and possibilities of electrospun nanoparticles for dental applications.

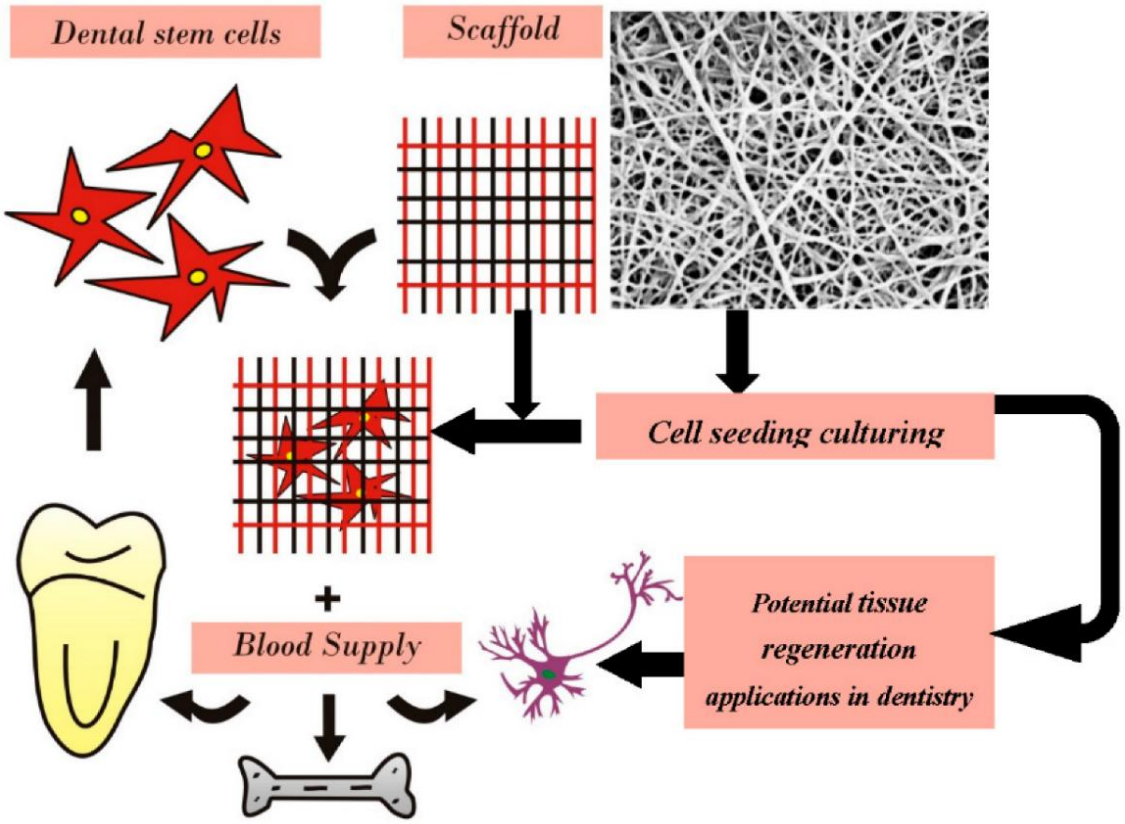

Figure 9. Diagram illustrating the use of electrospinning scaffolds in dental and oral tissue engineering [141]

Current advancements in the field are shifting toward "smart" electrospun systems and nanofibers capable of responding to physiological stimuli, such as pH fluctuations or the presence of specific bacteria, offering a promising future for personalized and regenerative dental care. The exceptional performance of electrospun nanofibers in biomedical applications is primarily attributed to their unique structural characteristics, including high interconnecting porosity, precisely controllable pore size, and an expansive specific surface area. These physical attributes enable electrospun membranes to outperform traditional materials in critical areas such as advanced wound dressings, scaffolds for complex tissue engineering, and systems for targeted drug release. By synthesizing current research breakthroughs with an analysis of existing challenges—such as scaling up production and ensuring long-term stability—it is evident that electrospinning technology is poised to become a transformative force in the future of biomedical materials and regenerative dentistry [162].

2.4.3.1. Zirconia nanofibers in dentistry

The evolution of zirconia-based materials in dentistry has transitioned from monolithic restorative structures to sophisticated one-dimensional (1D) nano reinforcements. Zirconia (ZrO_2), nanofibers, primarily synthesized via electrospinning, represent a strategic advancement in overcoming the inherent brittleness of dental resin matrices while maintaining the aesthetic and biocompatible standards required for clinical success [166].

In conventional dental composites, zero-dimensional (1D) nanoparticles are utilized to enhance wear resistance and minimize polymerization shrinkage. However, 1D zirconia nanofibers offer unique mechanical advantages that nanoparticles cannot provide:

- *Enhanced Load Transfer***:** Due to their high aspect ratio (length-to-diameter ratio), nanofibers facilitate more efficient stress distribution from the polymer matrix (e.g., polyetherimide) to the high-strength ceramic phase.
- *Crack Bridging and Toughening***:** Nanofibers act as physical barriers to crack propagation. When a micro-crack initiates, the nanofibers span the crack void, providing closure stresses that significantly increase the fracture toughness of the composite [166,167].

The mechanical integrity of zirconia nanofibers is fundamentally dependent on the stabilization of the tetragonal phase (t-ZrO_2). In the presence of a propagating crack, the metastable t-ZrO_2 grains undergo a stress-induced martensitic transformation into the monoclinic phase (m-ZrO_2). This phase change results in a localized volume expansion (3–5%), which generates a compressive field around the crack tip, effectively arresting its growth [58,168]. Recent studies emphasize that maintaining a fine grain size within the nanofibers is crucial; if the grains grow beyond a critical threshold during calcination, the material becomes highly susceptible to low-temperature degradation (LTD), leading to premature mechanical failure in the aqueous environment of the oral cavity [58,169].

The fabrication of these nanofibers relies on the synergy between sol-gel chemistry and electrospinning. By tailoring the viscosity and conductivity of the spinning dope (zirconium precursors mixed with a carrier polymer like PVP), researchers can produce continuous, defect-free "green" fibers. Optimization of Parameters: The final morphology and crystalline structure are dictated by processing conditions such as applied voltage, flow rate, and the subsequent calcination profile. Biomimetic Potential: Beyond mechanical reinforcement, the nanofibrous architecture mimics the natural extracellular matrix (ECM). This high surface area allows for functionalization with bioactive ions (e.g., Ca^{2+}, Mg^{2+}) to promote faster osseointegration in dental implant applications [168,170]. The primary hurdle in the clinical translation of zirconia

nanofiber-reinforced composites is achieving homogeneous dispersion. Preventing the agglomeration of nanofibers is essential, as clusters act as stress concentrators rather than reinforcements. Current research, including the scope of this dissertation, focuses on surface modification techniques and optimized mixing protocols to ensure a robust interphase between the zirconia nanofibers and the dental resin matrix.

2.5. Characterization of dental materials

Numerous characterization test techniques have been used to define the physical, mechanical, chemical, antibacterial, cytotoxic, and self-healing properties of dental composites in study. The characteristics of dental composites have significantly evolved as a result of advancements in characterization test procedures. The qualities of the dental composite work together and depend on one another to provide the intended result. Therefore, using the appropriate characterization test procedures greatly increases the accuracy of the findings. Based on a search, it appears that while a number of review papers have been published about dental composites [16,171], only two review papers—published by Ferracane et al. [172] and Ilie et al. [173] are related to dental composite characterization techniques. The first publication focused on studying several approaches for managing property characterization, polymerization kinetics, and polymerization shrinkage stress and strain. The second study reviewed various methods used to assess the mechanical properties of dental composites. These two publications have provided helpful approaches for characterization, along with many instructions and recommendations for device configurations and method procedures. Apart from the techniques employed for the characterization of innovative dental composites with biocompatibility, they haven't covered the characterization methods for the assessment of physical attributes and biocompatibility.

2.5.1. Mechanical characterization

Material strength is not an inherent trait but depends on the specimen's shape, preparation, and the test used, influenced by how force applies stress. While testing under common use conditions, like those in the oral cavity, seems logical, it's crucial to remember that most forces create complex stresses within a material. This complexity is particularly true in the oral environment, where forces are rarely straightforward due to teeth's anatomy and jaw mechanics. The strength also hinges on the material's composition and preparation quality, suggesting that tests under the most challenging conditions offer a more accurate assessment of performance. Tensile tests are preferred for their thoroughness, but flexure tests are often used as a practical alternative since they simulate a mix of stresses. Proper specimen preparation is vital to avoid misleading results due to flaws. The ISO standard 4049 for dental composites recommends flexure testing, which has shown a moderate correlation with clinical wear but not with major fractures, according to research. Additionally, artificial aging of specimens may improve the correlation with actual clinical outcomes [173]. Figure 10 shows the characterization process used to assess the mechanical properties of dental composite.

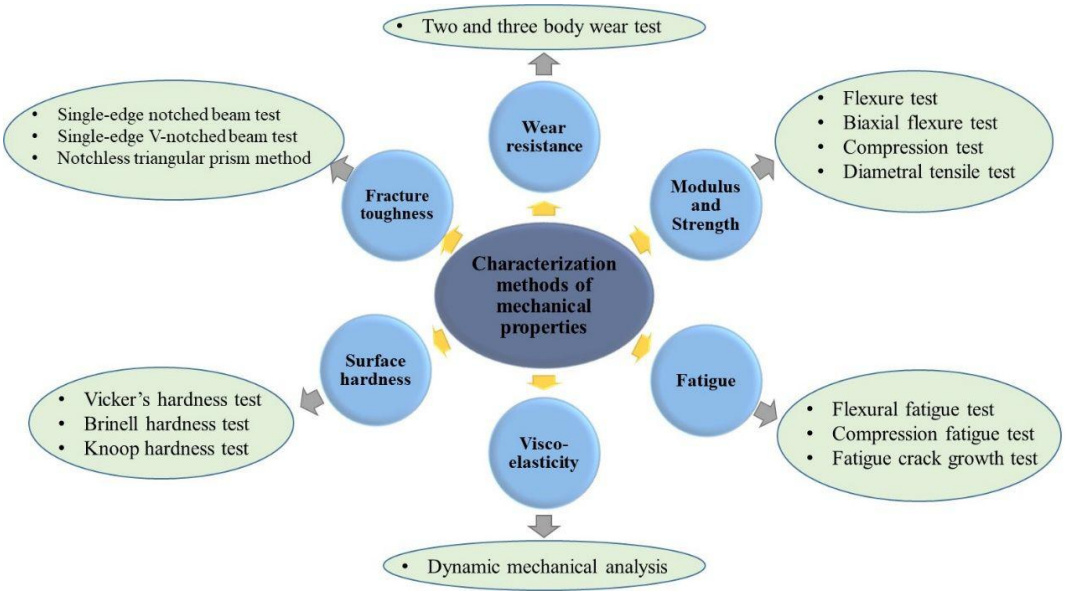

Figure 10. The group of characterization techniques used to assess dental composites' mechanical qualities [174]

2.5.1.1. Flexural properties

This method, widely used for testing dental composite strength, involves choices in support and load application, specimen geometry, and preparation. Typically, it employs 3-point bending (Figure 11), where the specimen acts as a beam supported by two rollers set apart at a specific distance, with a central top load applied. The ISO 4049 standard governs dental composites, while ASTM D790-10 applies to other plastics. The beam, prepared to fit the test supports and allow for beam mechanics principles, is tested on a low-compliance, rigid frame to ensure load transfer directly to the specimen. Deviating from these specifications can compromise test validity. Tests run to failure expect minimal specimen plastic deformation; significant bending may lead to calculating yield strength instead of failure load if the beam excessively bends. Ideally, a strain gauge measures true beam deformation, though often omitted for simplicity. If the specimen and frame are rigid, deformation can be reasonably estimated from the cross-head motion, allowing for elastic modulus and strength measurement within acceptable error margins [173].

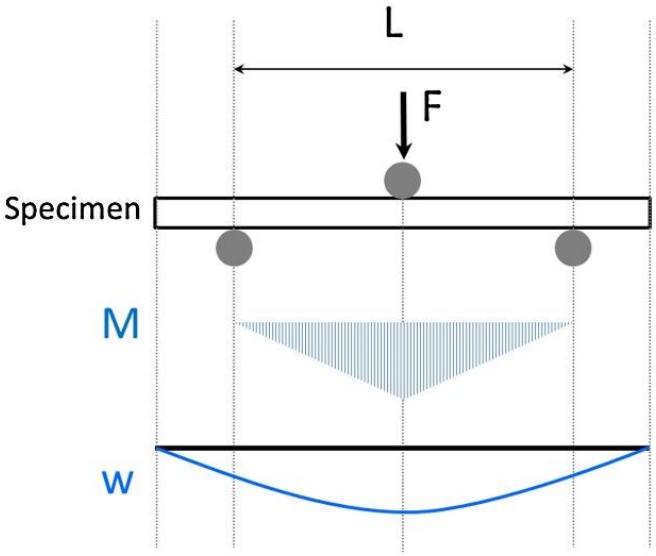

Figure 11. Diagram of the three-point bending test illustrating deflection (w) and bending moment (M) [173]

Flexure strength testing can be conducted using a four-point bending approach (Figure 12), where the load is applied at two separate points, distributing stress over a larger beam area. This method ensures failure occurs within a specific region, essential for accurate beam equation application. Unlike three-point bending, where failure might not directly align with the load point, potentially skewing results, four-point bending provides a more controlled failure zone. Studies suggest that three-point bending may yield higher strength results compared to four-point, although both tests can be executed similarly on specimens of identical dimensions [173].

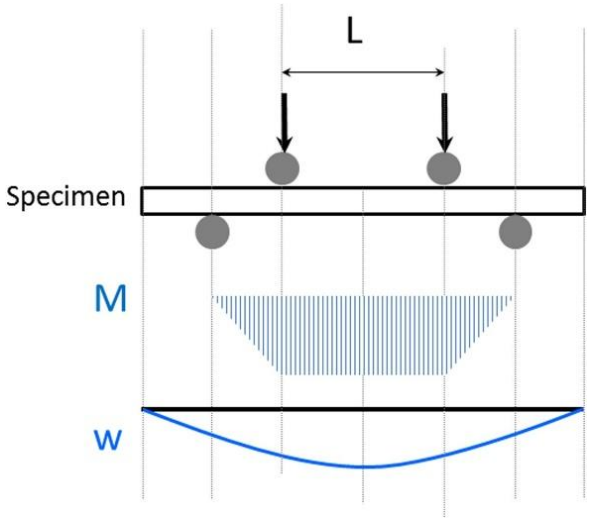

Figure 12. Ilustration of the four-point bending test displaying the deflection (w) and bending moment (M) [173]

2.5.1.2 Micro- and nanoindentation

Indentation or scratch tests have been a staple for assessing material hardness for over a century, particularly useful for characterizing resin composites. These tests involve pressing a hard indenter against the sample, leaving an indentation that reflects the material's resistance to deformation. Hardness is calculated by dividing the maximum load by the indenter's contact

area. Traditional methods like Brinell, Knoop, Rockwell, and Vickers focus primarily on the plastic deformation aspect (Figure 15). Although initially developed for metals, these methods are also applicable to brittle materials, as the stress distribution caused by indentation mimics hydrostatic pressure combined with shear stress, often preventing brittle fracture. Given that resin composites exhibit both plastic and elastic deformation, a more nuanced approach using depth-sensing hardness measurements is advisable. This dynamic technique measures the applied load along with the indenter's penetration depth, enabling differentiation and analysis of the material's plastic and elastic deformation components [173].

A Vickers indenter is used to indent the photo-polymerized specimens, and VH is computed using equation (1), which is the ratio of the maximum load (P_{max}) to the maximum projected contact area (A_{max}) [174].

$$HV = \frac{P_{max}}{A_{max}} = 1.8544 \times \frac{P_{max}}{\mathrm{d}^2} \quad (1)$$

where the two indented diagonals' mean length is represented by d. The hardness of dental composites is also measured using the Brinell and Knoop hardness procedures [175]. Figure 15shows the indenter shape associated with the hardness testing.

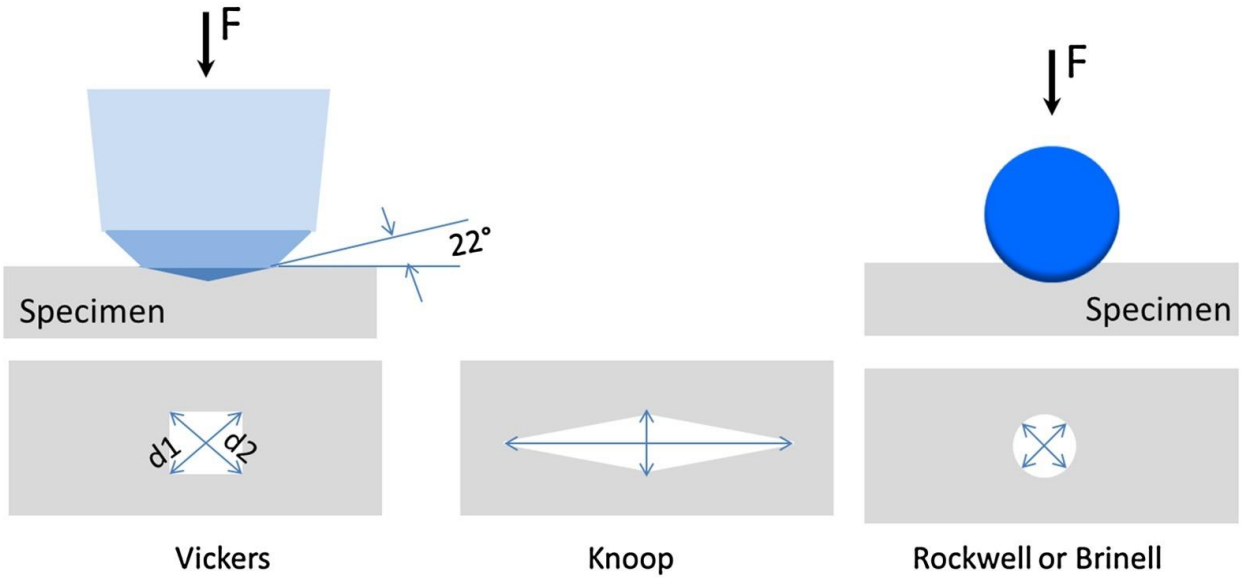

Figure 13. Indentation shapes and their corresponding imprints from Vickers, Knoop, Rockwell, and Brinell hardness tests [173]

Hardness measurement is categorized into macro-, micro-, or nano-scale based on the applied forces and resulting displacements according to ISO 14577-1:2015. In the macro range, forces range from 2 N to 30 kN. In the micro range, forces are greater than 2 N and indentation depths exceed 0.2 µm. Finally, in the nano range, indentation depths are less than or equal to 0.2 µm. It is important to note that the micro range has an upper limit set by the test force (2 N) and a lower limit determined by the indentation depth of 0.2 µm [173].

At the nanoscale, mechanical deformation is strongly influenced by the precise shape of the indenter tip, and the computed material properties are greatly affected by the contact area function specific to the indenter used. Thus, precise calibration of both the instrument and

indenter shape is crucial for achieving reproducible material parameters across different machines. Additionally, the specimen's surface must be smooth to ensure a regular indentation shape and clear visualization, and it should be positioned perfectly perpendicular to the indenter [173].

2.5.1.3 Fracture behavior

The fracture behaviour of the investigated dental nanocomposites was analysed to evaluate the influence of electro spun zirconia nanofibers on the failure mechanisms of the resin matrix. In conventional dental composites, brittle fracture is the dominant failure mode, characterized by rapid crack propagation through the polymer matrix with minimal energy absorption [176]. However, the integration of zirconia nanofibers significantly alters this behaviour by introducing several energy-dissipating toughening mechanisms [177].

Fracture resistance in the developed nanocomposites is significantly enhanced through a bridging mechanism. As micro-fractures develop under load, the integrated zirconia nanofibers remain intact across the crack faces, effectively 'sewing' the matrix together. This process absorbs a substantial amount of energy, as additional force is required to overcome the interfacial bonding between the fibers and the surrounding resin [178]. These "bridges" exert closure forces that counteract the opening displacement, effectively reducing the stress intensity at the crack tip. This process requires additional energy to either deboned the fibers from the matrix or to fracture the fibers themselves, which significantly increases the material's fracture toughness (K_{IC}) [179].

Furthermore, crack deflection was identified as a critical secondary toughening mechanism. When a propagating crack encounters a zirconia nanofiber, it is forced to deviate from its original path, moving along the fiber-matrix interface [178]. This increases the total fracture surface area and further dissipates the energy associated with crack growth. Another observed phenomenon is fiber pull-out, where the energy is consumed as fibers are frictionally withdrawn from the matrix during the final stages of fracture, preventing sudden catastrophic failure [180].

The analysis of the fracture surfaces via SEM reveals a transition from a smooth, mirror-like surface—typical of brittle failure—to a much rougher, hierarchical topography in the fiber-reinforced specimens. This increased roughness is a direct indicator of higher energy dissipation during failure. The integration of electrospun nanofibers, characterized by their high aspect ratio, mitigates the risk of stress localization often associated with spherical particles [181]. By distributing mechanical strain more effectively throughout the composite matrix, these fibers provide superior resistance to the cyclic forces of mastication, ensuring a more robust clinical performance [182].

2.5.1.4 Wear

The degradation of dental materials in the oral environment is a complex phenomenon, primarily governed by the synergy between mechanical loading and chemical degradation. While fundamental tribology classifies material loss into adhesive, abrasive, fatigue, and corrosive processes, dental wear is often more accurately described through its clinical manifestations to better reflect the intraoral reality [183].

In the clinical context, wear is typically categorized into three distinct types, each involving specific physical interactions [183]:

Attrition: This represents wear occurring at direct tooth-to-tooth or tooth-to-restoration contact sites. From a mechanical standpoint, attrition is driven by adhesive wear and surface fatigue. Under high masticatory forces, especially in parafunctional habits like bruxism, these contact areas experience significant stress concentrations, leading to micro-cracking and progressive loss of material.

Abrasion: This refers to material loss at non-contact sites, caused by the intervention of a third body. It can be further divided into:

Two-body abrasion: Such as the interaction between a toothbrush/dentifrice and the material surface.

Three-body abrasion: Occurring during mastication when food particles act as an abrasive medium between the restoration and the antagonist. In resin-based composites, this often results in the preferential wear of the softer polymer matrix, leading to the exposure and eventual exfoliation of filler particles—a process known as the "plucking effect."

Corrosion and Erosive Wear: Unlike mechanical wear, erosion involves the chemical dissolution of the material by exogenous or endogenous acids. In the oral cavity, this often manifests as tribocorrosion, where chemical softening of the composite matrix significantly lowers its resistance to subsequent mechanical abrasion.

To bridge the gap between laboratory findings and clinical outcomes, various in-vitro methodologies have been standardized. The ISO/TS 14569-2 technical specification outlines protocols for using dynamic chewing simulators that attempt to replicate the complex kinematics of human mastication.These simulations typically employ two main testing geometries:Two-body wear tests: Used to simulate attrition by providing direct sliding or impacting contact between the sample and an antagonist (e.g., steatite or ceramic balls).Three-body wear tests: These involve an intermediary abrasive slurry (e.g., polymethyl methacrylate (PMMA) beads or organic seeds in a liquid medium) to mimic the abrasive nature of a food bolus.The resistance of dental composites is quantitatively assessed by measuring the volume loss (mm^3) or the maximum wear depth (μm) using profilometry or 3D digital scanning. Furthermore, the evolution of surface roughness (R_a) is a critical parameter, as increased roughness not only compromises the aesthetic quality of the restoration but also promotes the adhesion of dental plaque and subsequent secondary caries [184].

2.5.2 Thermal characterization

Thermal characterization plays a fundamental role in evaluating the performance and reliability of dental restorative materials. Since the oral environment is subject to frequent and rapid temperature fluctuations—ranging from 5 °C to over 55 °C during the consumption of cold and hot beverages—understanding the thermal response of dental nanocomposites is essential for predicting their clinical longevity. These thermal changes can induce internal stresses due to the mismatch in thermal expansion coefficients between the polymer matrix, the inorganic fillers, and the surrounding natural tooth structure [185,186]. The application of standardized thermal analysis techniques provides a comprehensive profile of the material's structural integrity and thermodynamic properties, serving as a bridge between laboratory synthesis and clinical application [187].

2.5.2.1 Thermogravimetric Analysis (TGA)

Thermogravimetric analysis (TGA) is employed to monitor the mass change of dental composites as a function of temperature or time under a controlled atmosphere. This technique is instrumental in assessing the thermal stability and decomposition kinetics of the polymer matrix. In dental research, TGA is primarily used to determine the precise filler weight fraction, as the organic resin components undergo oxidative degradation while the inorganic reinforcement remains stable at elevated temperatures, typically up to 800 °C. Furthermore, TGA can identify the presence of residual solvents or unreacted monomers and provide insight into the efficiency of the silanization process at the filler-matrix interface [188,189].

2.5.2.2 Differential Scanning Calorimetry (DSC)

Differential Scanning Calorimetry (DSC) measures the heat flow associated with physical and chemical transitions within the material. For dental resin composites, DSC is crucial for identifying the glass transition temperature (T_g), which marks the shift from a rigid vitreous state to a more flexible rubbery state. This parameter is a vital indicator of the material's cross-linking density and overall polymerization efficiency. Additionally, DSC can be used to quantify the exothermic heat of polymerization, allowing for the evaluation of the reactivity of various monomer systems and the potential thermal impact on the surrounding dental tissues during the curing process [189].

2.5.2.3 Dynamic Mechanical Analysis (DMA)

Dynamic mechanical analysis (DMA) uses a dynamic method to evaluate material properties by applying cyclic stress and observing the material’s response. It applies a variable sinusoidal stress, while simultaneously measuring the resultant sinusoidal strain. Resin composites display viscoelasticity, meaning they show both elastic and viscous responses. In purely elastic materials, the stress and strain waves are in phase (0° phase difference), whereas in purely viscous materials, the phase difference is 90°. For viscoelastic resin composites, the phase difference, along with the amplitudes of the stress and strain waves, is used to determine key material parameters. These include the storage modulus, loss modulus, complex modulus, and tan delta (also known as the loss factor) [190].

2.5.3 Structural and morphological characterization

The performance of dental nanocomposites is fundamentally dictated by the structural arrangement of the filler phase and the quality of its integration into the organic matrix. To evaluate these characteristics, a combination of spectroscopic and microscopic techniques is employed, providing insight into the chemical bonding, crystalline structure, and spatial distribution of the reinforcements.

2.5.1.1 Fourier-Transform Infrared Spectroscopy (FTIR)

FTIR spectroscopy is utilized to identify the functional groups present in the dental composites and to verify the success of surface modifications, such as the silanization of

nanoparticles. By analysing the characteristic vibrational modes (e.g., Si-O-Si stretching or C=O bonds in methacrylate resins), FTIR can also be used to determine the Degree of Conversion (DC). This is achieved by comparing the ratio of aliphatic C=C double bonds before and after light-curing, which is a critical indicator of the material's final mechanical properties and biocompatibility [191,192].

2.5.1.2 X-ray Diffraction (XRD)

X-ray diffraction is essential for determining the crystalline nature of the synthesized nanoparticles (e.g., the perovskite structure of $SrTiO_3$ or the phases of MnO_2). In the context of the final composite, XRD analysis can confirm whether the filler maintains its structural integrity during the polymerization process. Furthermore, the broadening of diffraction peaks allows for the estimation of the average crystallite size using the Scherrer equation, providing a quantitative basis for the "nano" scale of the reinforcing phase [193].

2.5.1.3 Scanning Electron Microscopy (SEM) and EDS

Scanning Electron Microscopy (SEM) is the primary tool for investigating the morphological features of the dental materials [194]. It is employed to [195]:

- Examine the filler-matrix interface, where a seamless transition indicates strong chemical and mechanical interlocking.
- Assess the dispersion and distribution of nanoparticles to ensure the absence of large agglomerates, which could act as stress concentrators.
- Analyse the fracture surfaces after mechanical testing to determine the failure mode (e.g., ductile vs. brittle) and observe phenomena such as "plucking" or crack deflection.

When coupled with Energy-Dispersive X-ray Spectroscopy (EDS), this method provides elemental mapping, confirming the uniform presence of specific elements (e.g., Sr, Ti, Mn, Si) across the composite surface [196,197].

2.5.4. Biocompatibility

Biocompatibility is a fundamental requirement for any dental restorative material, representing its ability to coexist with the host's biological systems without eliciting harmful local or systemic responses. According to the ISO 10993-1 standard and current regulatory guidelines, the assessment of dental nanocomposites must consider the triadic interaction between the material's chemical composition, the dynamic oral environment, and the physiological response of the host tissues [198,199]. For resin-based materials, this evaluation is particularly critical due to the potential leaching of unreacted monomers or the release of reinforcing nanoparticles, which can induce oxidative stress or inflammatory pathways.

2.5.4.1 The MTT Cytotoxicity Assay

The standard for the initial biological screening of dental materials is the MTT assay, a quantitative, colorimetric method used to evaluate cellular metabolic activity and viability. This assay is based on the enzymatic reduction of the yellow tetrazolium salt, 3-(4,5-dimethylthiazol-2-yl)-2,5-diphenyltetrazolium bromide (MTT), by mitochondrial succinate dehydrogenase enzymes in living cells.

The biochemical process results in the formation of insoluble, purple formazan crystals within the mitochondria. After solubilizing these crystals, the optical density (OD) is measured using a spectrophotometer at a specific wavelength (typically 570 nm). The core principles and advantages of applying the MTT assay in this research include:

- *Metabolic Mapping*: The intensity of the purple coloration is directly proportional to the number of viable, metabolically active cells, allowing for a precise calculation of the survival rate relative to a control group.
- *Dose-Response Evaluation*: It enables the determination of the cytotoxic threshold of the nanocomposite extracts, providing data on whether the addition of STO/MnO_2 nanoparticles influences the overall biological safety of the resin matrix.
- *Correlation with Polymerization*: The assay is instrumental in observing how the Degree of Conversion affects biocompatibility; typically, higher conversion rates lead to reduced cytotoxicity as fewer residual monomers remain available for leaching into the surrounding tissues [200,201].

2.6. Current progress and challenges

Nanocomposites represent a transformative class of materials prized for their structural and functional synergy. In the field of dentistry, the transition to the nanoscale offers unprecedented opportunities to improve mechanical strength and aesthetics, though it significantly complicates the processing and characterization of the materials. The success of high-quality dental nanocomposites relies fundamentally on selecting an appropriate fabrication route to ensure the uniform dispersion of nanofillers within the matrix—the most crucial and challenging aspect of production [76,80,202].

The sol–gel technique remains a cornerstone "bottom-up" approach for preparing these materials, favored for its low energy consumption and the ability to yield high-purity products with unique morphologies [76,80]. By manipulating parameters such as solvent polarity and catalyst concentration, researchers can achieve precise control over particle size and phase stability, which is vital for managing the tetragonal-to-monoclinic transformation in zirconia [81]. Complementing this, hydrothermal synthesis offers a route to enhanced crystallinity and controlled shapes at moderate temperatures. Recent advancements in microwave-assisted hydrothermal methods have further accelerated reaction kinetics while maintaining an ecologically benign profile [76,78,203].

To achieve superior mechanical reinforcement, electrospinning has emerged as a premier technique for the fabrication of various nanostructures. This process allows for the transformation of sol-gel precursors into continuous nanofibers through the application of high voltage, resulting in reinforcements with an exceptionally high aspect ratio. Unlike traditional spherical nanoparticles, zirconia nanofibers produced via electrospinning provide a superior ability to bridge micro-cracks and prevent their propagation within a polymer matrix through the "crack-bridging" mechanism. This morphology facilitates a more efficient interfacial stress transfer, where the high surface area of the fibers ensures a strong mechanical and chemical bond with the host polymer [82,204]. Experimental findings within this research have shown

that even at low filler loadings, such as 1 wt. %, these nanofibers can significantly enhance the surface microhardness of the polymer matrix, providing a more resilient surface against the abrasive forces encountered in the oral cavity [205]. he reinforcement effect is predominantly governed by the effective transfer of mechanical load from the ductile PEI matrix to the high-modulus ZrO_2 nanofibers. Upon mechanical stress, these 1D nanostructures bridge the advancing crack fronts, effectively dissipating energy through fiber debonding and pull-out mechanisms, which prevents catastrophic failure of the composite. Additionally, techniques such as high-temperature mechanochemical technology (HTMT) can be utilized to further tailor the interphase and lower phase transition temperatures, facilitating near-theoretical densification and superior fracture toughness [82].

Despite these advancements, a significant research gap persists regarding the optimal integration of these 1D nanostructures into high-performance biocompatible matrices, such as polyetherimide (PEI). While spherical nano powders have been extensively studied, their ability to provide multi-directional reinforcement is often limited by their tendency to agglomerate, which creates stress concentrators rather than reinforcements. Polyetherimide, as a high-performance thermoplastic (HPP), offers exceptional thermal stability and chemical resistance, yet its potential as a matrix for electrospun zirconia nanofibers remains under-explored [206]. Building upon previous investigations involving various ceramic reinforcements, such as $BaZrO_3$ and hybrid $SrTiO_3/MnO_2$ systems in acrylic matrices, this work specifically targets the limitations of traditional fillers by utilizing the structural advantages of zirconia nanofibers within a high-performance polyetherimide host. Initial results indicate that the integration of calcined monoclinic ZrO_2 nanofibers into PEI not only improves mechanical integrity but also maintains the thermal stability of the composite, as evidenced by a consistent degradation onset in thermogravimetric analysis [71]. Furthermore, there is a lack of long-term data regarding the interfacial stability and aging behaviour of these novel nanofibers under the complex thermo-mechanical and biochemical conditions of the oral cavity, where phenomena such as tribocorrosion and hydrolytic degradation must be considered [198,207].

This research addresses these challenges by focusing on the synthesis and characterization of composite implants reinforced with zirconia nanofibers. By combining sol-gel processing with electrospinning, this work seeks to precisely engineer the morphology and interphase of the reinforcement to enhance the mechanical properties of the PEI matrix. The ultimate goal is to bridge the gap between laboratory-scale discovery and the development of next-generation dental implants, ensuring that technical excellence in mechanical properties—such as increased microhardness and fracture toughness, is balanced with long-term biocompatibility and clinical safety as dictated by the latest ISO 10993-1:2020 standards [208].

3. EXPERIMENTAL PART

3.1 Materials

Polyetherimide (PEI), polyacrylonitrile(PAN), N,N-dimethylformamide (DMF), zirconyl chloride octahydrate ($ZrOCl_2 \cdot 8H_2O$), barium zirconate ($BaZrO_3$), strontium titanate ($SrTiO_3$) and yttrium oxide (Y_2O_3) were purchased from Sigma-Aldrich, Germany.

3.2. Preparation of samples

3.2.1 Synthesis of reinforcing phases

3.2.1.1 Fabrication of electrospun ZrO_2 nanofibers

Zirconia nanofibers were synthesized using a combined sol-gel and electrospinning approach. Initially, a 10 wt. % precursor solution was prepared by dissolving 1 g of polyacrylonitrile (PAN, M_w = 150.000 g mol^{-1}) in 9 g of N,N-dimethylformamide (DMF) under magnetic stirring at 50 °C for 2 h. To this solution, 0.3 g of zirconyl chloride octahydrate ($ZrOCl_2 \cdot 8H_2O$) was added and homogenized in an ultrasonic bath (42 kHz) for 5 min. The resulting solution was electrospun using a Linari Engineering system at a constant feeding rate of 1.5 mL/h. A voltage of 22 kV was applied, with a tip-to-collector distance of 15 cm. The collected green mats were vacuum dried at 30 °C for 24 h to eliminate residual solvent. To obtain the final crystalline phase, the mats were calcined in an electric furnace at 1100 °C for 1 h (heating rate of 5 °C/min), resulting in the formation of high-purity monoclinic ZrO_2 nanofibers [205].

3.2.1.2. Preparation of $BaZrO_3/Y_2O_3/SrTiO_3$ hybrid nanoparticles

Hybrid oxide nanoparticles were prepared via a high-energy ball milling process. The precursor powders, comprising $BaZrO_3$, $SrTiO_3$, and Y_2O_3 in a specific weight ratio of 87:10:3, were milled at 300 rpm for 30 min. This ratio was optimized through iterative testing to achieve the most favourable particle morphology and structural stability. The mechanical activation served to reduce particle size and promote the formation of a defect-tolerant hybrid system suitable for interfacial reinforcement [71].

3.2.2. Fabrication of composite films

The polyetherimide (PEI) matrix was processed using the solution casting method. For the nanofiber-reinforced series, a 10 wt. % PEI solution in chloroform was used, while the nanoparticle-reinforced series utilized a 20 wt.% PEI solution to accommodate the different filler geometries [205]. The synthesized reinforcements (ZrO_2 nanofibers or $BaZrO_3/Y_2O_3/SrTiO_3$ nanoparticles) were ultrasonically dispersed into the polymer solution at loadings of 1 wt. % and 3 wt. % relative to the polymer mass. The mixtures were then cast into films and allowed to evaporate at room temperature for 24 h. The resulting samples were designated according to their filler type and concentration:

- Nanofiber Series: PEI (neat), PEI-ZrO_2(1wt%), and PEI-ZrO_2(3wt%).
- Nanoparticle Series: PEI (neat), PEI-$BaZrO_3/Y_2O_3/SrTiO_3$(1wt%), and PEI-$BaZrO_3/Y_2O_3/SrTiO_3$(3wt%).he preparation of these two series allows for a direct

comparison between the reinforcing efficiency of hybrid nanoparticles and calcined nanofibers within the same high-performance thermoplastic matrix. The systematic preparation of the composite samples, including the synthesis of the reinforcing phases and the final film fabrication, is illustrated in Figures 3.1. and 3.2.

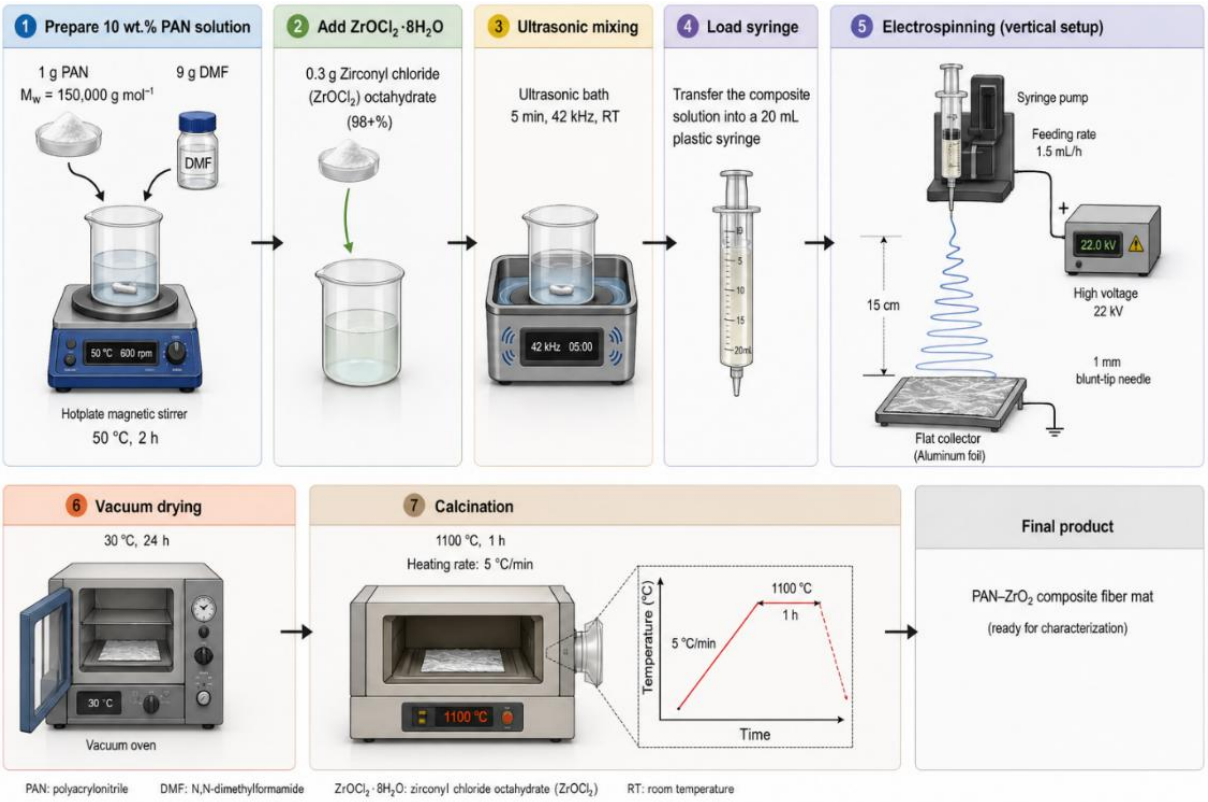

Figure 3.1. Schematic representation of the synthesis route for ZrO_2 ceramic nanofibers and the subsequent fabrication of reinforced polyetherimide films

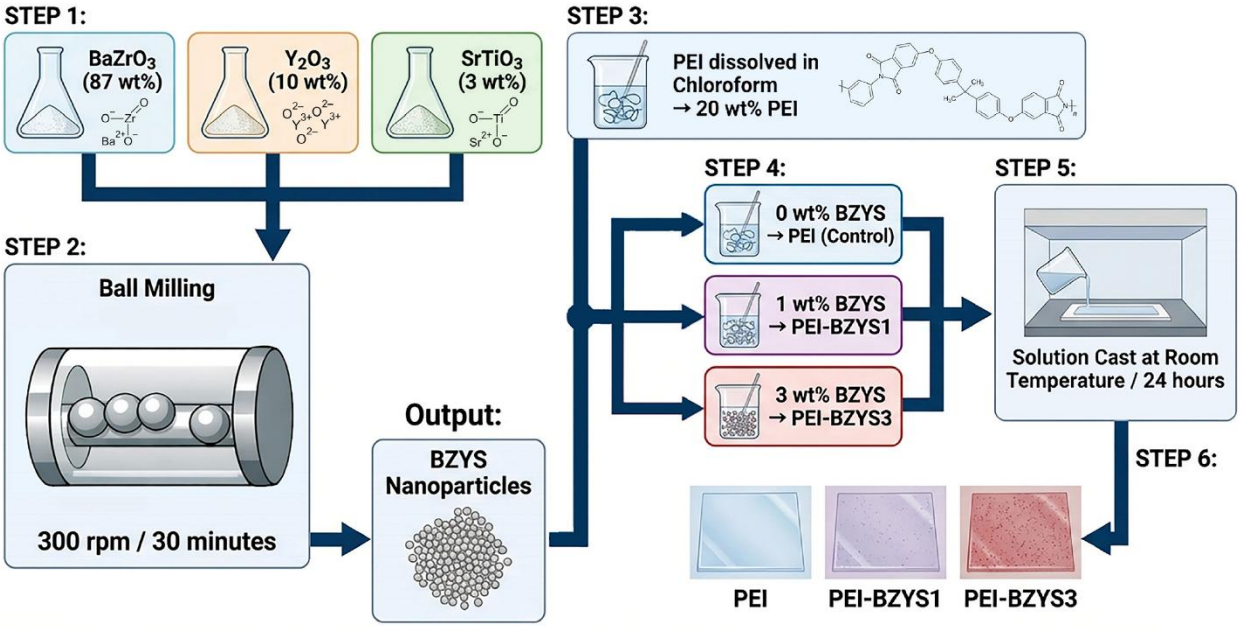

Figure 3.2. Schematic representation of the synthesis route for $BaZrO_3/Y_2O_3/SrTiO_3$ nanoparticles and the subsequent fabrication of reinforced polyetherimide films [71]

3.3. Characterization techniques

To evaluate the structural, morphological, thermal, optical, biological and mechanical properties of the developed PEI-based nanocomposites, a comprehensive suite of analytical techniques was employed.

3.3.1 Morphological and structural snalysis

3.3.1.1 Scanning Electron Microscopy (SEM) and Field Emission Scanning Electron Microscopy (FESEM)

The surface morphology, filler dispersion, and size distribution of both the ZrO_2 nanofibers and $BaZrO_3/Y_2O_3/SrTiO_3$ hybrid nanoparticles were investigated using Field Emission Scanning Electron Microscopy (FESEM) (Tescan Mira 3 and FEI Scios 2). Prior to imaging, all specimens were gold-sputtered to ensure adequate surface conductivity.

3.3.1.2 Image analysis

Quantitative assessment of the nanofiller dimensions and agglomerate sizes was performed via software image analysis using Image-Pro Plus 7.0, based on multiple representative micrographs for each sample series.

3.3.1.3 The optical properties

The optical properties and microstructural features of the composite films were examined using Polarized Optical Microscopy (POM) (Olympus CX43) equipped with a digital microphotography system (Figure 3.3.).

Figure 3.3. Optical microscope

3.3.1.4. UV-Vis spectrophotometry

The transmittance spectra of the films were recorded in the 200-800 nm wavelength range using a UV-Vis spectrophotometer (UV-2600, Shimadzu, Kyoto, Japan) presented in Figure 3.4.

Figure 3.4. UV-2600 UV-Vis spectrophotometer

3.3.1.5. Time resolved laser-induced fluorescence

3.3.1.6. X-ray Diffraction (XRD)

X-ray Diffraction (XRD) (Ital Structures APD2000) was utilized to identify the crystalline phases and calculate fundamental structural parameters, including unit cell dimensions and crystallite size. For the nanofiber series, patterns were recorded over a 2θ range of 20°–70° (step 0.1°, 10 s/step), while the nanoparticle series was scanned from 20° to 80° (step 0.02°, 1 s/step), using CuKα radiation in both cases.

3.3.1.7 Fourier Transform Infrared Spectroscopy (FTIR)

Chemical and structural changes occurring after calcination or thermal processing were monitored via Fourier Transform Infrared Spectroscopy (FTIR) (Nicolet iS5) in the wavenumber range of 4000-400 cm^{-1}.

3.3.2. Thermal Characterization

The thermal behaviour and phase transitions of the neat PEI and its composites were evaluated by Differential Scanning Calorimetry (DSC) (TA Instruments Q10). Samples were heated at a constant rate of 10 °C min^{-1} under a controlled nitrogen atmosphere (50 mL min^{-1}). The glass transition temperature (T_g) was precisely determined from the midpoint of the inflection curve during the primary heating cycle, serving as an indicator of the filler's influence on polymer chain mobility.3.3.3. Mechanical testing and statistical analysis

3.3.3.1 Microindentation

The surface mechanical properties were assessed through instrumented microindentation using a spherical indenter (4 mm diameter). The testing protocol involved a maximum load of 5 N, reached at a loading rate of 0.25 N s^{-1}, with a dwell time of 20 seconds to allow for material stabilization. Unloading was performed at the same rate, while the force-displacement data were continuously recorded. Hardness values were derived using the Oliver–Pharr analytical method. To ensure reproducibility, measurements were conducted at three distinct locations for each sample.

3.3.3.2. Nanoindentation

Nanoscale indentation and scratch measurements were performed using a Hysitron TI 950 TriboIndenter equipped with in situ scanning probe microscopy (SPM) imaging (Hysitron, Minneapolis, USA) (Figure 3.5.). A Berkovich diamond tip, characterized by a three-sided pyramidal geometry with a total included angle of 142.35°, was employed for all tests. Indentation experiments were conducted under a maximum load of 1000 μN, with at least nine indents applied at different surface locations for each sample to ensure statistical reliability. The loading protocol consisted of a 10 s linear loading segment, followed by a 5 s hold period at peak load, and a 10 s unloading stage.

Figure 3.5. Hysitron TI 950 TriboIndenter device

The impact of ZrO_2 nanofibers and $BaZrO_3/Y_2O_3/SrTiO_3$ nanoparticles on the composite properties was evaluated via one-way analysis of variance (ANOVA) using Origin 9 software. This statistical approach allowed for the determination of significance levels ($p < 0.05$) regarding the reinforcement efficiency of the different filler systems.

Nanoscratch testing was carried out to evaluate the coefficient of friction (CoF) by simultaneously recording the normal force (NF) and lateral force (LF). In each test, the indenter was initially loaded over 5 s to reach a normal force of 500 μN, followed by a constant-load scratching phase performed at a sliding velocity of 0.33 μm/s over a total scratch length of 10 μm. The test concluded with a 3 s unloading segment. A minimum of three scratches were performed at different surface positions. The reduced elastic modulus (E), indentation hardness (H), and coefficient of friction (CoF) were determined using standard analysis procedures described previously.

4. RESULTS AND DISCUSSION

4.1. Polyetherimide reinforced with ZrO_2 nanofibers

4.1.1. Morphology of PAN-$ZrOCl_2$ electrospun fibers

Figure 4.1. presents the FESEM analysis of the electrospun precursor fibers before thermal treatment. The freshly electrospun PAN-$ZrOCl_2$ fibers exhibit a continuous, smooth, and bead-free morphology, confirming that the selected electrospinning conditions enabled stable jet formation and uniform fiber deposition. The absence of beads indicates an appropriate balance between polymer chain entanglement, solution viscosity, precursor loading, feeding rate, applied voltage and tip-to-collector distance. In this stage, PAN acts as the spinnable carrier matrix, while zirconyl chloride is homogeneously incorporated within the polymer solution. The smooth fiber surface suggests that the inorganic precursor was sufficiently dispersed in the PAN/DMF system and did not induce severe phase separation or crystallization during solvent evaporation. The corresponding diameter distribution shows that nearly 80% of the fibers had diameters below 1 μm, confirming the formation of submicrometric precursor fibers with relatively narrow dimensional variability. This morphology is important because the initial continuity and uniformity of the electrospun precursor directly influence the preservation of the fibrous architecture during subsequent thermal conversion.

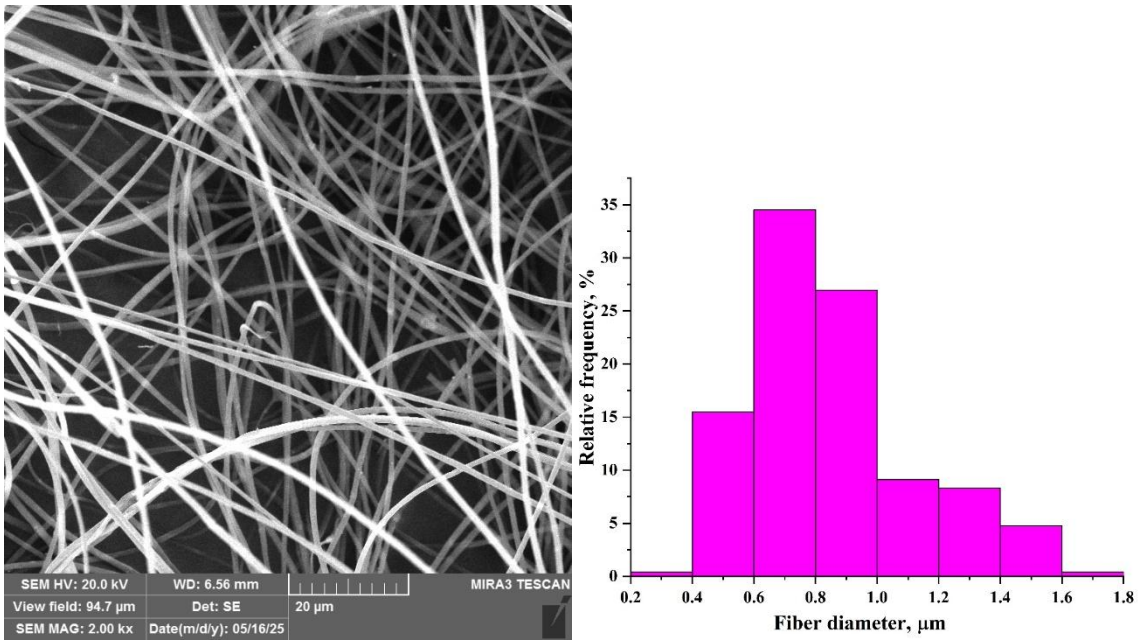

Figure 4.1. FESEM image (left) and fiber size distribution (right) of electrospun composite fibers

4.1.2. Morphology of calcined ZrO_2 fibers

After calcination, the morphology changes markedly because PAN decomposes and is removed from the system, while zirconyl species are converted into ZrO_2 ceramic nanofibers (Figure 4.2.). Therefore, the calcined fibers should not be described as PAN-containing composite fibers, but rather as ceramic ZrO_2 fibers derived from the PAN-$ZrOCl_2$ precursor. The thermal treatment causes pronounced shrinkage of the fibers, which is reflected in the substantial reduction of fiber diameter [209]. This shrinkage originates from solvent removal, polymer burnout, decomposition of the organic phase and densification/crystallization of the inorganic

zirconia phase. The diameter distribution of the calcined fibers (Figure 4.2.) shows that more than 50% of the fibers had diameters up to 100 nm, demonstrating successful conversion of the submicrometric precursor fibers into nanoscale ceramic fibers.

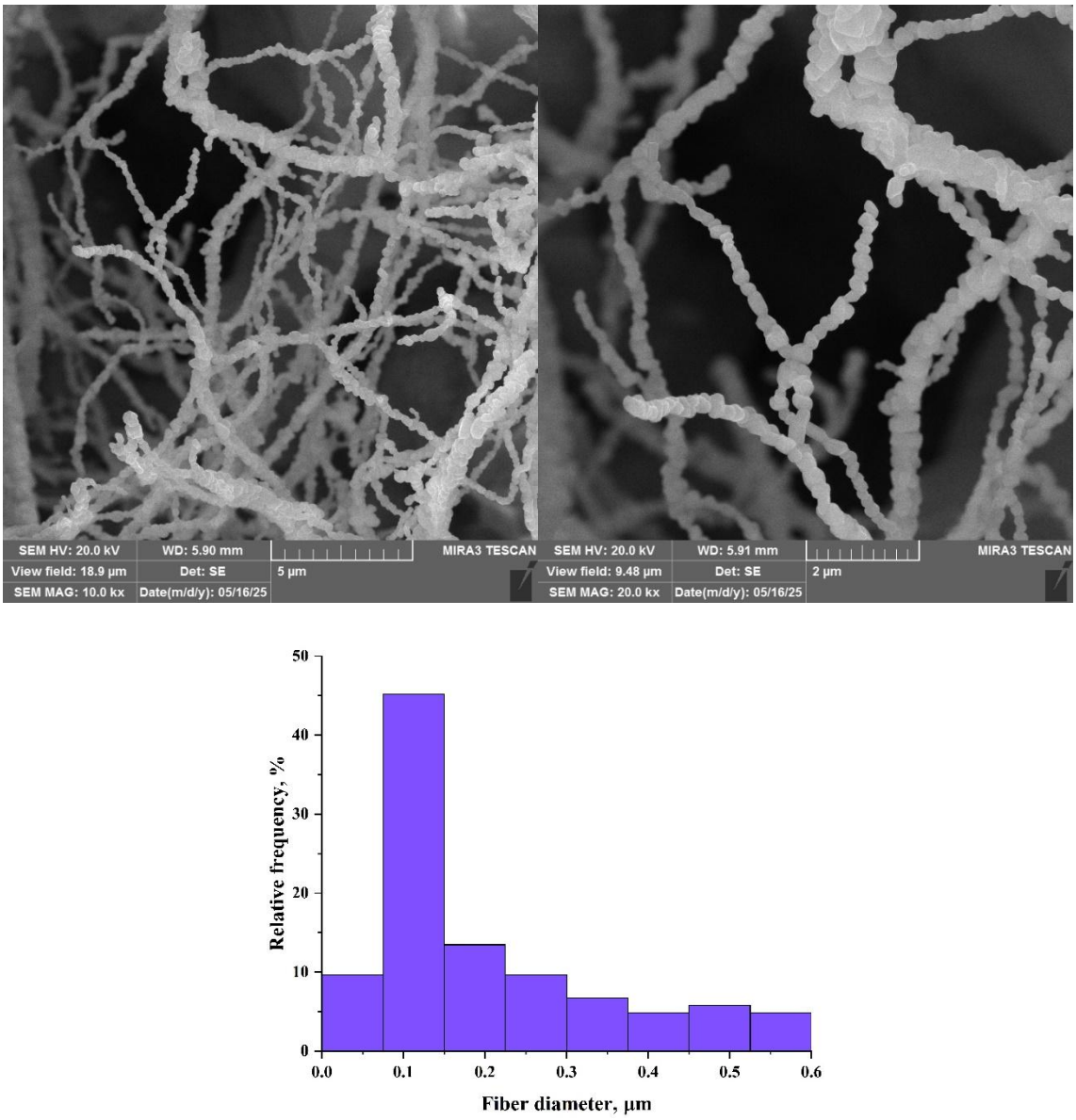

Figure 4.2. FESEM image and size distribution of ZrO_2 nanofibers

The surface of the calcined ZrO_2 fibers becomes considerably rougher and more granular compared with the as-spun fibers. This morphology is consistent with nucleation, growth and partial coalescence of zirconia grains during high-temperature calcination. The higher-magnification image (20000 x) reveals that the fibers are composed of closely packed or stacked ceramic grains, rather than a continuous polymeric phase [210]. Such a grain-built architecture indicates that the original electrospun fiber template was preserved during calcination, while the internal structure was transformed into a polycrystalline ceramic network. The rough surface and grain boundaries may be beneficial for reinforcement applications, because they can improve mechanical anchoring and interfacial contact when the ZrO_2 nanofibers are incorporated into polymer matrix. In addition, the nanoscale diameter of the calcined fibers provides a high aspect ratio and large specific surface area, both of which

are advantageous for stress transfer, crack deflection and mechanical interlocking within composite films.
Overall, Figures 4.1. and 4.2. confirm a successful two-step transformation: first, the formation of smooth and uniform PAN-$ZrOCl_2$ electrospun precursor fibers, and second, their thermal conversion into thinner, rougher, polycrystalline ZrO_2 ceramic nanofibers after PAN removal. This morphological evolution is essential for understanding the reinforcing potential of the final ceramic fibers, since the calcined ZrO_2 network combines preserved fibrous geometry, nanoscale diameter and a grain-structured surface capable of promoting stronger interaction with polymer.

4.1.3. Structural analysis of fibers

Figure 2 shows FTIR spectra of the as-spun PAN-$ZrOCl_2$ precursor fibers and the calcined ZrO_2 nanofibers, while the main vibrational assignments are summarized in Table 4.1. The spectra clearly demonstrate the chemical transformation that occurs during calcination, from an organic-inorganic PAN/zirconyl chloride precursor system to an inorganic zirconia fibrous network.

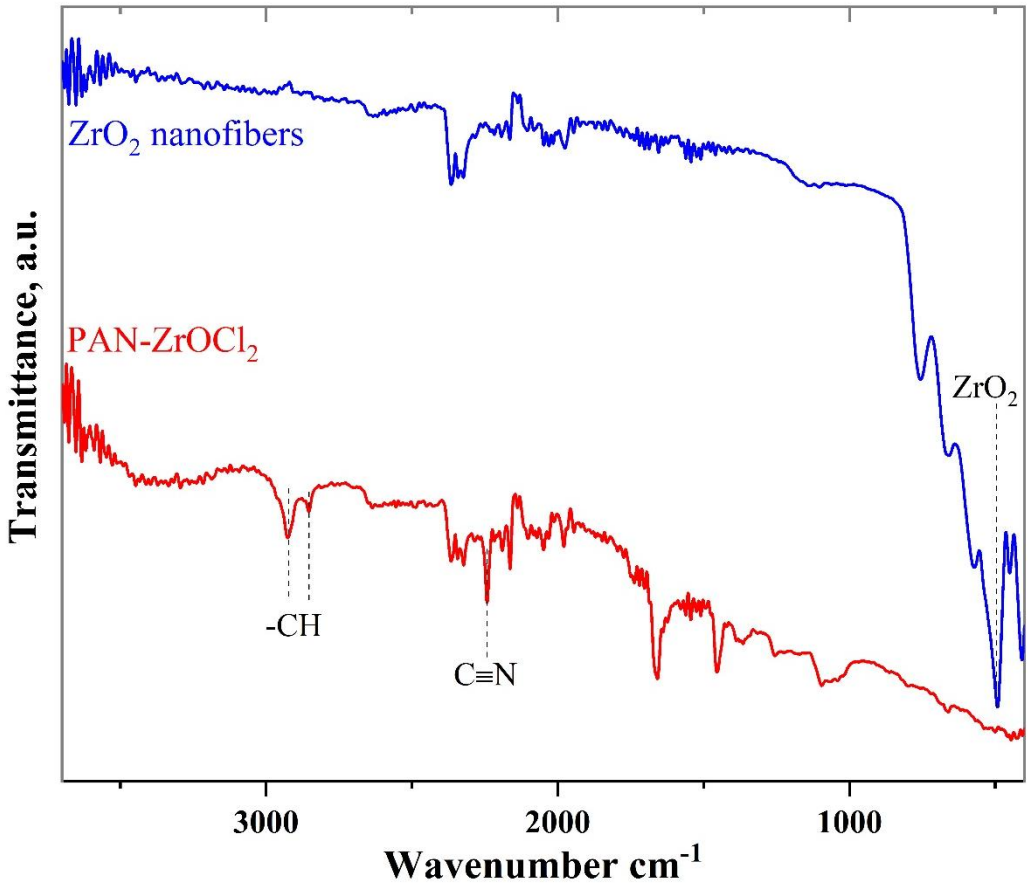

Figure 4.3. FTIR spectra of electrospun and calcined fibers

In the as-spun PAN-$ZrOCl_2$ fibers, the spectrum is dominated by bands characteristic of PAN and residual solvent/precursor components. The bands at 2927 and 2850 cm^{-1} are assigned to

asymmetric and symmetric stretching vibrations of aliphatic $–CH_2$ groups in the PAN backbone. The intense absorption at 2246 cm^{-1} corresponds to the stretching vibration of nitrile groups, C≡N, which represents the most characteristic FTIR marker of PAN. The presence of this band confirms that the polymeric PAN phase was preserved after electrospinning and that the as-spun fibers still possess the expected chemical structure of the precursor polymer. The band observed near 1662 cm^{-1} may be related to overlapping contributions from absorbed water, residual DMF and possible carbonyl-related vibrations from the solvent environment. Since DMF was used as the solvent, this band suggests that a small amount of solvent or solvent-associated species may remain trapped within the electrospun fibers before thermal treatment. The absorption at approximately 1455 cm^{-1} is attributed to $–CH_2$ bending vibrations of PAN, while the band at 1247 cm^{-1} can be assigned to C–N stretching vibrations. Together, these bands confirm the organic nature of the as-spun fibers and indicate that PAN acts as the structural carrier enabling continuous fiber formation during electrospinning.

After calcination at 1100 °C, the FTIR spectrum changes completely. The PAN-related bands at 2927, 2850, 2246, 1455 and 1247 cm^{-1} disappear, confirming the thermal decomposition and removal of the organic polymer phase. This result is especially important because the final material should no longer be described as PAN-containing fibers, but as ZrO_2 ceramic nanofibers derived from the PAN-$ZrOCl_2$ precursor. The disappearance of the nitrile band at 2246 cm^{-1} is a direct indication that the PAN backbone was destroyed during heat treatment, while the absence of aliphatic $–CH_2$ bands confirms the elimination of hydrocarbon fragments from the system. The calcined sample exhibits several intense bands in the low-wavenumber region, particularly in the region 751-408 cm^{-1}. These bands are assigned to Zr–O lattice vibrations and confirm the formation of zirconium dioxide. The sharp features below 600 cm^{-1} are consistent with the vibrational modes of crystalline ZrO_2, including contributions commonly associated with monoclinic and tetragonal zirconia phases. Therefore, the FTIR results support the successful conversion of zirconyl chloride species into zirconia during calcination [211]. The appearance of well-defined Zr–O bands, combined with the complete disappearance of PAN-related vibrations, demonstrates that the thermal treatment induced both organic phase burnout and inorganic phase crystallization.

Overall, FTIR analysis confirms a two-stage chemical evolution. Before calcination, the fibers consist of a PAN-based organic matrix containing zirconium precursor species and possible residual DMF. After calcination, the organic matrix is completely removed, and the remaining fibrous material consists of ZrO_2, as evidenced by the dominant Zr–O vibrational bands. These results agree with previous reports showing that high-temperature treatment of PAN-based electrospun precursors eliminates nitrile and aliphatic functional groups and enables the formation of ceramic oxide fibers [27]. Thus, Figure 4.3. provides strong chemical evidence for the successful transformation of electrospun PAN-$ZrOCl_2$ precursor fibers into ceramic ZrO_2 nanofibers.

Table 4.1. Main FTIR bands of as-spun PAN-$ZrOCl_2$ fibers and calcined ZrO_2 nanofibers

Wavenumber, cm^{-1}	Sample	Assignment	Interpretation
2927	As-spun PAN-$ZrOCl_2$	Asymmetric $–CH_2$ stretching	PAN backbone vibration
2850	As-spun PAN-$ZrOCl_2$	Symmetric $–CH_2$ stretching	Aliphatic PAN chain vibration
2246	As-spun PAN-$ZrOCl_2$	C≡N stretching	Characteristic nitrile band of PAN
1662	As-spun PAN-$ZrOCl_2$	H–O–H bending/C=O stretching	Residual water and/or DMF contribution
1455	As-spun PAN-$ZrOCl_2$	$–CH_2$ bending	PAN backbone deformation
1247	As-spun PAN-$ZrOCl_2$	C–N stretching	PAN-related vibration
751	Calcined ZrO_2	Zr–O vibration	Formation of zirconia lattice
662	Calcined ZrO_2	Zr–O vibration	Zirconia lattice mode
572	Calcined ZrO_2	Zr–O vibration	Monoclinic/tetragonal ZrO_2 contribution
494	Calcined ZrO_2	Zr–O vibration	Crystalline zirconia mode
447	Calcined ZrO_2	Zr–O vibration	Zirconia lattice vibration
408	Calcined ZrO_2	Zr–O vibration	Low-frequency Zr–O mode

4.1.4. XRD analysis of synthesized ceramic ZrO_2 nanofibers

Figure 4.4. presents X-ray diffraction (XRD) pattern of the calcined sample and provides direct structural evidence for the formation of crystalline zirconium dioxide after thermal treatment of the electrospun PAN-$ZrOCl_2$ precursor fibers. The diffraction peaks are well-defined and can be fully indexed to ZrO_2, showing excellent agreement with the standard PDF card No. 78-1807, corresponding to lattice parameters $a = 5.1505$ Å, $b = 5.2116$ Å, $c = 5.3173$ Å, $\beta = 99.23°$, and unit cell volume $V = 140.9$ Å^3. No additional reflections related to residual precursor phases (e.g., $ZrOCl_2$) or carbonaceous species are observed, which confirms the complete conversion of the precursor and the absence of secondary crystalline phases within the detection limits of XRD.

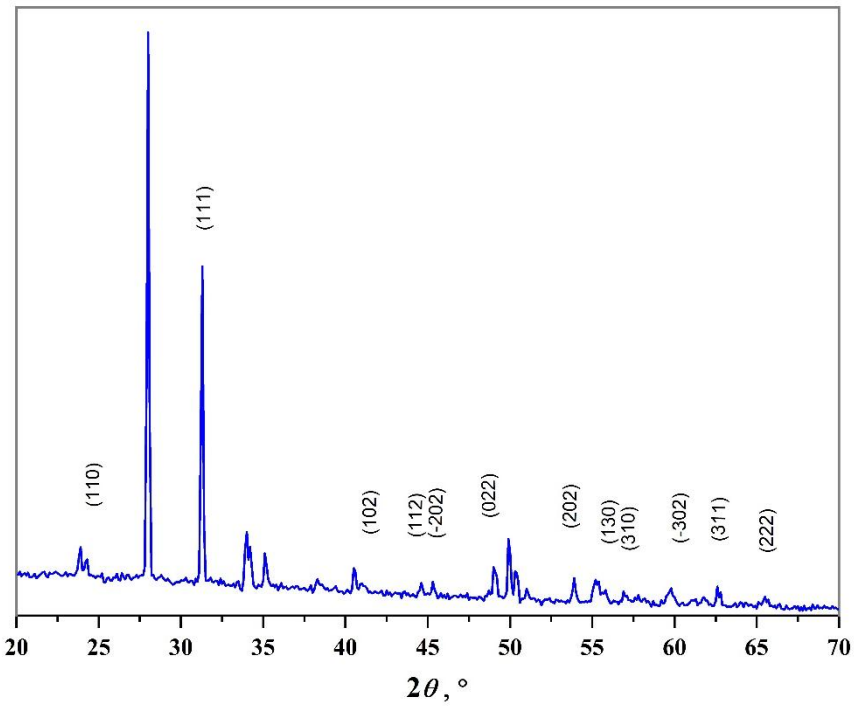

Figure 4.4. XRD pattern of ZrO_2 nanofibers

The diffraction pattern clearly indicates that ZrO_2 crystallizes in the monoclinic phase, belonging to the *P*21/c space group. The presence of characteristic monoclinic reflections, typically located around $2\theta \approx 28°$, 31°, 34°, 50° and 60°, confirms the thermodynamically stable phase of zirconia at the applied calcination temperature (1100 °C). The absence of peaks corresponding to tetragonal or cubic ZrO_2 suggests that the system underwent complete phase transformation into the monoclinic structure during cooling, which is consistent with the known phase stability of zirconia in the absence of stabilizing dopants. The relatively sharp and intense diffraction peaks indicate a high degree of crystallinity of the formed ZrO_2 nanofibers [212]. This observation is consistent with the high calcination temperature, which promotes crystal growth, phase ordering, and removal of structural defects associated with the precursor stage. Importantly, the preservation of the fibrous morphology observed in FESEM, combined with the crystalline features revealed by XRD, suggests that the material consists of polycrystalline ceramic fibers composed of interconnected ZrO_2 grains. The average crystallite size (D) of ZrO_2 was estimated using the Scherrer equation:

$$D = K \times \lambda/(\beta \times \cos\Theta)\P$$

where K is the shape factor, λ is the X-ray wavelength, β is the full width at half maximum (FWHM), and θ is the Bragg angle [31]. The calculated average crystallite size is 57 nm, indicating that each fiber is composed of nanoscale crystalline domains. This value is in good agreement with the FESEM observations, where a grain-like substructure was identified within the fibers after calcination. To further assess the crystalline quality, the dislocation density (δ), which reflects the concentration of lattice imperfections, was calculated using the relation:

$$\delta = 1/D^2$$

The obtained value, $\delta = 3.0 \times 10^{-4}$ nm^{-2}, is relatively low, indicating a limited density of crystallographic defects within the zirconia lattice. Such a low dislocation density is typically associated with well-developed crystalline domains and suggests that the applied thermal treatment was sufficient to promote structural relaxation and defect reduction. This is particularly relevant for applications where mechanical stability and chemical durability are required, as defect density can significantly influence both properties. From a structure–property perspective, the combination of monoclinic phase purity, nanoscale crystallite size, and low dislocation density indicates that the obtained ZrO_2 nanofibers possess a well-ordered crystal structure with limited internal strain. The nanoscale crystallite size contributes to a high specific surface area, while the polycrystalline fibrous architecture ensures mechanical integrity. When incorporated into polymer matrices, such fibers are expected to provide efficient load transfer and improved interfacial interactions due to their crystalline stability and surface characteristics. Overall, the XRD results confirm the successful transformation of electrospun PAN-$ZrOCl_2$ precursor fibers into phase-pure, highly crystalline monoclinic ZrO_2 nanofibers. The absence of secondary phases, combined with favorable crystallite size and defect characteristics, highlights the effectiveness of the applied synthesis and calcination route in producing structurally well-defined ceramic nanofibers.

4.1.5. FESEM analysis of PEI-ZrO_2 composites

Figure 4.5. presents a FESEM PEI composite films reinforced with ZrO_2 nanofibers, providing complementary insight into both microstructural dispersion and agglomerate size distribution. Table 4.2. presented size distribution of ZrO_2 nanofibers, which created whisker-like shapes in PEI matrix.

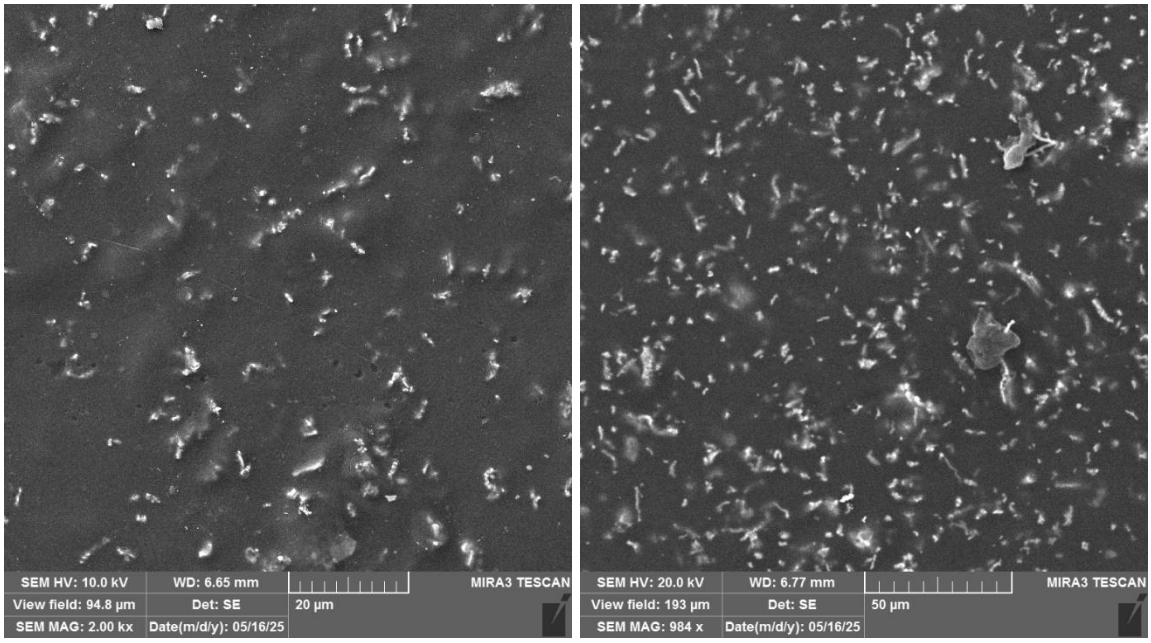

Figure 4.5. FESEM images of (a) PEI-ZrO_2(1wt%) and (b) PEI-ZrO_2(3wt%)

Table 4.2. ZrO_2 fibers' distribution size in PEI-ZrO_2(1wt%)

Length (µm)	Relative frequency (%)
< 0.5	18
0.5-1.0	34
1.0-1.5	22
1.5-2.0	12
2.0-3.0	10
> 3.0	4

Table 4.3. ZrO_2 fibers' distribution size in PEI-ZrO_2(3wt%)

Length (µm)	Relative frequency (%)
< 0.5	~12
0.5–1.0	~28
1.0–2.0	~35
2.0–3.0	~18
> 3.0	~7

The FESEM micrographs of composite films (Figure 4.5.) exhibits a finely distributed secondary phase embedded within the PEI matrix. The dispersed features appear as elongated, whisker-like structures, which can be directly associated with the incorporated ZrO_2 nanofibers. Their morphology suggests that the original fibrous architecture was at least partially preserved during dispersion, although some fragmentation into shorter segments likely occurred during ultrasonication. Importantly, these structures are relatively uniformly distributed throughout the observed composite, without evidence of large agglomerates or phase clustering in PEI-1% ZrO_2 (Figure 4.5.a). This indicates that ultrasonic homogenization was effective in overcoming fiber-fiber interactions and promoting a stable dispersion within the viscous polymer solution. An important observation from the FESEM analysis is the absence of interfacial defects such as voids, cracks, or pull-out cavities around the nanofibers.

This suggests strong interfacial adhesion between ZrO_2 and the PEI matrix, likely governed by physical interactions and possible surface compatibility between the ceramic fibers and the polymer chains. Such interfacial integrity is essential for efficient stress transfer in composite systems and directly correlates with improvements in mechanical properties, particularly stiffness and hardness, as previously observed in similar polymer-ceramic systems [205].
Quantitative analysis of the SEM micrographs reveals that the ZrO_2 phase is present in the form of whisker-like structures formed via ultrasonication-induced fragmentation of electrospun fibers. The whiskers exhibit lengths ranging from approximately 0.25 to 3.2 μm, with a median value of 1.05 μm and a mean of 1.3 μm, indicating a moderately right-skewed distribution (Table 4.2.). Approximately 52% of the structures fall within the 0.5-1.5 μm range, confirming that the dominant population consists of short, submicron-to-micron-scale segments. The whisker width is predominantly within 100-180 nm, resulting in aspect ratios of 5-8. This morphology demonstrates that ultrasonication effectively disrupts continuous fibers into dispersible reinforcement units while preserving sufficient aspect ratio for efficient stress transfer. The resulting distribution is characteristic of a balance between fragmentation and limited re-agglomeration, yielding a morphology well-suited for homogeneous dispersion within the polymer matrix.
SEM analysis of the PEI composite containing 3 wt% ZrO_2 (Figure 4.5.b) reveals a heterogeneous but well-dispersed microstructure consisting of a dominant population of whisker-like ceramic fragments accompanied by a limited number of secondary agglomerates [213]. The whiskers, formed by ultrasonication-induced fragmentation of electrospun fibers, exhibit lengths in the range of approximately 0.4-3.5 μm, with the majority falling between 0.8 and 1.8 μm and a median value of 1.3 μm (Table 4.3.). Their widths are in the range 100-220 nm, yielding aspect ratios of 4-9, confirming preservation of elongated geometry. In addition to these features, micron-scale agglomerates (2-10 μm) are observed, representing approximately 10% of the total population. These clusters arise from increased particle-particle interactions at higher filler loading and incomplete dispersion of secondary assemblies. Despite this, the overall morphology remains free of continuous aggregates, percolated networks or interfacial defects, indicating that dispersion remains sufficiently homogeneous. The increased density of whisker-like structures and reduced interparticle spacing contribute to enhanced load transfer and matrix constraint, while the limited agglomeration does not reach a critical level that would induce stress concentration. This balance between dispersion and controlled clustering is consistent with the observed increase in mechanical hardness at higher ZrO_2 loading. Table 4.4. summarizes morphological differences between PEI-ZrO_2(1wt%) and PEI-ZrO_2(3wt%) nanocomposites.

Table 4.4. Morphological differences between PEI-ZrO_2(1wt%) and PEI-ZrO_2(3wt%)

Feature	1 wt%	3 wt%
Whisker density	Moderate	High
Whisker spacing	Large	Reduced
Agglomerates	Rare	Clearly present
Distribution	Uniform	Slight clustering
Interaction	Particle-polymer dominant	Particle-particle more pronounced

4.1.6. Polarized optical microscopy of PEI-ZrO_2 composites

The polarized optical microscopy (POM) image (Figure 4.6.) further supports these revealed by FESEM by illustrating the optical response of the films. The neat PEI film appears optically uniform, displaying the characteristic amber coloration of PEI with minimal contrast variation. This uniformity confirms the amorphous nature of the polymer and the absence of internal structures capable of inducing birefringence.

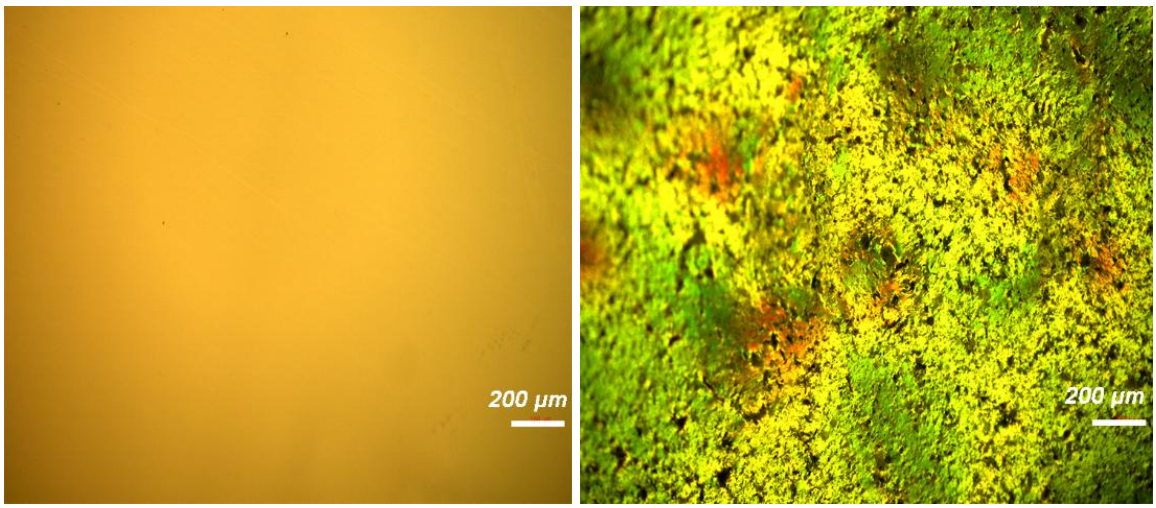

Figure 4.6. Optical microscopy of neat PEI and PEI-ZrO_2 composite

In contrast, the composite film shows pronounced heterogeneity in color and intensity, with localized bright regions and interference patterns distributed across the surface. These features are indicative of birefringence arising from the presence of anisotropic inclusions, ZrO_2 nanofibers, as well as the localized orientation of polymer chains in their vicinity. The introduction of rigid ceramic fibers can induce constraints on polymer chain mobility, leading to localized orientation or microstructural ordering, which becomes visible under polarized light [100]. Additionally, the spatial distribution of these birefringent regions correlates well with the uniform dispersion observed in FESEM, further confirming that the nanofibers are not only well distributed but also actively influence the optical behavior of the composite. The absence of large dark regions or optical discontinuities suggests that no macroscopic phase separation or aggregation occurred during processing.

Overall, the combined FESEM and POM analyses demonstrates that ZrO_2 nanofibers were successfully incorporated into the PEI matrix with a high degree of dispersion and strong interfacial compatibility. The whisker-like morphology observed in FESEM, together with the birefringent response in POM, confirms both structural integration and functional interaction between the reinforcement phase and the polymer matrix. These microstructural characteristics are expected to play a key role in enhancing the mechanical and possibly dielectric performance of the composite films.

4.1.7. Thermal analysis of PEI-ZrO_2

PEI is an intrinsically amorphous high-performance polymer, and under typical processing conditions (solution casting + moderate filler loadings), it does not crystallize. In presented DSC curves (Figure 4.7.), the presence of only a glass transition (T_g) and the absence of melting (T_m) or crystallization (T_c) peaks confirms that the matrix remains amorphous even after the addition of ZrO_2 nanofibers. If ZrO_2 acted as a nucleating agent (as fillers often do in semicrystalline polymers like PE, PP, PEEK, etc.), the following changes would occur:

- appearance of a crystallization exotherm (T_c) on cooling or reheating
- a melting endotherm (T_m)
- a change in heat capacity step (ΔC_p) associated with altered phase structure

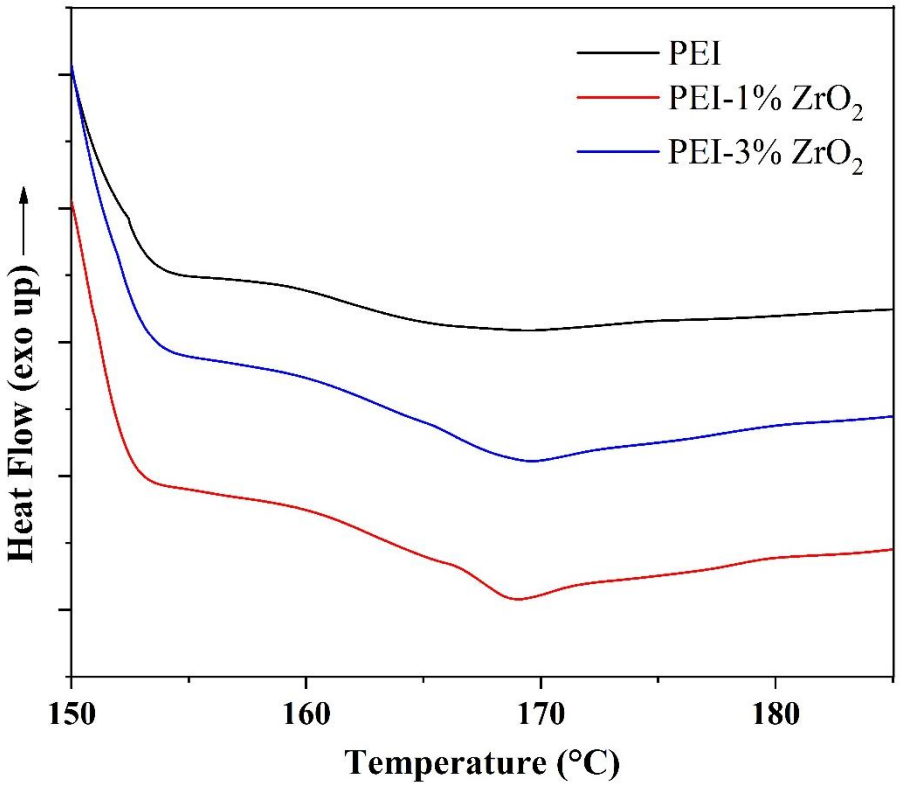

Figure 4.7. DSC thermogram of PEI and composites

The differential scanning calorimetry (DSC) thermograms of neat PEI and PEI-ZrO_2 nanocomposites are presented in Figure 4.7., while the extracted thermal parameters are summarized in Table 4.5. The glass transition temperature (T_g) of the pristine PEI matrix is observed at 165.8 °C, within the expected transition region of 150-190 °C, confirming the amorphous nature of the polymer and consistency with literature values for solution-processed

PEI systems. Upon incorporation of ZrO_2 nanofibers, a slight, but systematic increase in T_g is observed. The T_g shifts to 166.7 °C for the composite containing 1 wt% ZrO_2 and further to 167.2 °C for 3 wt% loading. Although the magnitude of this shift is relatively modest (≈1-1.5 °C), the trend is consistent and indicative of subtle changes in polymer chain dynamics induced by the presence of the ceramic phase. This behavior can be interpreted in terms of restricted segmental mobility of PEI chains in the vicinity of the ZrO_2 nanofibers. The high surface area and rigid nature of the ceramic fibers introduce an interfacial region where polymer chains experience physical confinement and reduced mobility [214]. Even in the absence of strong chemical bonding, such interfacial interactions, often described as weak chain-filler interactions, can lead to the formation of a partially immobilized polymer layer surrounding the filler surface. As a result, a higher thermal energy is required to activate cooperative segmental motion, which manifests as an increase in T_g. However, the relatively small shift in T_g suggests that the extent of this interfacial immobilization is limited. This is expected for low filler loadings (1-3 wt%) and composites where the interaction between filler and polymer is primarily physical rather than chemical. In such cases, the volume fraction of the interfacial region is not sufficiently large to significantly alter the bulk thermal response of the polymer matrix. Therefore, the observed T_g increase reflects a balance between localized chain restriction near the nanofiber surface and the dominant behavior of the bulk amorphous PEI phase. It is also important to note that no additional thermal transitions (e.g., melting peaks or crystallization exotherms) are observed in the DSC curves, confirming that the introduction of ZrO_2 nanofibers does not induce crystallization within the PEI matrix. This further supports the conclusion that the polymer remains predominantly amorphous, and that the nanofibers act as passive reinforcing elements rather than nucleating agents. From a structure-property standpoint, the slight increase in T_g suggests that the ZrO_2 nanofibers contribute to enhanced thermal stability without compromising the intrinsic amorphous nature and processability of PEI, which should lead to an increase in mechanical performance. Such behavior is advantageous for applications requiring dimensional stability at elevated temperatures, as even minor increases in T_g can improve resistance to thermal softening.

Table 4.5. Glass transition temperatures of neat PEI and PEI-ZrO_2 nanocomposites

Sample	**ZrO_2 content (wt%)**	**T_g (°C)**	**ΔT_g (°C)**
PEI	0	165.8	–
PEI-ZrO_2(1wt%)	1	166.7	+0.9
PEI-ZrO_2(3wt%)	3	167.2	+1.4

Although no crystallization or melting transitions were observed in the DSC thermograms, indicating that the PEI matrix remains fully amorphous, the POM analysis reveals pronounced birefringence in the composite films. This apparent discrepancy can be explained by the presence of localized chain orientation rather than true crystalline ordering. The incorporation of ZrO_2 nanofibers introduces anisotropic constraints within the polymer matrix, leading to the formation of interfacial regions where polymer chains are partially aligned. These regions exhibit optical anisotropy and are therefore visible under polarized light, despite the absence of long-range crystalline structure. The slight increase in T_g further supports this interpretation, as it reflects restricted segmental mobility within these interphase regions. Therefore, ZrO_2 nanofibers do not induce crystallization in PEI, but instead generate an anisotropic interphase

that modifies chain dynamics and optical response without altering the amorphous nature of the matrix.

4.1.8. UV–Vis analysis

The UV–Vis transmittance spectra of neat PEI and PEI-ZrO_2(3wt%) nanocomposite are presented in Table 4.6. The results clearly demonstrate the influence of ZrO_2 nanofibers on the optical behavior of the polymer matrix. Neat PEI exhibits high optical transparency across the visible region, with a transmittance of approximately 85% at 600 nm, which is consistent with its amorphous structure and absence of light-scattering heterogeneities. The sharp increase in transmittance around ~400 nm corresponds to the intrinsic absorption edge of PEI, associated with electronic transitions within the polymer backbone. Beyond this region, the relatively flat and high transmittance profile indicates minimal absorption and scattering losses, confirming the optical clarity of the pristine material. In contrast, the incorporation of ZrO_2 nanofibers leads to a noticeable reduction in transmittance, with the PEI-ZrO_2(3wt%) composite exhibiting approximately 54% transmittance at 600 nm. This decrease is not associated with increased absorption in the visible range, but is primarily governed by light scattering mechanisms [215]. The introduction of ceramic nanofibers creates numerous polymer-filler interfaces, and the significant refractive index mismatch between PEI ($n \approx 1.6$-1.7) and ZrO_2 ($n \approx 2.1$-2.2) results in strong scattering of incident. As the filler content increases, the density of these scattering centres rises, leading to a progressive attenuation of transmitted light.

Table 4.6. Optical transmittance of neat PEI and PEI-ZrO_2 composite

Sample	ZrO_2 content (wt%)	Transmittance at 600 nm (%)	Optical behavior
PEI	0	~85	High transparency, minimal scattering
PEI-ZrO_2(3wt%)	3	~54	Reduced transparency due to interfacial scattering

Additionally, the fibrous morphology of ZrO_2 plays an important role. Unlike spherical nanoparticles, high-aspect-ratio nanofibers act as anisotropic scattering centres, enhancing diffuse scattering and further reducing optical transparency. This interpretation is consistent with FESEM observations, which confirmed a uniform dispersion of whisker-like structures throughout the matrix. Even in the absence of large agglomerates, the cumulative scattering effect of well-dispersed nanofibers is sufficient to significantly alter optical transmission. The slight tailing of the absorption edge toward longer wavelengths (UV-visible boundary) in the composite suggests additional contributions from interfacial regions. These may arise from localized electronic states or increased disorder at the polymer-ceramic interface, which can introduce weak sub-bandgap absorption. However, this effect remains minor compared to scattering and does not dominate the optical response. Importantly, the reduction in transparency should not be interpreted as a drawback alone, but rather as a tunable property. The observed UV-edge behavior further indicates that the composite may selectively attenuate shorter wavelengths, which could be exploited to improve device lifetime in optoelectronic systems. Overall, UV–Vis analysis confirms that the incorporation of ZrO_2 nanofibers modifies the optical response of PEI primarily through scattering mechanisms, while preserving a reasonable level of transparency. When considered together with the mechanical and thermal results, the composite exhibits a well-balanced multifunctional profile, making it suitable for applications requiring both structural integrity and controlled optical performance.

4.1.9. Microhardness

The microindentation results for neat PEI and PEI-ZrO_2 nanocomposites are presented in Figure 4.8., while the corresponding quantitative values are summarized in Table 4.7. A pronounced enhancement in both hardness (H) and reduced modulus of elasticity (E_r) is observed with the incorporation of ZrO_2 nanofibers, indicating an effective reinforcement of the polymer matrix. For the neat PEI sample, relatively low hardness and modulus values are recorded, which is consistent with its amorphous structure and inherent chain mobility. Upon the addition of 1 wt% ZrO_2, the hardness increases by approximately 140%, while further increasing the filler content to 3 wt% results in an overall improvement of 163%. A similar trend is observed for the reduced modulus, which increases by 42% and 90% for 1 wt% and 3 wt% ZrO_2, respectively. These results clearly demonstrate a strong dependence of mechanical performance on nanofiber loading.

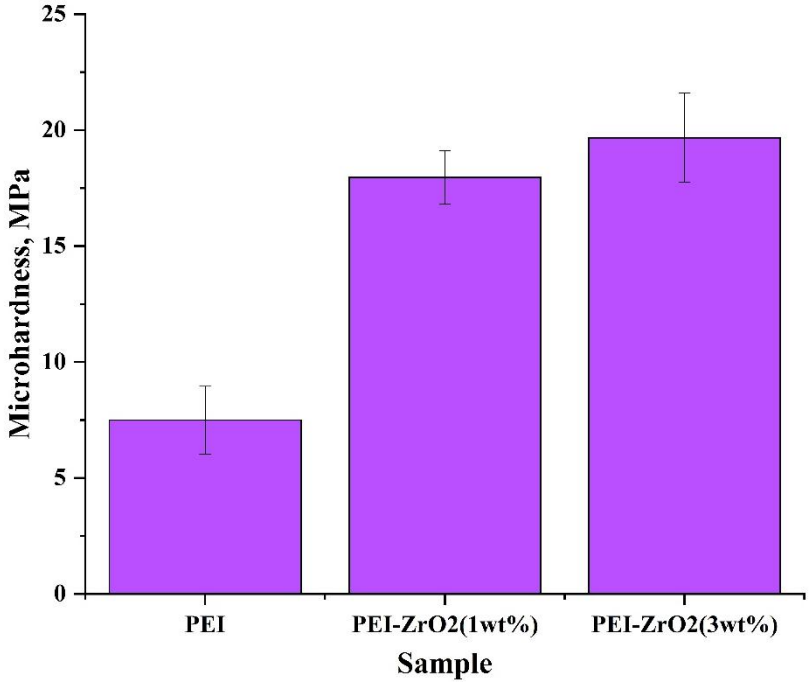

Figure 4.8. Microhardness of PEI and PEI-ZrO_2 nanocomposites

The statistical analysis further confirms the significance of these improvements. One-way ANOVA indicates that both hardness ($p < 0.001$) and reduced modulus ($p < 0.01$) differ significantly across the tested groups. Post-hoc Tukey analysis reveals statistically significant differences between neat PEI and both composites PEI-ZrO_2(1wt%) and PEI-ZrO_2(3wt%), confirming that even low filler loadings produce measurable and reliable enhancements in mechanical properties. The observed improvements can be directly correlated with the microstructural features discussed earlier. FESEM analysis (Figure 4.5.) showed that ZrO_2 nanofibers are well dispersed within the PEI matrix and exhibit a whisker-like morphology with high aspect ratio. Such geometry is highly favorable for reinforcement, as it enables the formation of an interconnected load-bearing network within the polymer. Under indentation, stress is efficiently transferred from the softer polymer matrix to the rigid ceramic nanofibers, resulting in increased resistance to plastic deformation and higher hardness values.

Table 4.7. Microindendation results

Sample	Hardness, MPa	Standard deviation	Reduced modulus of elasticity, MPa	Standard deviation
PEI	7.49468	1.45401	960.7622	90.8041
PEI-ZrO_2(1wt%)	17.96119	1.1398	1363.942	94.8086
PEI-ZrO_2(3wt%)	19.67095	1.93457	1825.334	181.1541

In addition to load transfer, the presence of ZrO_2 nanofibers induces localized restriction of polymer chain mobility, as evidenced by the slight increase in T_g observed in DSC analysis. This interfacial constraint leads to the formation of a mechanically stiffer interphase region surrounding the nanofibers. Although this interphase is not detectable as a separate phase in DSC (due to its limited volume fraction), it plays a crucial role in enhancing stiffness and modulus at the microscale [216]. The combined effect of rigid filler reinforcement and constrained polymer dynamics explains the simultaneous increase in both hardness and reduced modulus.

The absence of interfacial defects such as voids or cracks (as observed in FESEM) further supports efficient stress transfer. Poor interfacial adhesion would typically result in debonding or fiber pull-out under load, leading to reduced mechanical performance. In contrast, the current system exhibits strong interfacial compatibility, allowing the nanofibers to act as effective stress-bearing elements. Importantly, the continuous increase in both hardness and modulus with increasing filler content suggests that the system has not reached a critical filler concentration at which agglomeration or stress concentration effects would become detrimental. At higher loadings, such effects often lead to reduced reinforcement efficiency due to poor dispersion and defect formation. However, at 1-3 wt% ZrO_2, the dispersion remains sufficiently uniform to maintain effective load distribution throughout the matrix. Linking these results with POM observations, the birefringent regions observed in the composite films can be associated with anisotropic interfacial zones and nanofiber alignment, which contribute to mechanical reinforcement. Overall, the microindentation results demonstrate that ZrO_2 nanofibers act as highly effective reinforcing agents in PEI, primarily through a combination of high intrinsic stiffness of the ceramic phase, uniform dispersion and high aspect ratio enabling efficient stress transfer and formation of an interfacial constrained polymer region. This synergistic reinforcement mechanism leads to substantial improvements in hardness and modulus, even at low filler loadings. Therefore, the enhanced mechanical response arises from the combined effect of high filler stiffness, preserved whisker-like geometry, effective dispersion and interfacial constraint within the PEI matrix.

From a structure–property perspective, these results confirm that the combination of nanoscale

4.1.10. Nanoindentation and nanoscratch test of neat PEI and composite films

Representative scanning probe microscopy (SPM) image of indentation topography of PEI, PEI-ZrO_2(1wt%) and PEI-ZrO_2(3wt%) composite are shown in Figure 4.9. The incorporation of ZrO_2 nanofibers leads to a measurable improvement in both nanohardness (*H*) and reduced modulus of elasticity (*E*), confirming reinforcement at the nanoscale [217].

(a) PEI (b) PEI-ZrO_2(1wt%)

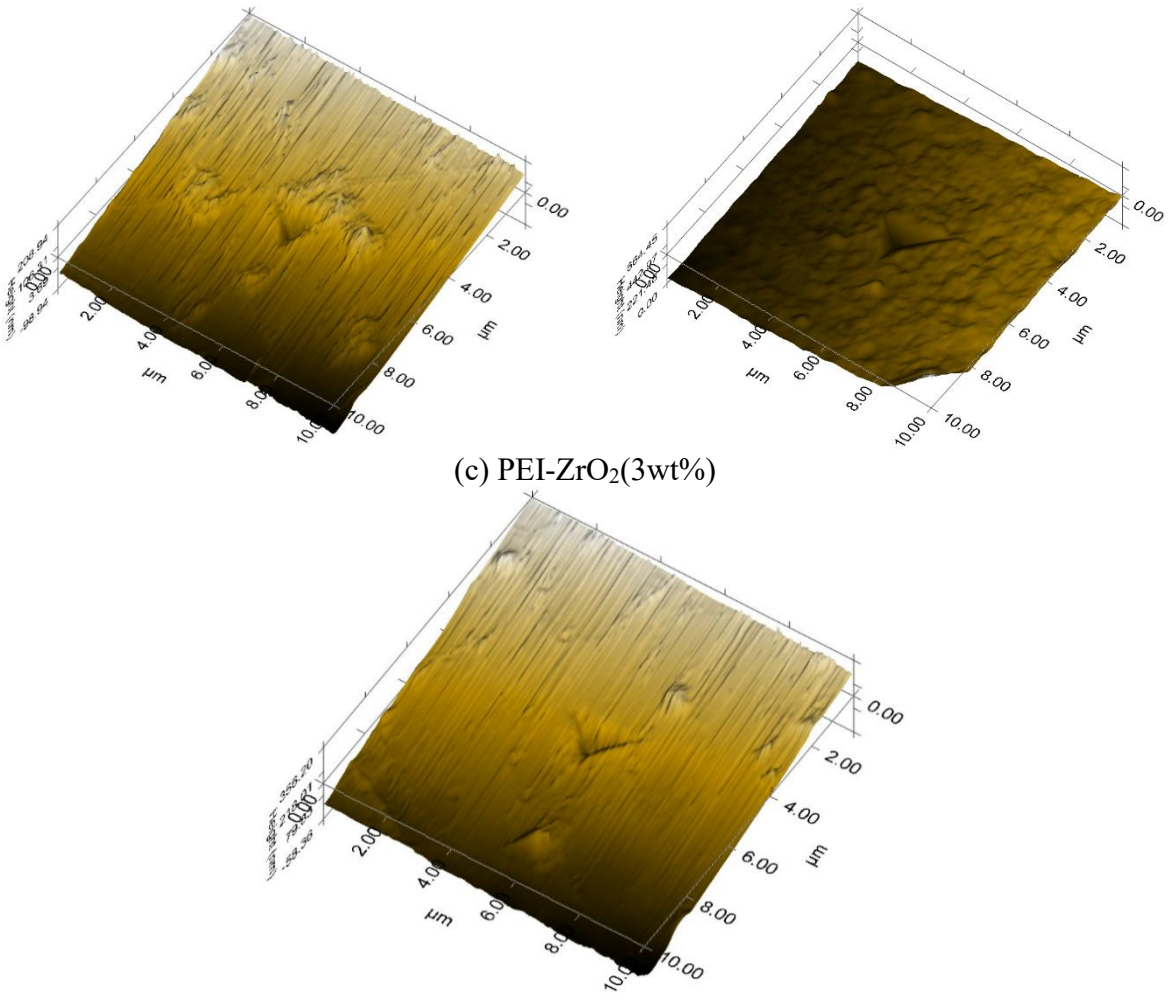

(c) PEI-ZrO_2(3wt%)

Figure 4.9. Scanning probe microscopy images of PEI in PEI-ZrO_2 composites

The hardness increases from 0.3432 GPa for neat PEI to 0.3775 GPa for the PEI-ZrO_2(3wt%) composite, corresponding to an improvement of approximately 10%. Similarly, the reduced modulus rises from 4.75 GPa to 5.51 GPa, representing a 14% increase. Although these enhancements are less pronounced than those observed in microindentation, they are highly significant because nanoindentation probes localized mechanical response, which is strongly influenced by interfacial regions and nanoscale dispersion rather than bulk averaging effects. The observed increase in hardness can be attributed to a reduction in the effective free volume within the polymer matrix. The introduction of rigid ZrO_2 nanofibers constrains the mobility of nearby PEI chains, leading to the formation of a physically crosslinked interphase region. This results in increased resistance to localized plastic deformation under the indenter tip. In addition, the high stiffness of the ceramic nanofibers contributes directly to load-bearing, especially when the indentation depth approaches the scale of the interphase thickness. The SPM 3D topographical images of the residual indents provide insight into the deformation mechanisms. Both samples exhibit well-defined, symmetric indent geometries without evidence of material pile-up (upthrow), cracking or collapse around the indentation site. This indicates that the deformation is predominantly elastic-plastic and homogeneous, without brittle fracture or interfacial debonding. The preservation of indent shape in the composite sample suggests that the addition of ZrO_2 does not compromise the structural integrity of the matrix but rather enhances its resistance to penetration. The composite surface appears slightly more resistant to indentation depth, consistent with the higher modulus. This supports the

interpretation that the nanofibers act as a reinforcing skeleton within the matrix, distributing the applied load and limiting localized deformation. From a multiscale perspective, the difference between nanoindentation and microindentation results is particularly informative. While microindentation showed a much larger increase in hardness, nanoindentation reflects the intrinsic material response at the nanoscale, where the indenter may probe regions with varying local filler concentration. This suggests that reinforcement is highly effective at the macroscale due to the formation of a percolated or semi-continuous reinforcing network, whereas at the nanoscale, the response depends on the proximity to individual nanofibers and interphase zones.

The nanoscratch results further complement the nanoindentation findings. The coefficient of friction (CoF) for neat PEI ranges from 0.40 to 0.50, in agreement with literature values, while the PEI-ZrO_2(3wt%) composite exhibits slightly higher values in the range of 0.50 to 0.60. This increase in CoF can be explained by several concurrent mechanisms. First, the embedded ZrO_2 nanofibers act as rigid asperities that increase surface roughness at the microscale, leading to higher resistance during sliding. Second, the nanofibers restrict interlayer slippage of polymer chains, thereby increasing shear resistance. During scratching, part of the polymer material may adhere to the indenter tip, forming a so-called *transfer film*. In neat PEI, this film can act as a lubricating layer, reducing friction. However, in the composite, the presence of hard zirconia nanofibers disrupts the formation and stability of this transfer film. Moreover, the nanofibers can exert a micro-scraping effect on the contact interface, continuously removing or destabilizing the transfer layer, which leads to an increase in friction coefficient. Importantly, the absence of cracks or delamination during scratching indicates that the composite maintains good cohesion and interfacial bonding even under shear loading conditions. This is consistent with the FESEM observations, where no interfacial defects were detected, and supports the conclusion that stress is effectively transferred between the matrix and the reinforcement phase. From an application standpoint, the simultaneous increase in hardness, modulus and friction coefficient suggests enhanced wear resistance, which is particularly relevant for applications such as dental restorations, where materials are subjected to repeated mechanical and tribological loading. The zirconia nanofibers provide a dual function: they improve resistance to surface deformation while also stabilizing the material under sliding contact. Overall, nanoindentation and nanoscratch analyses confirm that ZrO_2 nanofibers enhance the local mechanical and tribological performance of PEI through a combination of interfacial chain restriction, load transfer, and surface interaction mechanisms, complementing the improvements observed at the microscale.

The combined results obtained from morphological (FESEM, POM), structural (XRD), thermal (DSC), mechanical (micro- and nanoindentation), and optical (UV-Vis) analyses provide a consistent and complementary understanding of the behavior of PEI-ZrO_2 nanocomposites across multiple length scales. At the microstructural level, FESEM observations confirmed a uniform dispersion of high-aspect-ratio ZrO_2 nanofibers within the PEI matrix, without the presence of interfacial defects such as voids or cracks. This homogeneous distribution is critical, as it enables the formation of an effective load-bearing network. The whisker-like morphology of the nanofibers, combined with their polycrystalline nature (as confirmed by XRD), provides a rigid reinforcing phase capable of sustaining mechanical loads. This structural arrangement directly translates into the observed mechanical enhancements. Both microindentation and nanoindentation results show significant increases in hardness and modulus, although at different scales. At the macroscale, the formation of a semi-continuous reinforcing network leads to pronounced improvements in hardness, while at the nanoscale, the response reflects localized interactions between the polymer matrix and individual nanofibers. These results confirm that reinforcement is governed not only by filler stiffness, but also by efficient stress transfer and interfacial integrity. Thermally, DSC analysis

reveals only a slight increase in T_g, indicating that the polymer matrix remains amorphous. However, this small shift is highly informative, as it reflects the formation of a constrained interfacial region where polymer chain mobility is reduced. This interpretation is further supported by POM observations, which show birefringent domains in the composite despite the absence of crystallinity. These domains arise from localized chain orientation induced by nanofibers, rather than long-range crystalline ordering. Thus, the system can be described as an amorphous matrix containing anisotropic interphase regions that contribute to mechanical reinforcement. The optical behavior is also consistent with this microstructure. The reduction in transparency observed in UV-Vis spectra is primarily due to light scattering at polymer-ceramic interfaces, amplified by the refractive index mismatch and fibrous morphology of ZrO_2. Importantly, this confirms that the nanofibers are well dispersed throughout the matrix, as a homogeneous distribution of scattering centers is required to produce the observed optical attenuation. From a tribological perspective, the increase in coefficient of friction further supports the structural model. The ZrO_2 nanofibers act as a rigid skeleton, limiting polymer chain slippage and disrupting transfer film formation during sliding. This leads to improved wear resistance, which, together with increased hardness and modulus, highlights the suitability of the composite for mechanically demanding environments. Overall, the results demonstrate that the reinforcement mechanism in PEI-ZrO_2 nanocomposites is governed by a synergistic interplay of three key factors:

1. the intrinsic stiffness and crystallinity of ZrO_2 nanofibers,
2. their uniform dispersion and high aspect ratio enabling efficient stress transfer, and
3. the formation of an interfacial region that restricts polymer chain mobility and induces local anisotropy.

A balanced property profile makes these composites promising candidates for multifunctional applications, particularly in areas requiring a combination of structural integrity, thermal stability and controlled optical performance, such as protective coatings, electronic housings and advanced dental or biomedical materials.

4.2. Polyetherimide reinforced with $BaZrO_3/Y_2O_3/SrTiO_3$ nanoparticles

4.2.1. FESEM of particles

FESEM analysis of the $BaZrO_3/Y_2O_3/SrTiO_3$ nanoparticles (Figure 4.10.) reveals a broad and asymmetric particle size distribution. This type of distribution indicates a system dominated by fine particles, accompanied by a smaller population of larger secondary agglomerates. The measured particle diameters span a wide range, from approximately 0.07 μm to 2.49 μm, with a median value of 0.17 μm and a mean size of 0.39 μm. The noticeable difference between median and mean values reflects the statistical influence of relatively few coarse agglomerates, which skew the distribution toward higher sizes [218].

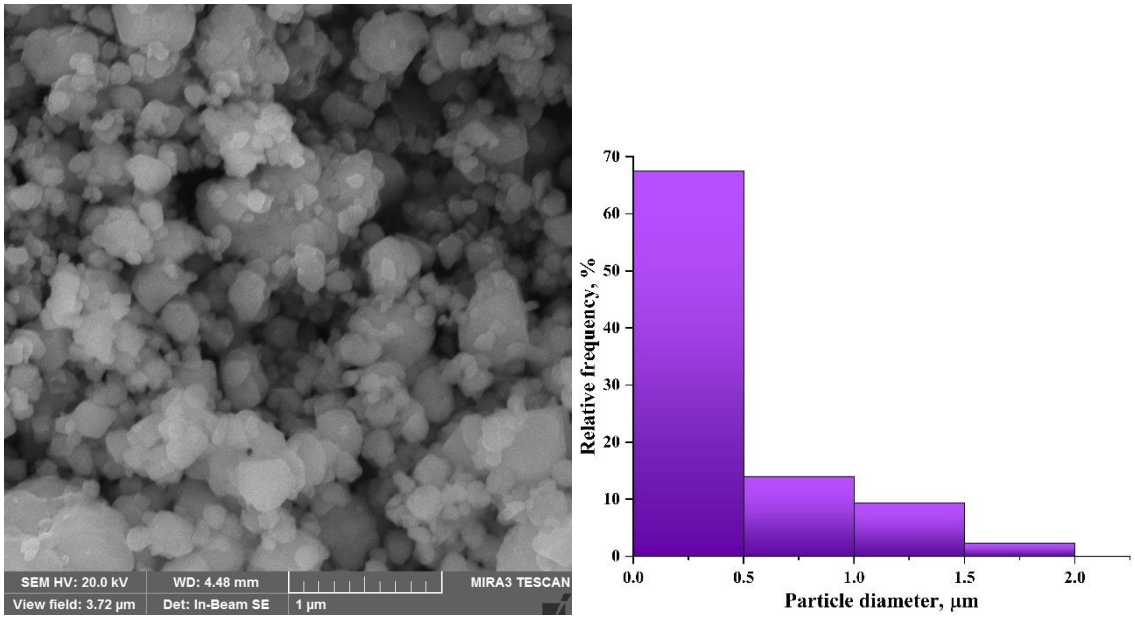

Figure 4.10. FESEM image and size distribution of $BaZrO_3/Y_2O_3/SrTiO_3$ nanoparticles

A more detailed examination of the relative frequency data confirms that the particle population is strongly concentrated within the submicron regime. Approximately 67% of all detected agglomerates fall below 0.5 μm, highlighting the effectiveness of the ball-milling process in reducing particle size and promoting fragmentation. Within this range, nearly 49% of particles are smaller than 0.2 μm, indicating that a substantial fraction of the material consists of ultrafine particles. This high proportion of fine particles suggests that fracture and comminution mechanisms dominate during milling, leading to progressive breakdown of larger particles and the formation of new surfaces. Despite this strong refinement effect, the size distribution also retains a noticeable fraction of intermediate-sized agglomerates in the range of 0.5-1.0 μm, which collectively account for approximately 14% of the population. These features likely correspond to partially fragmented clusters that have not undergone complete disintegration, reflecting the dynamic balance between particle breakage and re-agglomeration processes during milling. In contrast, micron-scale agglomerates (>1 μm) represent a relatively small fraction of the total population (~19%), with only about 7% exceeding 1.5 μm. These larger structures are not primary particles but rather secondary agglomerates, formed through mechanisms such as cold welding, mechanical interlocking and repeated plastic deformation under high-energy impacts. During ball milling, particles are subjected to cyclic fracture and bonding events; while impact forces promote size reduction, they can simultaneously induce

localized adhesion between freshly created surfaces, leading to the formation of larger aggregates. The presence of a limited but distinct coarse tail in the distribution is therefore consistent with this competitive interplay between fragmentation and agglomeration.
The observed distribution suggests a hierarchical structure, in which fine primary particles or crystallites are loosely assembled into secondary agglomerates of varying size. Importantly, the relatively low fraction of large agglomerates indicates that these clusters are neither dominant nor structurally continuous, but rather exist as isolated entities within an otherwise fine particle system. Such a particle size distribution is characteristic of mechanically activated ceramic powders, where high-energy milling leads to crystallite refinement, increased defect density, and the formation of submicron aggregates, while preserving a limited population of larger clusters due to incomplete dispersion or localized re-bonding. This morphology is particularly advantageous for subsequent processing steps, as the high fraction of fine particles enhances specific surface area and reactivity, while the weakly bound nature of secondary agglomerates facilitates their breakdown during dispersion in liquid media or polymer matrices. The results confirm that ball milling produces a heterogeneous but predominantly fine-grained particle system, governed by a dynamic equilibrium between particle fracture and re-agglomeration, which ultimately defines the structural and functional behavior of the material.

4.2.2. XRD analysis of $BaZrO_3/Y_2O_3/SrTiO_3$ nanoparticles

The X-ray diffraction (XRD) patterns of the commercial $BaZrO_3$ powder and the mechanically activated $BaZrO_3$-Y_2O_3-$SrTiO_3$ system are presented in Figure 4.11. The diffraction data clearly demonstrate that the perovskite structure of $BaZrO_3$ remains preserved after ball milling at 300 rpm for 30 min, indicating that the applied mechanical activation does not induce phase decomposition. The main diffraction maxima corresponding to the (110), (111), (200), (211), (220) and (310) planes are observed at approximately $2\theta \approx 30°$, 37°, 43°, 54°, 63°, and 71° (Cu Kα radiation), which are characteristic of cubic $BaZrO_3$. These reflections are in excellent agreement with the standard reference pattern (PDF No. 06-0399, $a = 4.193$ Å, $V = 73.7$ Å^3). The retention of peak positions and relative intensities, together with the absence of additional dominant reflections, confirms that the crystal symmetry and phase composition of $BaZrO_3$ are largely maintained during milling.

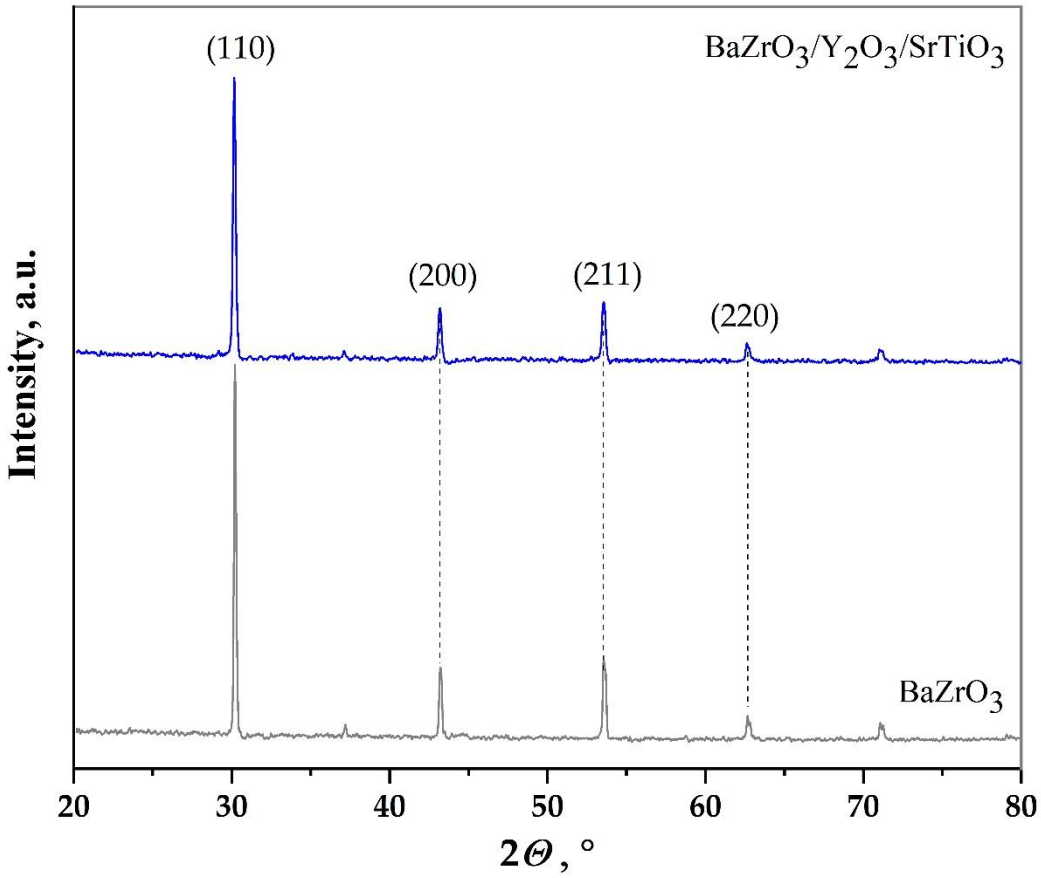

Figure 4.11. XRD pattern of $BaZrO_3$ and $BaZrO_3$-Y_2O_3-$SrTiO_3$ nanoparticles

Notably, diffraction peaks associated with crystalline Y_2O_3 (expected at $2\theta \approx 29°$, 33.8°, 48.5°, and 58°) are not observed within the detection limits of the instrument. This suggests that yttrium is not present as a separate, well-crystallized phase, but is instead at least partially incorporated into the perovskite lattice. A similar conclusion can be inferred for Sr and Ti species, whose contributions are either overlapped with the dominant $BaZrO_3$ reflections or distributed within the lattice [219]. Consequently, the material can be described as a compositionally modified perovskite system, approximating a (Ba,Sr)(Zr,Ti,Y)O_3-type structure, although not necessarily representing a fully equilibrated solid solution. From a crystallographic standpoint, such substitution is feasible due to the comparable ionic radii of the involved cations. Sr^{2+} (1.44 Å, CN = 12) can substitute for Ba^{2+} (1.61 Å, CN = 12) at the A-site, while Ti^{4+} (0.605 Å, CN = 6) and Y^{3+} (0.9 Å, CN = 6) may occupy the B-site positions typically held by Zr^{4+} (0.72 Å, CN = 6) within the octahedral framework. However, the incorporation of aliovalent Y^{3+} ions requires charge compensation, which is most likely achieved through the formation of oxygen vacancies and lattice defects, leading to local structural distortions. Refinement of the lattice parameters was performed using multiple $BaZrO_3$ reflections, assuming cubic symmetry (space group *Pm*–3*m*). The refined unit cell parameter for the commercial powder was determined as a = 4.192(2) Å (V = 73.68(3) Å^3), while the milled sample exhibited a slightly increased value of a = 4.196(2) Å (V = 73.88(2) Å^3). This corresponds to a small but measurable lattice expansion ($\Delta a \approx 0.004$ Å, ~0.1%). The shift of the (110) reflection toward lower diffraction angles further supports this observation. The observed expansion reflects the competing effects of different cation substitutions. While Sr^{2+} substitution at the A-site and Ti^{4+} substitution at the B-site would be expected to induce

lattice contraction due to their smaller ionic radii, the incorporation of the larger Y^{3+} ions (0.9 Å) into Zr^{4+} sites (0.72 Å) leads to lattice expansion. The experimental results indicate that the expansive effect of Y^{3+} substitution dominates, resulting in a net increase in unit cell volume. This behavior is consistent with partial substitution accompanied by defect formation, rather than uniform and complete solid-solution formation. While the data strongly suggest incorporation of Y^{3+} into the perovskite lattice, the presence of minor segregated or poorly crystalline phases cannot be entirely ruled out.

The average crystallite size was estimated using the Scherrer equation. The calculation was performed using multiple well-resolved $BaZrO_3$ reflections to ensure statistical reliability. The commercial $BaZrO_3$ exhibited an average crystallite size of 78(3) nm, while the milled sample showed a reduced size of 69(2) nm, indicating that mechanical activation leads to moderate crystallite refinement. It should be emphasized that the crystallite size obtained from the Scherrer equation represents the size of coherent diffraction domains, and is influenced by both finite crystallite size and microstrain-induced peak broadening. Therefore, the observed reduction in crystallite size likely reflects a combination of domain refinement and defect-induced lattice distortion, rather than purely geometric size reduction.

XRD results demonstrate that ball milling induces defect-assisted structural modification within a stable perovskite framework, rather than phase transformation. The slight lattice expansion, peak broadening, and reduction in crystallite size collectively indicate partial cation substitution and increased defect density. These changes suggest the formation of a non-equilibrium**,** defect-rich perovskite structure, rather than a fully homogenized thermodynamic solid solution, highlighting the structural robustness and defect tolerance of $BaZrO_3$ under mechanical activation conditions.

4.2.3. SEM analysis of PEI-$BaZrO_3$/Y_2O_3/$SrTiO_3$ composites

Scanning electron microscopy (SEM) was employed to examine the surface morphology of the PEI-$BaZrO_3$/Y_2O_3/$SrTiO_3$ composite films in order to assess filler dispersion, interfacial compatibility, and overall microstructural uniformity after solution casting (Figure 4.12.). At 1 wt% loading (PEI-$BaZrO_3$/Y_2O_3/$SrTiO_3$(1wt%)), the composite exhibits a highly homogeneous microstructure, characterized by a uniform distribution of ceramic domains within the continuous PEI matrix. The filler-rich regions are spatially separated and well embedded, with no evidence of large-scale clustering, phase segregation, or formation of interconnected particle networks. The dispersed features are predominantly within the submicron range, which is consistent with the particle size distribution of the starting powder described in Section 4.2.1., indicating that the dispersion process preserves the refined morphology achieved by ball milling [220]. At 3 wt% loading, particles are much denser, with more agglomerates formed (Figure 4.13.).

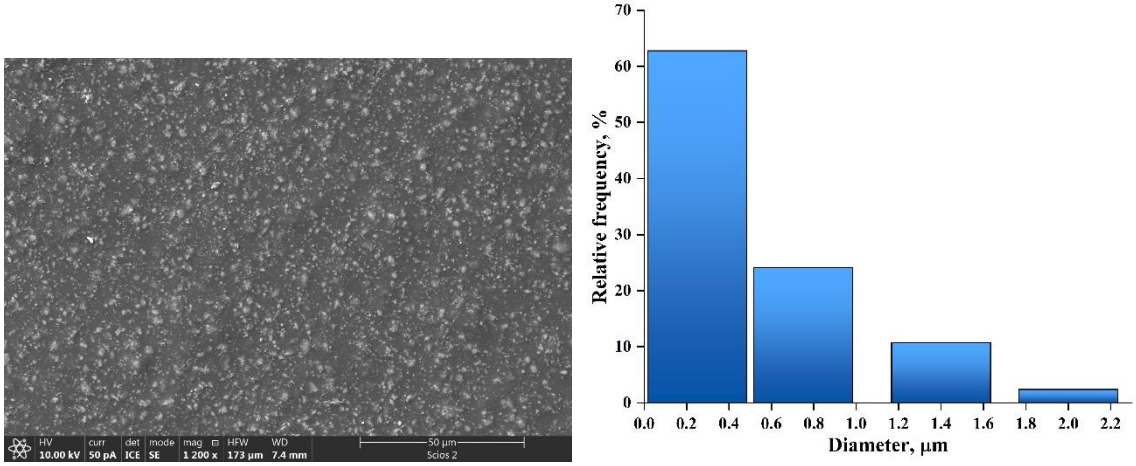

Figure 4.12. Surface SEM image and agglomerate size distribution in of PEI-$BaZrO_3/Y_2O_3/SrTiO_3$(1wt%)

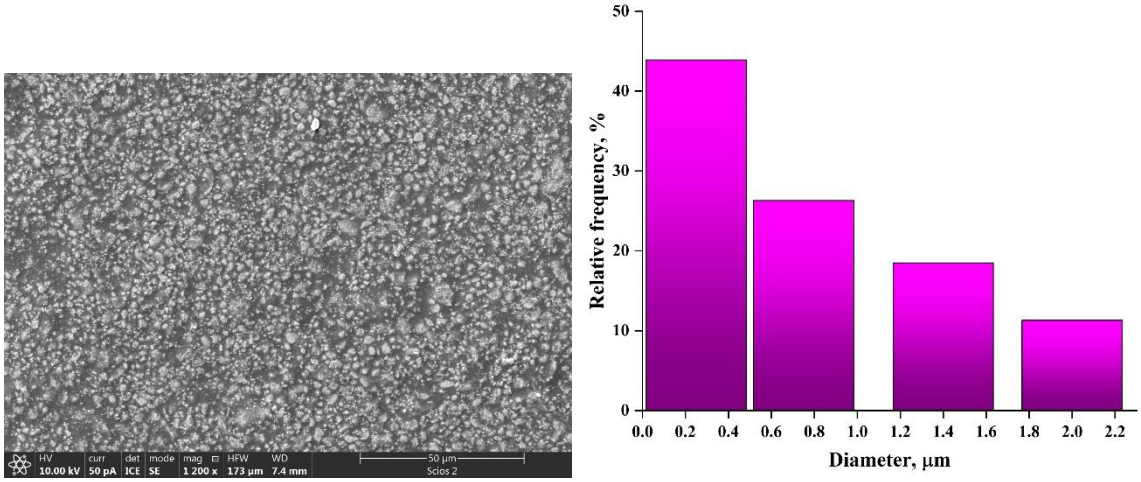

Figure 4.13. Surface SEM image and agglomerate size distribution in of PEI-$BaZrO_3/Y_2O_3/SrTiO_3$(3wt%)

Quantitative image analysis further confirms this observation (Figures 4.12. and 4.13.). The agglomerate size distribution is moderately right-skewed, with a median diameter of approximately 0.39 µm, reflecting a system dominated by fine particles with a limited contribution from larger agglomerates. The majority of particles (approximately 62.8%) fall within the 0.20-0.50 µm range, while an additional 14.4% are smaller than 0.20 µm. In contrast, only 13.1% of agglomerates exceed 1 µm, and a negligible fraction (2.4%) is larger than 2 µm. This distribution indicates that extensive agglomeration is effectively suppressed at low filler loading, resulting in a well-dispersed system with minimal structural heterogeneity.

Such a morphology suggests that the processing route, particularly solution mixing and casting, enables efficient particle wetting and stabilization within the polymer matrix, preventing extensive particle-particle interactions. The few larger agglomerates observed are most likely the result of localized clustering of fine particles, rather than systematic phase separation or processing-induced defects. The absence of voids, cracks or interfacial discontinuities indicates

good adhesion between the ceramic phase and the PEI matrix, which is essential for effective load transfer in composite systems.

In contrast, the composite containing 3 wt% $BaZrO_3/Y_2O_3/SrTiO_3$ (PEI-$BaZrO_3/Y_2O_3/SrTiO_3$(3wt%)) displays a broader and more pronounced right-skewed particle size distribution (Figure 4.13., indicating an increased contribution of larger agglomerates. Although submicron particles remain the dominant population, their relative fraction decreases compared to the 1 wt% system. Specifically, the proportion of particles in the 0.20-0.50 μm range drops to 38.8%, while the fractions in the 0.50-1.00 μm and 1.00-2.00 μm ranges increase to 26.3% and 18.5%, respectively. Notably, the population of agglomerates larger than 2 μm increases significantly to 11.3%, reflecting the formation of more pronounced secondary clusters. This shift is also reflected in the increase of the median agglomerate size to approximately 0.60 μm, as well as the extension of the upper quartile beyond 1 μm. These changes indicate that particle-particle interactions become more significant at higher filler loadings, promoting re-agglomeration through mechanisms such as van der Waals attraction, mechanical interlocking, and residual surface energy effects. Despite this increase in agglomerate size, the overall microstructure remains relatively uniform at the microscale. Importantly, no large continuous aggregates, percolated particle networks, or macroscopically segregated regions are observed. This suggests that agglomeration remains localized and discontinuous, rather than forming a continuous secondary phase that could compromise structural integrity. Furthermore, the absence of interfacial voids, cracks or particle pull-out features indicates that matrix-filler adhesion remains sufficient even at elevated filler content. The polymer matrix continues to effectively wet and anchor the ceramic particles, maintaining interfacial cohesion and preventing debonding under processing conditions.

The transition from the finely dispersed system at 1 wt% to the broader distribution at 3 wt% reflects a competition between dispersion forces and interparticle interactions. At lower concentrations, the polymer matrix effectively isolates individual particles, promoting uniform dispersion. At higher concentrations, increased particle proximity enhances the likelihood of contact and clustering, leading to partial agglomeration. However, since no percolation threshold or large-scale aggregation is reached, the composite retains its overall homogeneity.

4.2.3. FTIR analysis of PEI-$BaZrO_3/Y_2O_3/SrTiO_3$ composites

The FTIR spectrum of the PEI-$BaZrO_3/Y_2O_3/SrTiO_3$ composite (Figure 4.13.) was analyzed to evaluate potential chemical interactions between the polymer matrix and the incorporated $BaZrO_3/Y_2O_3/SrTiO_3$ ceramic phase. The spectrum retains all absorption bands of polyetherimide, indicating that the introduction of ceramic nanoparticles does not alter the chemical structure of the PEI backbone.

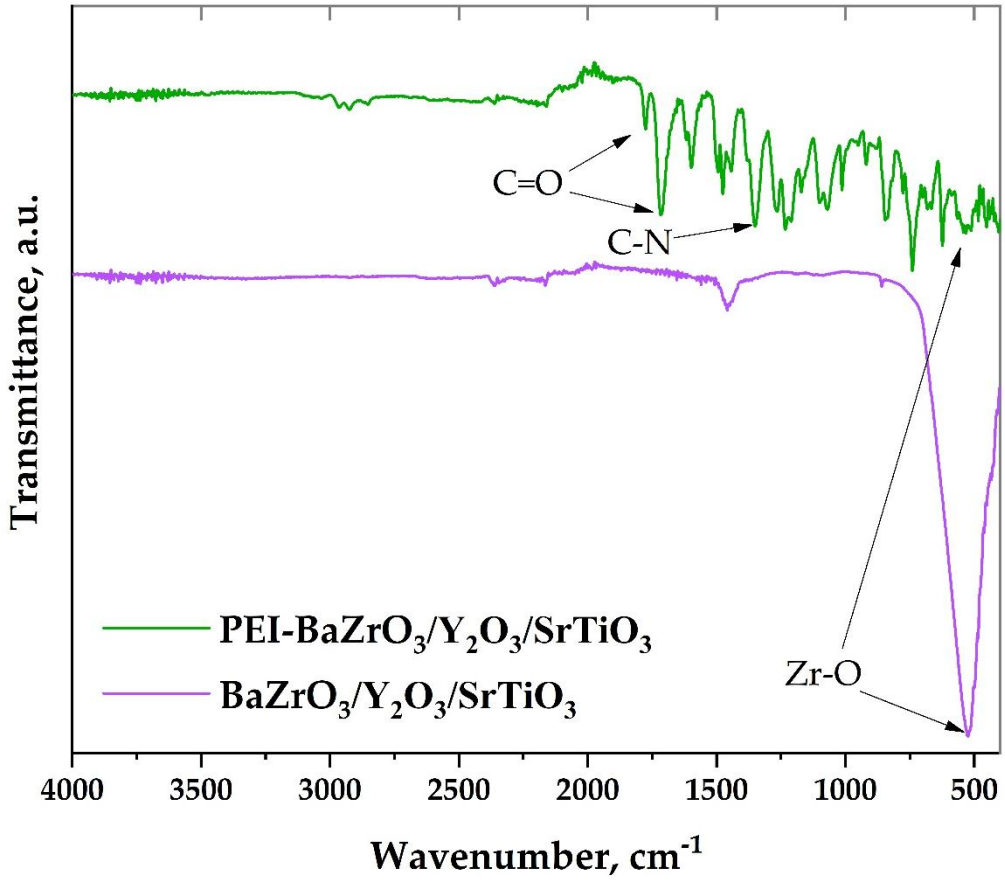

Figure 4.12. FTIR spectrums of nanoparticles and PEI-based composite

The most prominent features of PEI, namely the imide carbonyl stretching vibrations, are clearly preserved in the composite. The strong bands located at approximately 1779 cm^{-1} and 1715 cm^{-1}, corresponding to asymmetric and symmetric C=O stretching of the imide group, remain unchanged in both position and intensity. This confirms that the imide ring structure remains intact after composite processing. Similarly, other characteristic PEI bands, including aromatic C=C stretching (~1597 cm^{-1}), C–N stretching (~1350 cm^{-1}), and ether C–O–C vibrations (~1232 cm^{-1}), are clearly observed, further supporting the chemical stability of the polymer matrix [45].

In contrast to the unchanged polymer-related bands, additional absorption features appear in the composite spectrum, particularly in the low-wavenumber region, which can be attributed to the ceramic phase. These bands are absent in neat PEI and therefore serve as direct evidence of filler incorporation. Specifically, the band observed around 1450 cm^{-1} is associated with Ba–O vibrations, while the peak near 527 cm^{-1} corresponds to Zr–O and mixed metal–oxygen lattice vibrations characteristic of perovskite-type oxides. The presence of these bands confirms that the BZYS particles are successfully embedded within the polymer matrix and remain structurally intact after composite formation. No new absorption bands are detected, nor are there any significant shifts or broadening of the characteristic PEI peaks. This indicates that no chemical bonding or strong interfacial reactions occur between PEI and the ceramic phase. Instead, the interaction between the matrix and the filler is predominantly physical, likely governed by van der Waals forces and interfacial adhesion. This observation is consistent with the SEM analysis, which showed good dispersion and interfacial contact without evidence of chemical modification [221].

From a structure-property perspective, the absence of chemical interaction implies that the reinforcement mechanism in PEI-$BaZrO_3/Y_2O_3/SrTiO_3$ composites is primarily related to mechanical interlocking and interfacial constraint, rather than covalent bonding. At the same time, the preservation of the polymer's chemical structure ensures that its intrinsic thermal and chemical stability are maintained.

Table 4.8. Assignment of characteristic FTIR bands in PEI-$BaZrO_3$-Y_2O_3-$SrTiO_3$(3wt%) composite

Wavenumber (cm^{-1})	**Assignment**	**Origin**
~1779	Asymmetric C=O stretching (imide)	PEI
~1715	Symmetric C=O stretching (imide)	PEI
~1597	Aromatic C=C stretching	PEI
~1450	Ba–O vibration	BZYS
~1350	C–N stretching	PEI
~1232	C–O–C (ether) stretching	PEI
~527	Zr–O / mixed metal–O vibrations	$BaZrO_3/Y_2O_3/SrTiO_3$

4.2.4. Thermal analysis of PEI-$BaZrO_3/Y_2O_3/SrTiO_3$ composites

Differential scanning calorimetry (DSC) thermograms of neat PEI and PEI-$BaZrO_3/Y_2O_3/SrTiO_3$ composites are presented in Figure 4.13., and the extracted thermal parameters are summarized in Table 4.9. All samples exhibit a single, well-defined glass transition step during the first heating cycle, without the presence of melting or crystallization peaks within the investigated temperature range. This confirms that the polymer matrix remains predominantly amorphous, even after the incorporation of ceramic fillers. The glass transition temperature (T_g), determined from the midpoint of the heat flow inflection, increases systematically with filler addition. For neat PEI, T_g is observed at 202.0 °C, while the composites containing 1 wt% and 3 wt% $BaZrO_3/Y_2O_3/SrTiO_3$ show elevated values of 210.4 °C and 212.0 °C, respectively. This shift toward higher temperatures indicates a progressive restriction of polymer chain mobility induced by the presence of ceramic particles.

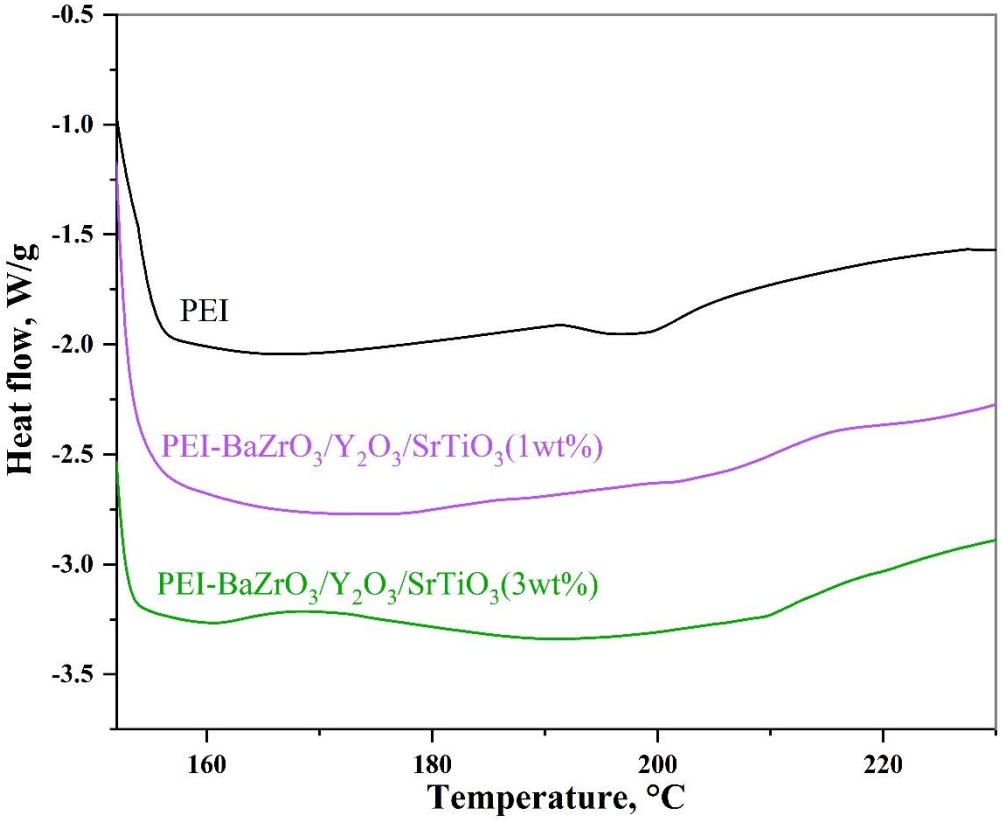

Figure 4.13. DSC analysis of PEI and PEI-$BaZrO_3/Y_2O_3/SrTiO_3$ nanocomposites

The relatively large increase in T_g at 1 wt% loading (+8.4 °C) suggests that even small amounts of $BaZrO_3/Y_2O_3/SrTiO_3$ nanoparticles significantly influence the segmental dynamics of the polymer. This behavior can be attributed to the formation of an interfacial immobilized layer, where polymer chains in close proximity to the particle surface experience reduced mobility due to physical interactions and spatial confinement. Such interphase regions effectively decrease the local free volume and hinder cooperative molecular motions, thereby increasing the thermal energy required for the glass transition. In contrast, further increasing the filler content from 1 wt% to 3 wt% results in only a modest additional increase in T_g (+1.6 °C). This behavior suggests the onset of a saturation effect, where the fraction of immobilized polymer chains does not increase proportionally with filler content. Two factors may contribute to this trend. First, at higher loadings, partial agglomeration of particles, observed in SEM analysis, reduces the effective interfacial surface area available for polymer-particle interaction. Second, the interphase regions may begin to overlap, limiting the extent to which additional filler can further constrain chain mobility. The absence of additional thermal transitions confirms that the ceramic particles do not induce crystallization in PEI, which is consistent with its inherently amorphous nature. Instead, the reinforcement mechanism is governed by physical confinement and interfacial effects, rather than nucleation-driven structural changes.

Table 4.9. Glass transition temperatures of PEI and PEI-$BaZrO_3/Y_2O_3/SrTiO_3$ composites

Sample	BZYS content (wt%)	Tg (°C)	ΔTg (°C)
PEI	0	202.0	–
PEI-$BaZrO_3/Y_2O_3/SrTiO_3$(1wt%)	1	210.4	+8.4
PEI-$BaZrO_3/Y_2O_3/SrTiO_3$(3wt%)	3	212.0	+10.0

Overall, DSC analysis demonstrates that the incorporation of BZYS nanoparticles leads to a significant enhancement in thermal resistance, primarily through interfacial confinement of polymer chains, with diminishing incremental effects at higher filler loadings due to partial interphase saturation and reduced effective dispersion [222].

4.2.5. Time-resolved laser-induced fluorescence

Time-resolved laser-induced fluorescence analysis shows that both neat PEI and PEI-$BaZrO_3/Y_2O_3/SrTiO_3$(3wt%) nanoparticle composites exhibit a broad emission band in the blue-green region, mainly between ~430 and 550 nm (Figure 4.14.). However, the PEI-$BaZrO_3/Y_2O_3/SrTiO_3$(3wt%) composite displays a noticeably stronger emission intensity than neat PEI, indicating that the incorporation of $BaZrO_3/Y_2O_3/SrTiO_3$ nanoparticles enhances the fluorescence response. The stronger emission intensity observed for the PEI-$BaZrO_3/Y_2O_3/SrTiO_3$ composite is expected, considering the intrinsically high luminescence activity of $BaZrO_3$-based perovskite oxides. $BaZrO_3$ can exhibit defect-related photoluminescence associated with oxygen vacancies, lattice distortions, and localized electronic states within the perovskite structure. The mechanically activated perovskite-based particles likely contain oxygen vacancies, lattice distortions, and surface defect states, all of which can participate in excitation trapping and delayed radiative emission.

(a) PEI (b) PEI-$BaZrO_3/Y_2O_3/SrTiO_3$(3wt%)

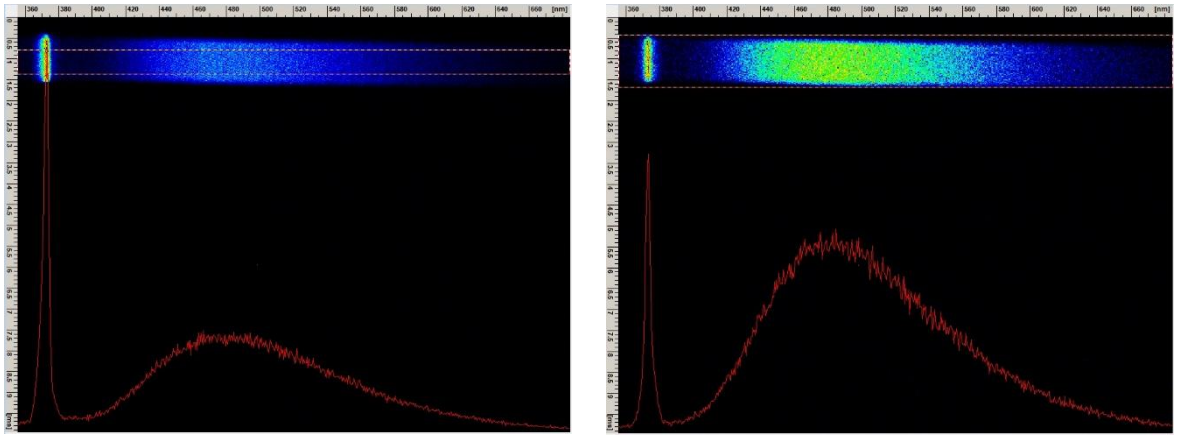

Figure 4.14. Streak images of (a) PEI and (b) PEI-$BaZrO_3/Y_2O_3/SrTiO_3$(3wt%) fluorescence

4.2.6. Cytotoxicity evaluation of PEI-$BaZrO_3/Y_2O_3/SrTiO_3$ composites

The cytotoxicity of the PEI-$BaZrO_3/Y_2O_3/SrTiO_3$ composite was assessed using an indirect extract assay (ISO 10993-5) on L929 fibroblasts, and the results indicate a concentration-

dependent biological response governed by the amount of leachable species present in the conditioned medium (Figures 4.15.-4.17.). Overall, the composites exhibit acceptable biocompatibility upon dilution, while the undiluted extract represents a more demanding exposure condition. At 100% extract, a reduction in cell viability is observed for the $BaZrO_3$-containing sample compared to neat PEI, indicating that the highest concentration of extractable species can transiently affect cell metabolic activity. However, upon dilution (e.g., 50% and 25%), cell viability increases markedly, approaching or exceeding the commonly accepted cytocompatibility threshold (≥70%), which confirms that the material does not induce persistent or severe cytotoxic effects under physiologically relevant exposure conditions. Quantitative results show that neat PEI maintains high cell viability across all conditions (~83–89%), confirming its baseline cytocompatibility (Figure 4.15.). The composite exhibits a more pronounced decrease at 100% extract (~46% viability), corresponding to moderate cytotoxicity (index 2). However, this effect is not sustained: at 50% extract, viability increases to ~71%, and at 25% it reaches ~90%, both corresponding to non-cytotoxic behavior (index 0). This rapid recovery strongly suggests that the biological response is governed by dose-dependent exposure, rather than permanent material-induced damage.

This behavior can be rationalized by considering both material chemistry and processing-related factors. From a chemical standpoint, $BaZrO_3$ is widely regarded as a bioinert ceramic, and therefore the observed effects are unlikely to arise from intrinsic toxicity of the oxide itself. Instead, the initial reduction in viability at high extract concentration is more plausibly associated with residual low-molecular-weight species, such as traces of solvent, unreacted processing components or minor ionic species released from the composite surface [223]. These species are readily diluted in the surrounding medium, which explains the rapid recovery of cell viability with decreasing extract concentration. However, the absence of sustained cytotoxic effects upon dilution indicates that the PEI-$BaZrO_3$/Y_2O_3/$SrTiO_3$ system demonstrates good cytocompatibility under realistic conditions, particularly when considering that in practical applications, direct exposure to undiluted extract is unlikely. Furthermore, the results are consistent with literature reports describing $BaZrO_3$-based materials as suitable for biomedical applications due to their chemical stability and low biological reactivity.

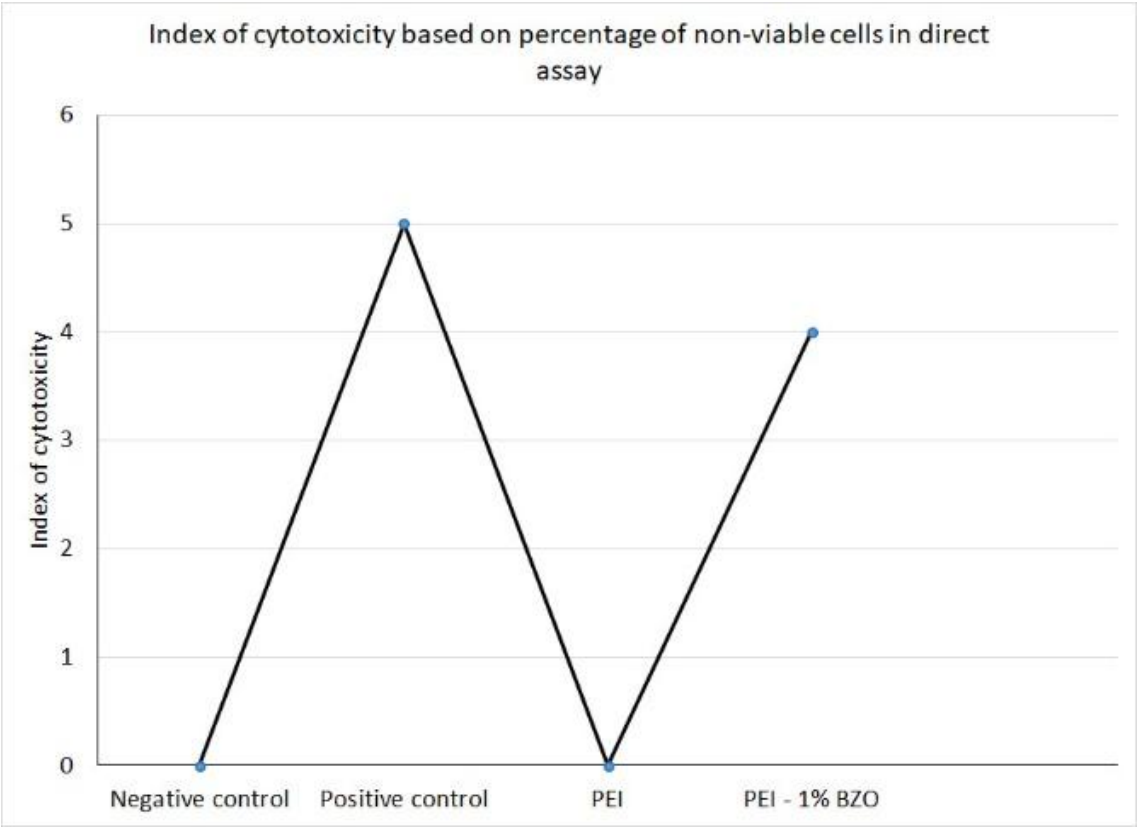

Figure 4.15. Cytotoxic effect of PEI and PEI-$BaZrO_3$/Y_2O_3/$SrTiO_3$(1wt%) on L929 cells upon the direct contact – quantitative assessment of the cytotoxic effect calculated by measuring the percentage of non-viable, based on which the indexes of cytotoxicity were assigned. Range of reference values: 0- absence of cytotoxicity (undetectable or basal cytotoxicity which is detected in the negative control); 1- discrete cytotoxicity (less than 20% of lysed (non-viable) cells); 2- mild cytotoxicity (20 - 40% of lysed (non-viable) cells); 3- moderate cytotoxicity (>40% - <60% of lysed (non-viable) cells); 4- serious cytotoxicity (>60% - <80% of lysed (non-viable) cells); 5- pronounced cytotoxicity (>80% of lysed (non-viable) cells).

From a structure-property-biological perspective, the findings highlight the importance of microstructural homogeneity and processing control. While the mechanical properties benefit from increased filler content and localized reinforcement, excessive or non-uniform filler accumulation may influence surface-mediated biological interactions. Therefore, ensuring uniform dispersion and minimizing sedimentation effects are essential not only for mechanical performance but also for achieving consistent biological behavior [224].

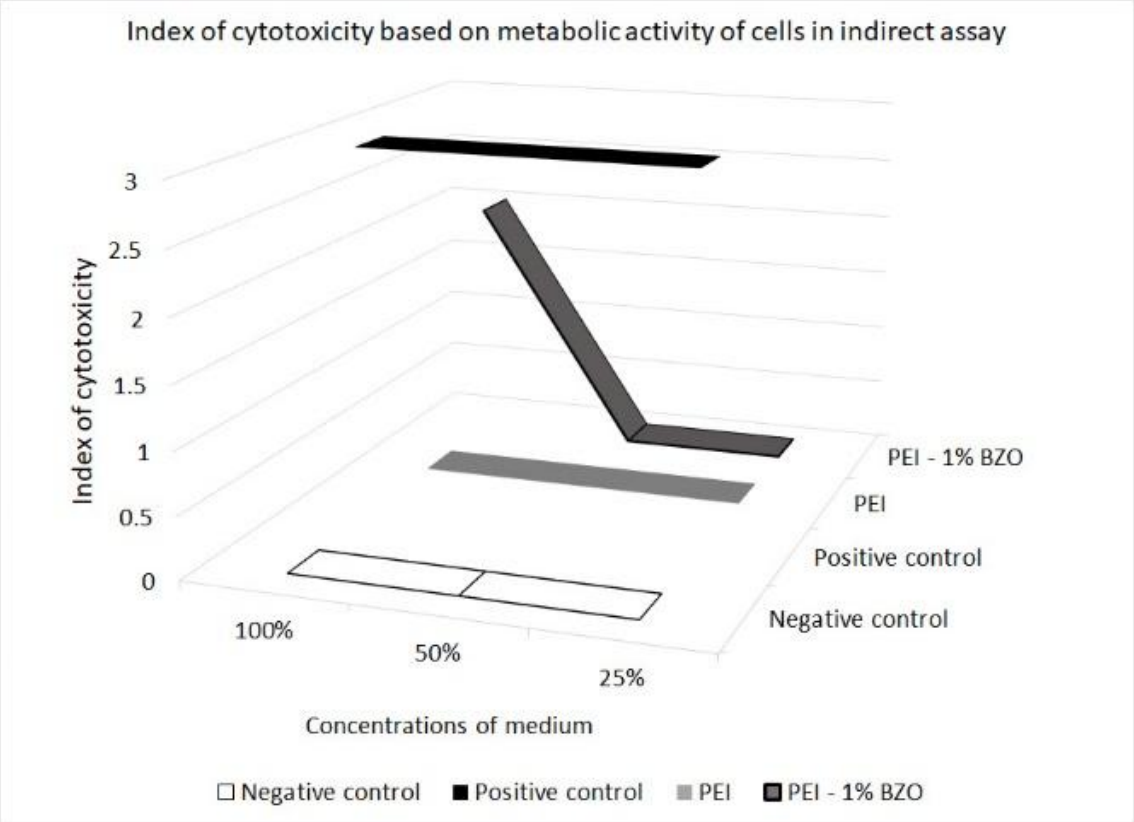

Figure 4.16. Cytotoxic effect of media conditioned with PEI and PEI-$BaZrO_3/Y_2O_3/SrTiO_3$(1wt%) on L929 cells based on metabolic activity of cells in an indirect assay (MTT). A) Cell viability is represented as a percentage of the absorbance value of the negative control culture, which was arbitrarily assigned a viability value of 100%. Results are presented as mean ± SD of three independent experiments and statistical significance was determined using the Student t-test. B) Index of cytotoxicity was defined according to reference range: 0 - absence of cytotoxicity (0-30% decrease in viability compared to control (100%)); 1 - discrete cytotoxicity (30%-50% decrease in viability compared to control); 2 - moderate cytotoxicity 50%-75% decrease in viability compared to control); 3 - pronounced cytotoxicity (75%-100% decrease in viability compared to the control).

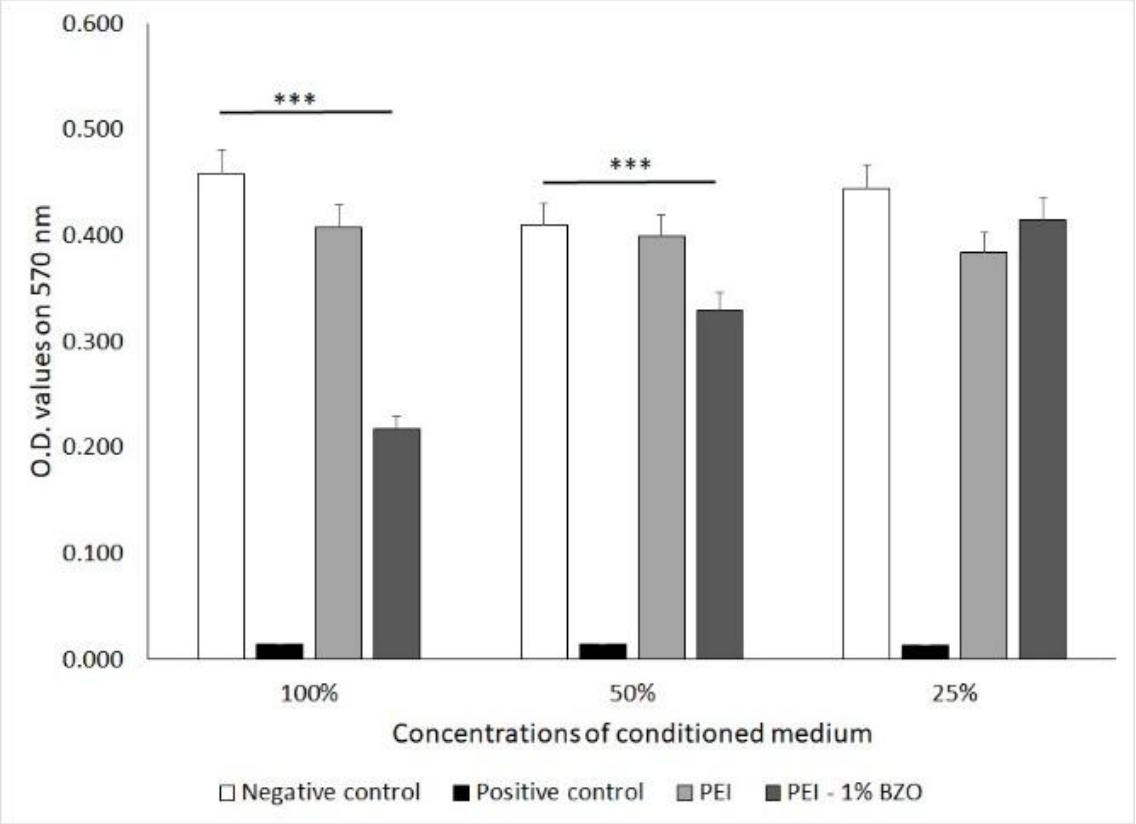

Figure 4.17. Cytotoxic effect of media conditioned with PEI and PEI-$BaZrO_3/Y_2O_3/SrTiO_3$(1wt%) on L929 cells based on metabolic activity of cells in an indirect assay (MTT) presented as optical density (O.D.) values obtained on 570 nm. Data are presented as Mean±SD for hexaplicates of treated cells in the culture

Table 4.10. Cytotoxicity assesment

	Negative control		**Positive control**		**PEI**		**PEI-$BaZrO_3/Y_2O_3/SrTiO_3$(1wt%)**	
Treatment	Cell viability (%)	Index of cytotoxicity	Cell viability (%)	Index of cytotoxicity	Cell viability (%)	Index of cytotoxicity	Cell viability (%)	Index of cytotoxicity
100%	100	0	1	3	83.2	0	46.0	2
50 %	100	0	1	3	86.8	0	71.2	0
25 %	100	0	2	3	88.6	0	90.3	0

*Viability of cells upon the treatment with PEI and PEI – 1% BZO conditioned media on L929 cells based on metabolic activity of cells in an indirect assay (MTT). Percentages of cell viability were calculated using the average values of obtained optical densities at 570 nm of different dilutions of conditioned media and negative control, each in hexaplicates. Index of cytotoxicity was defined according to reference range: 0 - absence of cytotoxicity (0-30% decrease in viability compared to control (100%)); 1 - discrete cytotoxicity (30%-50% decrease in viability compared to control); 2 - moderate cytotoxicity 50%-75% decrease in viability compared to control); 3 - pronounced cytotoxicity (75%-100% decrease in viability compared to the control) [225].

Morphological observations further support the conclusion that no severe cytotoxic mechanisms are activated Figures 4.18.-4.20.). Cells exposed to the composite extracts retain their characteristic fibroblastic morphology, with no evidence of widespread membrane disruption, apoptosis, or loss of adhesion comparable to positive controls. This indicates that

the material does not induce irreversible cellular damage, but rather transient metabolic suppression at high exposure levels.

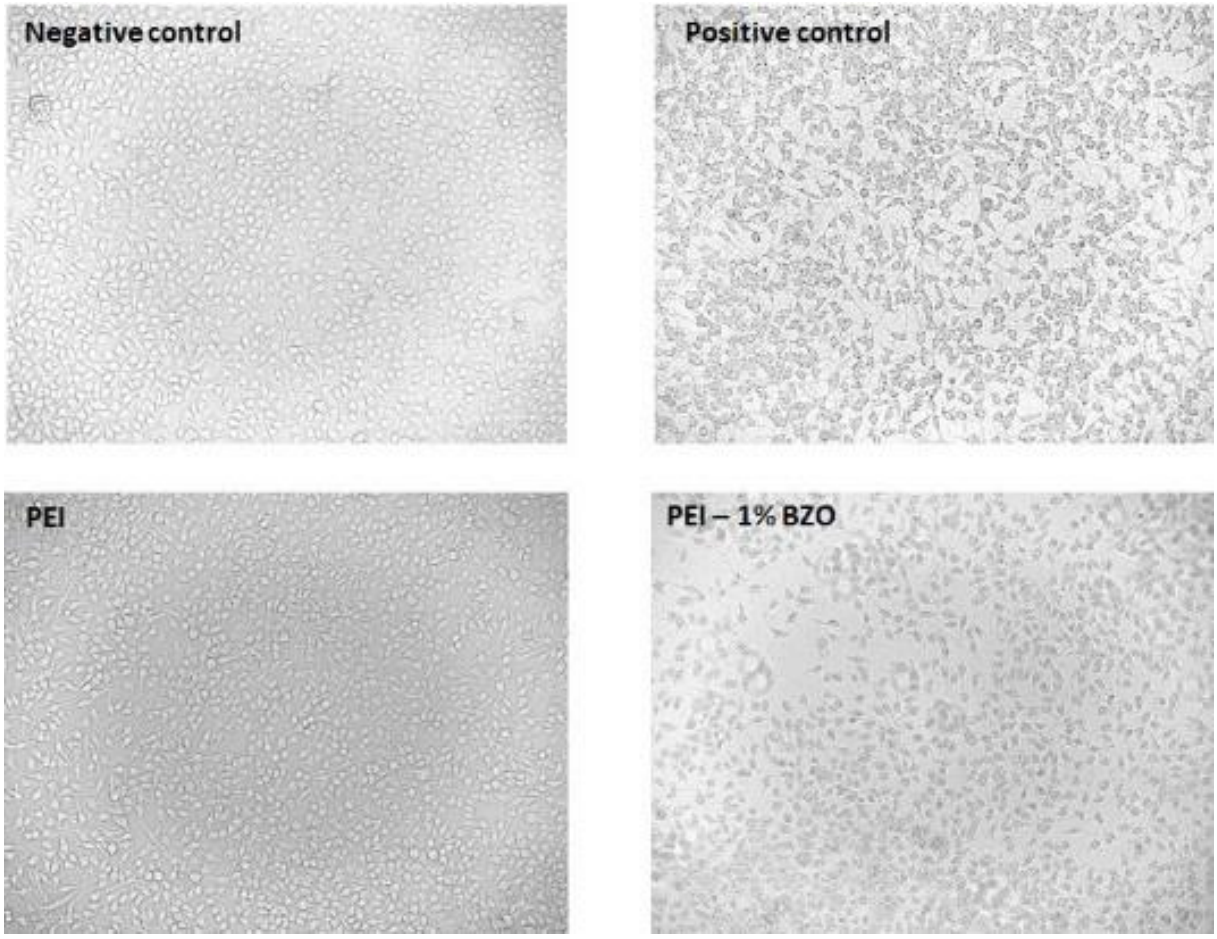

Figure 4.18. The effect of PEI and PEI-$BaZrO_3/Y_2O_3/SrTiO_3$(1wt%) on the morphology and phenotype of L929 cells. Morphological and intracellular changes of cells treated with the PEI and PEI-$BaZrO_3/Y_2O_3/SrTiO_3$(1wt%) for 24 h were determined without staining on live cells in the culture (Zoe Fluorescent Cell Imaging System [Bio-Rad, CA, United States], 200× magnification).

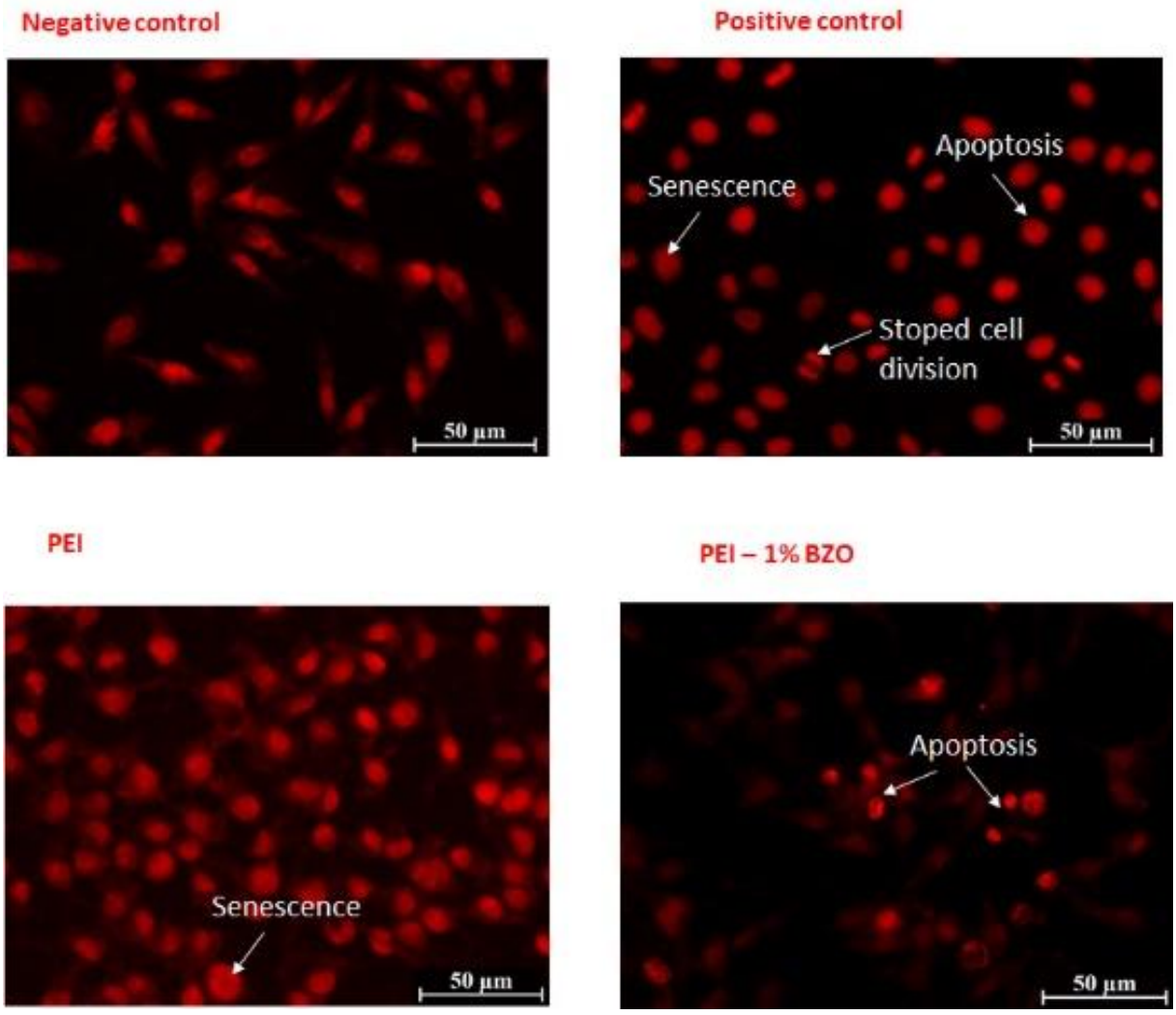

Figure 4.19. The effect of PEI and PEI-$BaZrO_3/Y_2O_3/SrTiO_3$(1wt%) on the morphology and phenotype of L929 cells. Morphological and intracellular changes of cells treated with PEI and PEI-$BaZrO_3/Y_2O_3/SrTiO_3$(1wt%) for 24 h were determined by propidium iodide staining and subsequent fluorescent microscopy (Axio Imager, Carl Zeiss microscope, 400× magnification) (apoptotic nuclei and stopped cell division are indicated by white arrows on positive controls). Representative micrographs are shown.

In summary, PEI-$BaZrO_3/Y_2O_3/SrTiO_3$ composites exhibit a dose-dependent cytotoxicity response, with reduced viability only at the highest extract concentration and excellent recovery upon dilution. The results confirm that the material is cytocompatible under standard conditions, while also emphasizing that local variations in filler distribution can influence the biological response and should be carefully controlled in future studies.

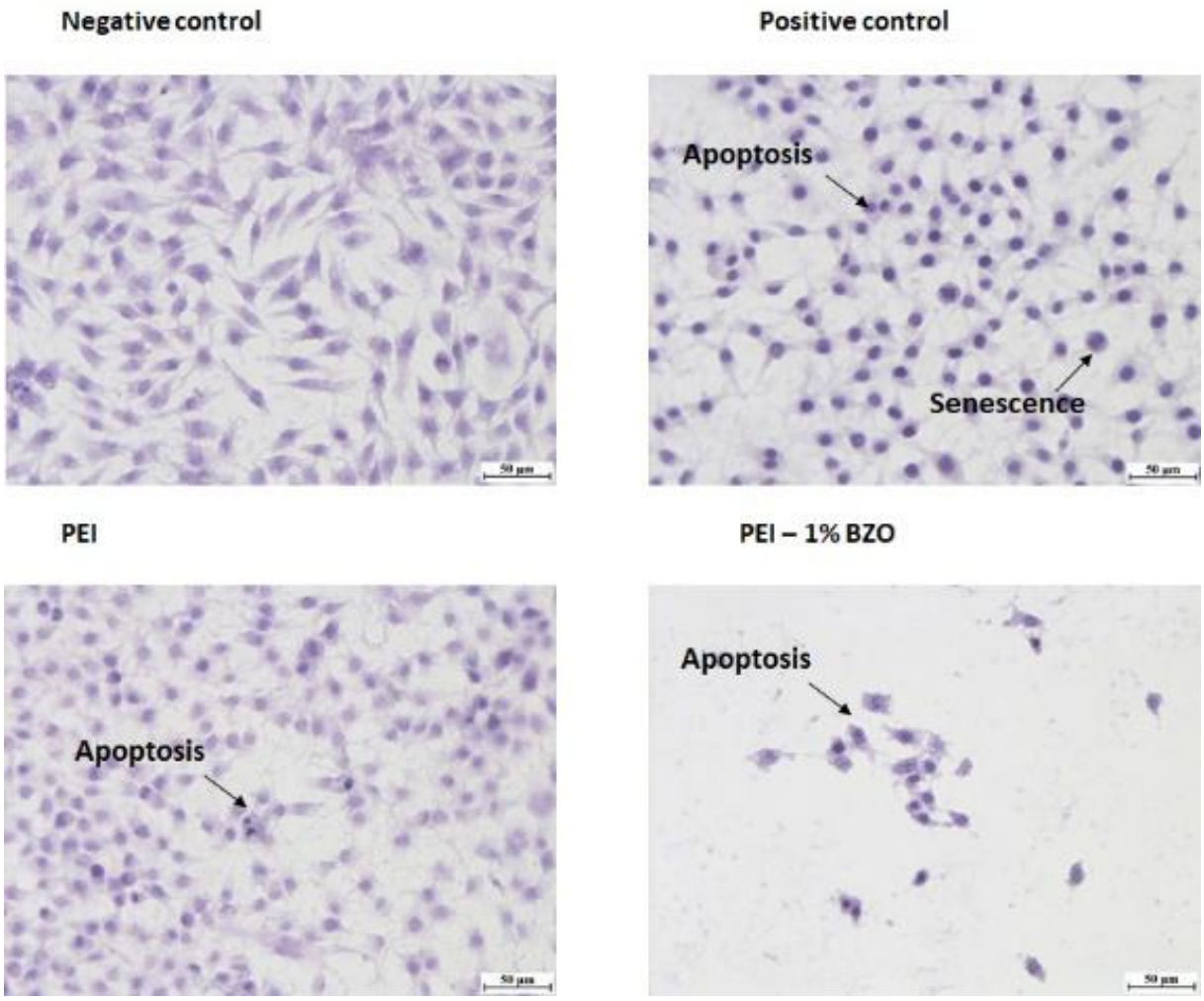

Figure 4.20. The effect of PEI and PEI-$BaZrO_3/Y_2O_3/SrTiO_3$(1wt%) on the morphology and phenotype of L929 cells.

Cells were cultivated on cover slips until they reached the confluency, fixed in 4% paraformaldehyde and stained with Mayer's Hematoxylin followed by the analyses under the light microscope (Axio Imager, Carl Zeiss, 200x magnification) (apoptotic nuclei are indicated by white arrows on positive controls).
In summary, the PEI-$BaZrO_3/Y_2O_3/SrTiO_3$ composites exhibit a dose-dependent cytotoxicity response, with reduced viability only at the highest extract concentration and excellent recovery upon dilution. The results confirm that the material is cytocompatible under standard conditions, while also emphasizing that local variations in filler distribution can influence the biological response and should be carefully controlled in future studies.

4.2.7. Microhardness analysis of PEI-$BaZrO_3/Y_2O_3/SrTiO_3$ composites

Microhardness results (Figure 4.21.) clearly demonstrate a substantial strengthening effect induced by the incorporation of $BaZrO_3/Y_2O_3/SrTiO_3$ particles into the PEI matrix. A systematic increase in hardness is observed with increasing filler content, highlighting the strong dependence of surface mechanical response on reinforcement loading. Compared to neat

PEI, the composite containing 1 wt% $BaZrO_3/Y_2O_3/SrTiO_3$ exhibits an increase in hardness of approximately 40%, while further addition to 3 wt% results in an enhancement of about 83%, indicating highly efficient reinforcement within a relatively low filler concentration range [226].

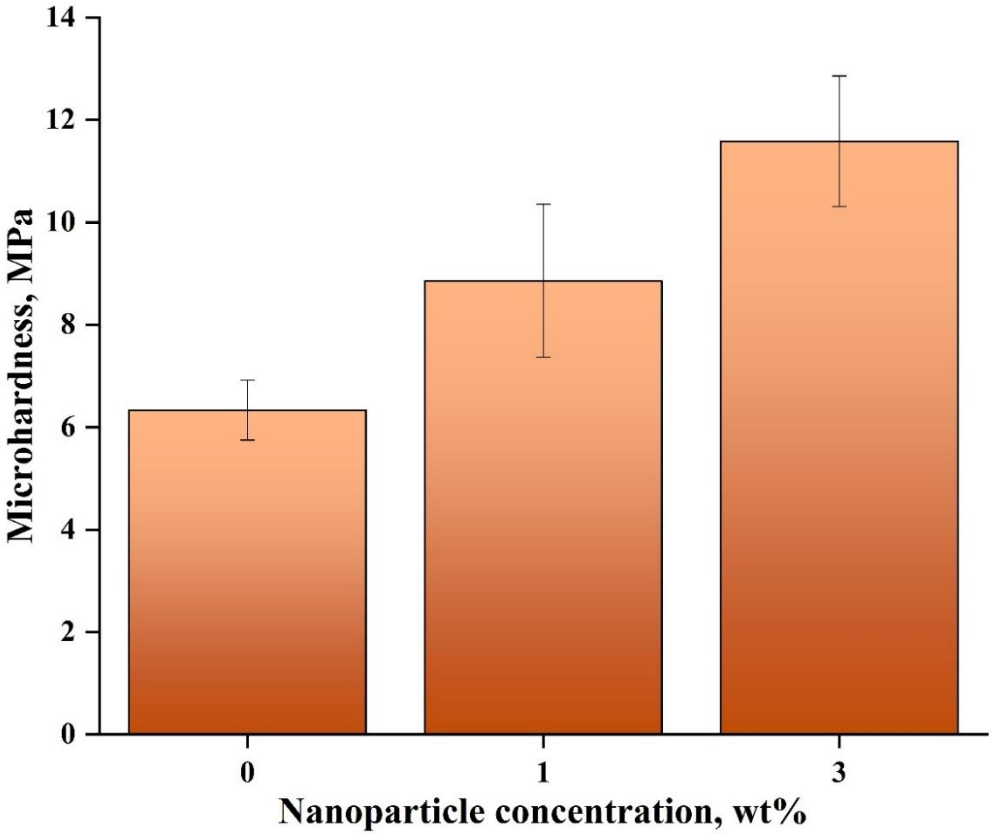

Figure 4.21. Microhardness of PEI and PEI-$BaZrO_3/Y_2O_3/SrTiO_3$

This pronounced improvement can be directly correlated with the microstructural characteristics revealed by SEM analysis. At 1 wt% loading, the particles are predominantly dispersed in the submicron range, forming well-separated domains within the polymer matrix. Such a morphology enables effective reinforcement through two primary mechanisms, localized restriction of polymer chain mobility in the vicinity of the filler surface and enhanced stress transfer across the particle-matrix interface. The relatively uniform dispersion ensures that these effects are distributed throughout the material, leading to a measurable increase in hardness. At 3 wt% loading, the highest hardness values are achieved, which is consistent with the increased number density of reinforcing domains. The SEM results indicate a broader particle size distribution at this loading, including a higher fraction of submicron-to-micron-scale agglomerates. Despite this, the dispersion remains sufficiently homogeneous, and no continuous particle networks or large-scale aggregates are formed. The presence of a greater number of rigid ceramic domains leads to increased local constraint of the polymer matrix, thereby enhancing resistance to indenter penetration. In this regime, load transfer is further improved by the closer proximity of particles, which facilitates stress sharing between adjacent reinforcement sites. Although some degree of agglomeration is observed at higher filler content, the fraction of large clusters remains limited. This indicates that the system does not exceed a critical threshold at which aggregation would introduce stress concentrations or structural defects. Instead, the microstructure maintains a balance between particle dispersion

and controlled agglomeration, which appears to be beneficial for mechanical performance. Despite the lack of chemical bonding, DSC results reveal a significant increase in glass transition temperature, particularly at low filler loading. This behavior indicates the formation of an interfacial immobilized layer, where polymer chains experience reduced mobility due to spatial confinement and interaction with the rigid particle surface. The pronounced Tg shift at 1 wt%, followed by a more modest increase at 3 wt%, suggests that the interfacial region becomes partially saturated at higher filler content, consistent with the onset of particle clustering observed in SEM. This interfacial constraint mechanism is directly reflected in the mechanical performance of the composites. Microhardness measurements show a strong and nearly linear increase with filler content. The enhancement arises from a combination of factors: the intrinsic stiffness of the ceramic phase, efficient stress transfer enabled by uniform dispersion, and restricted polymer chain mobility within the interphase. At higher loading, the increased number density of rigid domains further enhances resistance to deformation, while controlled agglomeration contributes to load sharing without introducing detrimental stress concentrations. Statistical analysis further supports the significance of these findings.

One-way ANOVA confirms that the differences in hardness among the investigated compositions are statistically significant ($p < 0.05$). Post hoc Tukey analysis reveals significant differences between neat PEI and both composite systems (PEI-$BaZrO_3$/Y_2O_3/$SrTiO_3$(1wt%) and PEI-$BaZrO_3$/Y_2O_3/$SrTiO_3$(3wt%)), confirming that even low levels of $BaZrO_3$/Y_2O_3/$SrTiO_3$ incorporation lead to measurable and reliable improvements in mechanical performance. The enhancement in microhardness can be attributed to a synergistic combination of factors, including increased filler content, effective dispersion of submicron particles, and the presence of controlled agglomerates that contribute to load-bearing capacity without compromising structural uniformity. These features collectively promote efficient stress transfer and restrict localized deformation, resulting in improved surface mechanical performance. From a broader perspective, although the present study focuses on a PEI matrix, the underlying reinforcement mechanism, based on ceramic reinforcements, interfacial constraint and defect-tolerant perovskite fillers, is not system-specific.

The combined results obtained from structural, morphological, thermal, mechanical, and optical analyses provide a consistent and complementary understanding of the behavior of PEI-$BaZrO_3$/Y_2O_3/$SrTiO_3$ composites across multiple length scales. At the powder level, ball milling produces a predominantly submicron particle system with a right-skewed size distribution, where fine particles dominate and only a limited fraction of larger agglomerates is present [227]. XRD analysis confirms that these particles retain the cubic perovskite $BaZrO_3$ structure, while undergoing slight lattice expansion and crystallite refinement due to partial cation substitution and defect formation. This results in a defect-modified, structurally stable ceramic phase, suitable for reinforcement purposes. When incorporated into the PEI matrix, SEM analysis shows that this powder morphology translates into a well-dispersed composite microstructure, particularly at low filler loading. At 1 wt% $BaZrO_3$/Y_2O_3/$SrTiO_3$ particles remain predominantly in the submicron range and are uniformly distributed within the polymer, ensuring effective stress transfer and minimal structural heterogeneity. Increasing the loading to 3 wt% leads to a broader particle size distribution and a higher fraction of micron-scale agglomerates, reflecting enhanced particle-particle interactions. However, the absence of continuous aggregates or phase-separated domains indicates that dispersion remains sufficiently homogeneous, with agglomeration confined to localized regions. These results demonstrate that the reinforcement of PEI by $BaZrO_3$/Y_2O_3/$SrTiO_3$ particles is governed by a multiscale synergistic mechanism. Overall, the PEI-$BaZrO_3$/Y_2O_3/$SrTiO_3$ composites exhibit a well-balanced combination of properties, where controlled dispersion, defect-engineered fillers and interfacial confinement act together to enhance composite performance. This makes the material particularly promising for applications requiring a combination of mechanical

robustness, thermal stability and tailored optical properties, such as advanced coatings, structural components and functional polymer-based systems.

4.3. Comparison of PEI-ZrO_2 and PEI-$BaZrO_3/Y_2O_3/SrTiO_3$ composites

A comparison between PEI composites reinforced with ZrO_2 nanofibers and those containing $BaZrO_3/Y_2O_3/SrTiO_3$ particles reveals important differences in reinforcement mechanisms, interfacial behavior, and resulting properties. Table 4.11. summarized the main differences between two types of novel composites presented in this dissertation.

From a morphological analysis, the most evident distinction arises from filler geometry. ZrO_2 is introduced in the form of high-aspect-ratio nanofibers, whereas $BaZrO_3/Y_2O_3/SrTiO_3$ is present as submicron, irregularly shaped particles or agglomerates. As a result, PEI–ZrO_2 composites exhibit a more anisotropic reinforcing architecture, where fibers can form a quasi-continuous load-bearing network even at relatively low concentrations. In contrast, PEI-$BaZrO_3/Y_2O_3/SrTiO_3$ composites rely on particle-based reinforcement, where stress transfer occurs through discrete filler-matrix interfaces and localized interphase regions. This difference in morphology directly influences the mechanical response. The PEI-ZrO_2 composites show extremely pronounced increases in hardness and modulus, driven by efficient load transfer along the fiber length and the ability of fibers to bridge deformation zones. On the other hand, PEI-$BaZrO_3/Y_2O_3/SrTiO_3$ composites also exhibit significant strengthening, but the mechanism is more dependent on particle dispersion, interfacial constraint, and filler concentration. While $BaZrO_3/Y_2O_3/SrTiO_3$ particles increase hardness through local stiffening and chain restriction, they do not provide the same level of stress redistribution as fibrous reinforcements.

From a thermal perspective, both composite systems show an increase in glass transition temperature (T_g), indicating restricted polymer chain mobility. However, the magnitude and origin of this effect differ slightly. In PEI-ZrO_2 composites, the high surface area and extended geometry of nanofibers promote a more continuous interfacial region, potentially leading to stronger confinement effects. In PEI-$BaZrO_3/Y_2O_3/SrTiO_3$ composites, the Tg increase is significant at low loading but tends to saturate at higher concentrations, reflecting the limited effective interfacial area due to partial agglomeration. This highlights the importance of filler dispersion and accessible surface area, rather than simply filler content.

Structurally, the fillers themselves differ in complexity. ZrO_2 is a relatively simple oxide system, whereas $BaZrO_3/Y_2O_3/SrTiO_3$ represents a multicomponent, defect-engineered perovskite. XRD analysis of $BaZrO_3/Y_2O_3/SrTiO_3$ indicates partial cation substitution and lattice distortion, resulting in a defect-rich structure that may influence interfacial interactions and surface energy. While this does not lead to chemical bonding (as confirmed by FTIR), it may contribute to improved compatibility and interaction at the polymer-filler interface compared to single-component oxides [228,229]. Finally, from a processing and dispersion perspective, the two systems exhibit different challenges. ZrO_2 nanofibers, while highly effective mechanically, may be more difficult to disperse uniformly due to entanglement and alignment tendencies. In contrast, $BaZrO_3/Y_2O_3/SrTiO_3$ particles, although prone to partial agglomeration at higher loadings, can be more easily dispersed at low concentrations and offer greater flexibility in tuning composite composition.

Table 4.11. Comparison of PEI-ZrO_2 and PEI-$BaZrO_3/Y_2O_3/SrTiO_3$ composites

Feature	PEI-ZrO_2 composites	PEI-$BaZrO_3/Y_2O_3/SrTiO_3$ composites
Filler type	ZrO_2 (single oxide)	$BaZrO_3/Y_2O_3/SrTiO_3$ (multicomponent perovskite)
Filler morphology	Nanofibers (high aspect ratio, anisotropic)	Submicron particles/agglomerates (quasi-spherical, isotropic)
Reinforcement mechanism	Fiber bridging, load transfer along fiber length, network formation	Particle reinforcement, interfacial constraint, localized stress transfer
Dispersion behavior	Potential fiber entanglement, but good distribution achievable	Uniform at low loading; partial agglomeration at higher loading
Microstructural evolution (↑ loading)	Increased fiber density, potential alignment effects	Broader size distribution, increased secondary agglomerates
Interfacial interaction	Predominantly physical; large interfacial area due to fiber geometry	Predominantly physical; interphase formation limited by agglomeration
Thermal behavior (Tg)	Slight increase due to strong interfacial confinement	Pronounced Tg increase at low loading; saturation at higher content
Crystallinity (polymer)	Remains amorphous	Remains amorphous
Mechanical improvement	Very high (strong increase in hardness/modulus)	Significant but lower than fiber system; increases with loading
Reinforcement efficiency	High at low loading due to fiber aspect ratio	Dependent on dispersion and particle distribution
Optical properties	Reduced transparency due to anisotropic scattering by fibers	Reduced transparency due to particle scattering and refractive mismatch
Scattering mechanism	Directional (fiber-induced) scattering	Diffuse scattering from size distribution and agglomerates
Structural complexity (filler)	Relatively simple oxide	Defect-engineered perovskite with cation substitution
Defect contribution	Limited (pure oxide)	Significant (lattice distortion, vacancies, substitution effects)
Processing sensitivity	Sensitive to fiber alignment/entanglement	Sensitive to agglomeration at higher loadings

5. CONCLUSIONS

This doctoral dissertation successfully demonstrates the potential of utilizing advanced ceramic nanofillers, specifically electrospun zirconia (ZrO_2) nanofibers and hybrid $BaZrO_3/Y_2O_3/SrTiO_3$ nanoparticles, as high-performance reinforcements for a polyetherimide (PEI) matrix. The study focused on understanding how reinforcement morphology (nanofibers vs. hierarchical particle agglomerates), filler content, dispersion quality, and interfacial interactions influence structural, thermal, mechanical, optical and biological properties.Through the integration of FESEM, XRD, FTIR, DSC, microindentation, nanoscratch testing, UV-Vis spectroscopy and cytotoxicity assays, this thesis establishes a comprehensive structure-property-processing relationship, demonstrating how processing conditions and reinforcement design govern composite performance. In light of the conducted research, the following conclusions are established:

- Two distinct reinforcement strategies were successfully implemented within the PEI matrix: high-aspect-ratio zirconia nanofibers and nanostructured $BaZrO_3/Y_2O_3/SrTiO_3$ hybrid ceramic agglomerates. This dual approach enabled a direct comparison between anisotropic fiber reinforcement and particle-based hierarchical reinforcement, providing a comprehensive framework for evaluating morphology-dependent strengthening mechanisms.
- Electrospinning followed by thermal treatment proved to be an effective method for producing continuous zirconia nanofibers, which were subsequently fragmented into whisker-like structures through ultrasonication. These high-aspect-ratio fragments retained sufficient geometry to enable efficient stress transfer, while their reduced length improved dispersion within the polymer matrix.
- Mechanochemical processing of $BaZrO_3$, Y_2O_3 and $SrTiO_3$ resulted in the formation of defect-modified, nanostructured ceramic agglomerates composed of nanoscale crystallites. Structural analysis confirmed preservation of the perovskite phase with slight lattice distortion, indicating partial cation substitution and defect formation rather than complete solid-solution equilibrium.
- In PEI-ZrO_2 composites, reinforcement efficiency was significantly higher, with hardness increases exceeding 140% at low filler loading. This demonstrates that high-aspect-ratio whisker-like structures provide more effective stress transfer and deformation resistance compared to particle-based systems, confirming the dominant role of reinforcement geometry.
- In PEI-$BaZrO_3/Y_2O_3/SrTiO_3$ composites, the most significant improvement in mechanical performance was achieved at 3 wt% loading, where microhardness increased by approximately 83%. This enhancement is attributed to a combination of uniform submicron particle dispersion, increased filler density, and interfacial constraint of polymer chain mobility.
- A direct correlation between microstructure and mechanical performance was established. The most effective reinforcement occurred in systems where fillers were well dispersed and acted as distributed load-bearing elements, whereas excessive agglomeration led to reduced efficiency due to local stress concentration and heterogeneity.
- It was established that the biological response of the composites is concentration-dependent. While moderate cytotoxicity was observed at full extract concentration, cell

viability recovered significantly upon dilution, indicating that the materials are cytocompatible under realistic conditions. The observed response is attributed to extractable species rather than intrinsic material toxicity.

- This thesis demonstrates that hybrid reinforcement strategies combining controlled morphology, defect-engineered ceramic systems, and optimized dispersion can significantly enhance the performance of polymer composites. The findings provide a foundation for the design of next-generation multifunctional materials for dental and biomedical applications.

References

[1] Avila JD, Bose S, Bandyopadhyay A. Additive manufacturing of titanium and titanium alloys for biomedical applications. Titanium in Medical and Dental Applications, Elsevier; 2018, p. 325–43. https://doi.org/10.1016/B978-0-12-812456-7.00015-9.

[2] Attar H, Ehtemam-Haghighi S, Soro N, et al. Additive manufacturing of low-cost porous titanium-based composites for biomedical applications: Advantages, challenges and opinion for future development. Journal of Alloys and Compounds 2020;827:154263. https://doi.org/10.1016/j.jallcom.2020.154263.

[3] Kerni L, Singh S, Patnaik A, et al. A review on natural fiber reinforced composites. Materials Today: Proceedings 2020;28:1616–21. https://doi.org/10.1016/j.matpr.2020.04.851.

[4] Yao J, Zhou Z, Zhou H. Highway Engineering Composite Material and Its Application. Singapore: Springer Singapore; 2019. https://doi.org/10.1007/978-981-13-6068-8.

[5] Sumithra G, Reddy RN, Dheeraj Kumar G, et al. Review on composite classification, manufacturing, and applications. Materials Today: Proceedings 2023. https://doi.org/10.1016/j.matpr.2023.04.637.

[6] Egbo MK. A fundamental review on composite materials and some of their applications in biomedical engineering. Journal of King Saud University - Engineering Sciences 2021;33:557–68. https://doi.org/10.1016/j.jksues.2020.07.007.

[7] Ngo T-D. Introduction to Composite Materials. Composite and Nanocomposite Materials - From Knowledge to Industrial Applications, IntechOpen; 2020. https://doi.org/10.5772/intechopen.91285.

[8] Sun J, Ye D, Zou J, et al. A review on additive manufacturing of ceramic matrix composites. Journal of Materials Science & Technology 2023;138:1–16. https://doi.org/10.1016/j.jmst.2022.06.039.

[9] Singh L, Singh B, Saxena KK. Manufacturing techniques for metal matrix composites (MMC): an overview. Advances in Materials and Processing Technologies 2020;6:441–57. https://doi.org/10.1080/2374068X.2020.1729603.

[10] Marghalani HY. Resin-Based Dental Composite Materials. Handbook of Bioceramics and Biocomposites, Cham: Springer International Publishing; 2016, p. 357–405. https://doi.org/10.1007/978-3-319-12460-5_22.

[11] Chen H, Wei S, Wang R, et al. Improving the Physical–Mechanical Property of Dental Composites by Grafting Methacrylate-Polyhedral Oligomeric Silsesquioxane onto a Filler Surface. ACS Biomaterials Science & Engineering 2021;7:1428–37. https://doi.org/10.1021/acsbiomaterials.1c00152.

[12] Yang Y, Xu Z, Guo Y, et al. Novel core–shell CHX/ACP nanoparticles effectively improve the mechanical, antibacterial and remineralized properties of the dental resin composite. Dental Materials 2021;37:636–47. https://doi.org/10.1016/j.dental.2021.01.007.

[13] Makvandi P, Gu JT, Zare EN, et al. Polymeric and inorganic nanoscopical antimicrobial fillers in dentistry. Acta Biomaterialia 2020;101:69–101. https://doi.org/10.1016/j.actbio.2019.09.025.

[14] Elfakhri F, Alkahtani R, Li C, et al. Influence of filler characteristics on the performance of dental composites: A comprehensive review. Ceramics International 2022;48:27280–94. https://doi.org/10.1016/j.ceramint.2022.06.314.

[15] J.F., McCabe WRW. Hardness of model dental composites - The effect of filler volume fraction and silanation. Journal of Materials Science: Materials in Medicine 1999;10:291–4. https://doi.org/10.1023/A:1008957513531.

[16] Ferracane JL. Resin composite—State of the art. Dental Materials 2011;27:29–38. https://doi.org/10.1016/j.dental.2010.10.020.
[17] Kretsis G. A review of the tensile, compressive, flexural and shear properties of hybrid fibre-reinforced plastics. Composites 1987;18:13–23. https://doi.org/10.1016/0010-4361(87)90003-6.
[18] Lindberg A, Peutzfeldt A, van Dijken JW V. Effect of power density of curing unit, exposure duration, and light guide distance on composite depth of cure. Clinical Oral Investigations 2005;9:71–6. https://doi.org/10.1007/s00784-005-0312-9.
[19] Ilie N, Bucuta S, Draenert M. Bulk-fill Resin-based Composites: An In Vitro Assessment of Their Mechanical Performance. Operative Dentistry 2013;38:618–25. https://doi.org/10.2341/12-395-L.
[20] Mitra SB, Wu D, Holmes BrainN. An application of nanotechnology in advanced dental materials. The Journal of the American Dental Association 2003;134:1382–90. https://doi.org/10.14219/jada.archive.2003.0054.
[21] Curtis AR, Palin WM, Fleming GJP, et al. The mechanical properties of nanofilled resin-based composites: The impact of dry and wet cyclic pre-loading on bi-axial flexure strength. Dental Materials 2009;25:188–97. https://doi.org/10.1016/j.dental.2008.06.003.
[22] Omar MF, Akil HM, Ahmad ZA. Particle size – Dependent on the static and dynamic compression properties of polypropylene/silica composites. Materials & Design 2013;45:539–47. https://doi.org/10.1016/j.matdes.2012.09.026.
[23] Cho K, Rajan G, Farrar P, et al. Dental resin composites: A review on materials to product realizations. Composites Part B: Engineering 2022;230:109495. https://doi.org/10.1016/j.compositesb.2021.109495.
[24] Zhou X, Huang X, Li M, et al. Development and status of resin composite as dental restorative materials. Journal of Applied Polymer Science 2019;136. https://doi.org/10.1002/app.48180.
[25] Jiangkongkho P, Arksornnukit M, Takahashi H. The synthesis, modification, and application of nanosilica in polymethyl methacrylate denture base. Dental Materials Journal 2018;37:582–91. https://doi.org/10.4012/dmj.2017-142.
[26] De Matteis V, Cascione M, Toma CC, et al. Silver Nanoparticles Addition in Poly(Methyl Methacrylate) Dental Matrix: Topographic and Antimycotic Studies. International Journal of Molecular Sciences 2019;20:4691. https://doi.org/10.3390/ijms20194691.
[27] Kostić M, Stanojević J, Tačić A, et al. Determination of residual monomer content in dental acrylic polymers and effect after tissues implantation. Biotechnology & Biotechnological Equipment 2020;34:254–63. https://doi.org/10.1080/13102818.2020.1736952.
[28] Nollenberger K, Albers J. Poly(meth)acrylate-based coatings. International Journal of Pharmaceutics 2013;457:461–9. https://doi.org/10.1016/j.ijpharm.2013.09.029.
[29] Keul C, Seidl J, Güth J-F, et al. Impact of fabrication procedures on residual monomer elution of conventional polymethyl methacrylate (PMMA)—a measurement approach by UV/Vis spectrophotometry. Clinical Oral Investigations 2020;24:4519–30. https://doi.org/10.1007/s00784-020-03317-1.
[30] Zafar MS. Prosthodontic Applications of Polymethyl Methacrylate (PMMA): An Update. Polymers 2020;12:2299. https://doi.org/10.3390/polym12102299.
[31] Pratte J. Polyetherimide Matrix Resins and Composites. Wiley Encyclopedia of Composites, Wiley; 2012, p. 1–8. https://doi.org/10.1002/9781118097298.weoc176.
[32] https://yifuhuiplastic.com/blog/what-is-pei-plastic/] (accessed 9.6.2025) n.d.

[33] https://www.plasticservice.com/industry-news/7087/unlocking-the-potential-of-polyetherimide--pei---properties-and-applications (accessed 9.6.2025) n.d.
[34] Johnson RO, Burlhis HS. Polyetherimide: A new high-performance thermoplastic resin. Journal of Polymer Science: Polymer Symposia 1983;70:129–43. https://doi.org/10.1002/polc.5070700111.
[35] Shanitha Salim, Gautam Ranjit. Recent advances in newer generation composites: An overview. World Journal of Advanced Research and Reviews 2022;14:100–3. https://doi.org/10.30574/wjarr.2022.14.2.0403.
[36] Jandt KD, Al-Jasser AMO, Al-Ateeq K, et al. Mechanical properties and radiopacity of experimental glass-silica-metal hybrid composites. Dental Materials 2002;18:429–35. https://doi.org/10.1016/S0109-5641(01)00064-1.
[37] Beyth N, Yudovin-Farber I, Bahir R, et al. Antibacterial activity of dental composites containing quaternary ammonium polyethylenimine nanoparticles against Streptococcus mutans. Biomaterials 2006;27:3995–4002. https://doi.org/10.1016/j.biomaterials.2006.03.003.
[38] Moraschini V, Fai CK, Alto RM, et al. Amalgam and resin composite longevity of posterior restorations: A systematic review and meta-analysis. Journal of Dentistry 2015;43:1043–50. https://doi.org/10.1016/j.jdent.2015.06.005.
[39] Kukulka EC, Sato TP, Archangelo KC, et al. Development of electrospun-based polyetherimide fibers and diameter analysis for potential use in dental materials. Brazilian Dental Science 2021;24:5. https://doi.org/10.14295/bds.2021.v24i2.2107.
[40] Khan AS, Azam MT, Khan M, et al. An update on glass fiber dental restorative composites: A systematic review. Materials Science and Engineering: C 2015;47:26–39. https://doi.org/10.1016/j.msec.2014.11.015.
[41] Thomason JL. The influence of fibre length, diameter and concentration on the impact performance of long glass-fibre reinforced polyamide 6,6. Composites Part A: Applied Science and Manufacturing 2009;40:114–24. https://doi.org/10.1016/j.compositesa.2008.10.013.
[42] Guarino V, Antonio Alvarez-Pérez M, editors. Current Advances in Oral and Craniofacial Tissue Engineering. Boca Raton : CRC Press, [2020]: CRC Press; 2020. https://doi.org/10.1201/9780429423055.
[43] Safwat EM, Khater AGA, Abd-Elsatar AG, et al. Glass fiber-reinforced composites in dentistry. Bulletin of the National Research Centre 2021;45:190. https://doi.org/10.1186/s42269-021-00650-7.
[44] Leprince J, Palin WM, Mullier T, et al. Investigating filler morphology and mechanical properties of new low-shrinkage resin composite types. Journal of Oral Rehabilitation 2010;37:364–76. https://doi.org/10.1111/j.1365-2842.2010.02066.x.
[45] Mali C, Maniyar K, Rupanar S, et al. An Analysis of Nanoparticles in Composite Materials. Journal of Mines, Metals and Fuels 2024:1215–23. https://doi.org/10.18311/jmmf/2024/45579.
[46] Saha R, Munshi MdH, Akter M, et al. Synthesis techniques, fundamental properties, and emerging applications of nanocomposites: A comprehensive review. SPE Polymers 2025;6. https://doi.org/10.1002/pls2.70004.
[47] Uddin MdN, Hossain MdT, Mahmud N, et al. Research and applications of nanoclays: A review. SPE Polymers 2024;5:507–35. https://doi.org/10.1002/pls2.10146.
[48] Okamoto M. Polymer Nanocomposites. Eng 2023;4:457–79. https://doi.org/10.3390/eng4010028.
[49] Camargo PHC, Satyanarayana KG, Wypych F. Nanocomposites: synthesis, structure, properties and new application opportunities. Materials Research 2009;12:1–39. https://doi.org/10.1590/S1516-14392009000100002.

[50] Lalire T, Longuet C, Taguet A. Electrical properties of graphene/multiphase polymer nanocomposites: A review. Carbon 2024;225:119055. https://doi.org/10.1016/j.carbon.2024.119055.
[51] Ayesha Khan, Sadia Iqbal, Mehrab Khan, et al. A Comprehensive Review on Polymer Nanocomposites; Classification, Properties and Potential Applications. JOURNAL OF NANOSCOPE (JN) 2023;4:45–74. https://doi.org/10.52700/jn.v4i1.88.
[52] Wang Y, Ye J, Li J, et al. Microstructure and properties of SrTiO3/ZrO2 ceramic composites prepared through pressureless sintering. Ceramics International 2024;50:1908–17. https://doi.org/10.1016/j.ceramint.2023.10.293.
[53] Pavanello L, Cortês IT, de Carvalho RDP, et al. Physicochemical and biological properties of dental materials and formulations with silica nanoparticles: A narrative review. Dental Materials 2024;40:1729–41. https://doi.org/10.1016/j.dental.2024.07.028.
[54] Chen H, Luo J, Yang J, et al. Synthesis of Pore-Size-Tunable Porous Silica Particles and Their Effects on Dental Resin Composites. Biomolecules 2023;13:1290. https://doi.org/10.3390/biom13091290.
[55] Nabhan A, Taha M, Ghazaly NM. Filler loading effect of Al2O3/TiO2 nanoparticles on physical and mechanical characteristics of dental base composite (PMMA). Polymer Testing 2023;117:107848. https://doi.org/10.1016/j.polymertesting.2022.107848.
[56] Azmy E, Al-Kholy MRZ, Fattouh M, et al. Impact of Nanoparticles Additions on the Strength of Dental Composite Resin. International Journal of Biomaterials 2022;2022:1–9. https://doi.org/10.1155/2022/1165431.
[57] Gad MM, Abualsaud R. Behavior of PMMA Denture Base Materials Containing Titanium Dioxide Nanoparticles: A Literature Review. International Journal of Biomaterials 2019;2019:1–14. https://doi.org/10.1155/2019/6190610.
[58] Wang J, Zhang L, Wang K. Bioactive ceramic-based materials: beneficial properties and potential applications in dental repair and regeneration. Regenerative Medicine 2024;19:257–78. https://doi.org/10.1080/17460751.2024.2343555.
[59] Fernandes JS, Gentile P, Pires RA, et al. Multifunctional bioactive glass and glass-ceramic biomaterials with antibacterial properties for repair and regeneration of bone tissue. Acta Biomaterialia 2017;59:2–11. https://doi.org/10.1016/j.actbio.2017.06.046.
[60] Workie AB, Shih S-Ju. A study of bioactive glass–ceramic's mechanical properties, apatite formation, and medical applications. RSC Advances 2022;12:23143–52. https://doi.org/10.1039/D2RA03235J.
[61] Dorozhkin S V. Bioceramics of calcium orthophosphates. Biomaterials 2010;31:1465–85. https://doi.org/10.1016/j.biomaterials.2009.11.050.
[62] Jeong J, Kim JH, Shim JH, et al. Bioactive calcium phosphate materials and applications in bone regeneration. Biomaterials Research 2019;23. https://doi.org/10.1186/s40824-018-0149-3.
[63] Karabela MM, Sideridou ID. Synthesis and study of properties of dental resin composites with different nanosilica particles size. Dental Materials 2011;27:825–35. https://doi.org/10.1016/j.dental.2011.04.008.
[64] SAGHIRI MA, ORANGI J, ASATOURIAN A, et al. Calcium silicate-based cements and functional impacts of various constituents. Dental Materials Journal 2017;36:8–18. https://doi.org/10.4012/dmj.2015-425.
[65] Cuylear DL, Elghazali NA, Kapila SD, et al. Calcium Phosphate Delivery Systems for Regeneration and Biomineralization of Mineralized Tissues of the Craniofacial Complex. Molecular Pharmaceutics 2023;20:810–28. https://doi.org/10.1021/acs.molpharmaceut.2c00652.

[66] Luo X, Barbieri D, Davison N, et al. Zinc in calcium phosphate mediates bone induction: In vitro and in vivo model. Acta Biomaterialia 2014;10:477–85. https://doi.org/10.1016/j.actbio.2013.10.011.
[67] Demirkiran H. Bioceramics for Osteogenesis, Molecular and Cellular Advances, 2012, p. 134–47. https://doi.org/10.1007/978-1-4614-4090-1_9.
[68] Chen Y, Liu Z, Jiang T, et al. Strontium-substituted biphasic calcium phosphate microspheres promoted degradation performance and enhanced bone regeneration. Journal of Biomedical Materials Research Part A 2020;108:895–905. https://doi.org/10.1002/jbm.a.36867.
[69] Dyer MS, Darling GR, Claridge JB, et al. Chemical Bonding and Atomic Structure in Y 2 O 3 :ZrO 2 -SrTiO 3 Layered Heterostructures. Angewandte Chemie 2012;124:3474–8. https://doi.org/10.1002/ange.201108068.
[70] Li Q-L, Jiang Y-Y, Wei Y-R, et al. The influence of yttria content on the microstructure, phase stability and mechanical properties of dental zirconia. Ceramics International 2022;48:5361–8. https://doi.org/10.1016/j.ceramint.2021.11.079.
[71] Gamoudi HA, Radojevic V, Stajcic A, et al. Microhardness Enhancement in Polymer Composites via BaZrO3-Based Ceramic Reinforcement. Applied Sciences 2026;16:2529. https://doi.org/10.3390/app16052529.
[72] Nayak AK, Sasmal A. Recent advance on fundamental properties and synthesis of barium zirconate for proton conducting ceramic fuel cell. Journal of Cleaner Production 2023;386:135827. https://doi.org/10.1016/j.jclepro.2022.135827.
[73] Kadhum RN, Hamad TI. Barium titanate synthesis, mechanism of action and its applications in dentistry: A literature review. Journal of Applied Biomaterials & Functional Materials 2025;23. https://doi.org/10.1177/22808000251375714.
[74] Sood A, Desseigne M, Dev A, et al. A Comprehensive Review on Barium Titanate Nanoparticles as a Persuasive Piezoelectric Material for Biomedical Applications: Prospects and Challenges. Small 2023;19. https://doi.org/10.1002/smll.202206401.
[75] Elhmali HT, Radojevic V, Stajcic A, et al. Denture base poly(methyl methacrylate) reinforced with <scp> SrTiO 3 </scp> / <scp> Y 2 O 3 </scp> : Structural, morphological and mechanical analysis. Polymer Composites 2025;46:8831–40. https://doi.org/10.1002/pc.29523.
[76] Ismael M. A review on graphitic carbon nitride (g-C3N4) based nanocomposites: Synthesis, categories, and their application in photocatalysis. Journal of Alloys and Compounds 2020;846:156446. https://doi.org/10.1016/j.jallcom.2020.156446.
[77] Rane AV, Kanny K, Abitha VK, et al. Methods for Synthesis of Nanoparticles and Fabrication of Nanocomposites. Synthesis of Inorganic Nanomaterials, Elsevier; 2018, p. 121–39. https://doi.org/10.1016/B978-0-08-101975-7.00005-1.
[78] Baig N, Kammakakam I, Falath W. Nanomaterials: a review of synthesis methods, properties, recent progress, and challenges. Materials Advances 2021;2:1821–71. https://doi.org/10.1039/D0MA00807A.
[79] Gutierrez-Sanchez CD, Téllez-Jurado L, Dorantes-Rosales HJ. Synthesis of zirconia nanoparticles by sol-gel. Influence of acidity-basicity on the stability transformation, particle, and crystallite size. Ceramics International 2024;50:20547–60. https://doi.org/10.1016/j.ceramint.2024.03.177.
[80] Bokov D, Turki Jalil A, Chupradit S, et al. Nanomaterial by Sol-Gel Method: Synthesis and Application. Advances in Materials Science and Engineering 2021;2021. https://doi.org/10.1155/2021/5102014.
[81] Yilmaz E, Soylak M. Functionalized nanomaterials for sample preparation methods. Handbook of Nanomaterials in Analytical Chemistry, Elsevier; 2020, p. 375–413. https://doi.org/10.1016/B978-0-12-816699-4.00015-3.

[82] Xu J, Jia J, Li B, et al. High-Temperature Mechanochemical Synthesis of Nano-ZrO2 for Enhanced Densification and Fracture Toughness in B4C Ceramics. Materials 2025;18:2332. https://doi.org/10.3390/ma18102332.
[83] Xiong Y, Du X, Xiang M, et al. Densification mechanism during reactive hot pressing of B4C-ZrO2 mixtures. Journal of the European Ceramic Society 2018;38:4167–72. https://doi.org/10.1016/j.jeurceramsoc.2018.05.016.
[84] Kim H-W, Koh Y-H, Kim H-E. Reaction sintering and mechanical properties of B 4 C with addition of ZrO 2. Journal of Materials Research 2000;15:2431–6. https://doi.org/10.1557/JMR.2000.0349.
[85] Fu S. Effects of fiber length and fiber orientation distributions on the tensile strength of short-fiber-reinforced polymers. Composites Science and Technology 1996;56:1179–90. https://doi.org/10.1016/S0266-3538(96)00072-3.
[86] Syed MR, Bano NZ, Ghafoor S, et al. Synthesis and characterization of bioactive glass fiber-based dental restorative composite. Ceramics International 2020;46:21623–31. https://doi.org/10.1016/j.ceramint.2020.05.268.
[87] Bor Z. Jang. Advanced Polymer Composites: Principles and Applications. Taylor & Francis, 1994; 1994.
[88] ISO 4049: Dentistry—Polymer-Based Restorative Materials n.d.
[89] Jiang S, Chen Y, Duan G, et al. Electrospun nanofiber reinforced composites: a review. Polymer Chemistry 2018;9:2685–720. https://doi.org/10.1039/C8PY00378E.
[90] Kumari N, Sareen S, Verma M, et al. Zirconia-based nanomaterials: recent developments in synthesis and applications. Nanoscale Advances 2022;4:4210–36. https://doi.org/10.1039/D2NA00367H.
[91] Bumajdad A, Nazeer AA, Al Sagheer F, et al. Controlled Synthesis of ZrO2 Nanoparticles with Tailored Size, Morphology and Crystal Phases via Organic/Inorganic Hybrid Films. Scientific Reports 2018;8:3695. https://doi.org/10.1038/s41598-018-22088-0.
[92] Isacfranklin M, Dawoud T, Ameen F, et al. Synthesis of highly active biocompatible ZrO2 nanorods using a bioextract. Ceramics International 2020;46:25915–20. https://doi.org/10.1016/j.ceramint.2020.07.076.
[93] Xu H, Qin D-H, Yang Z, et al. Fabrication and characterization of highly ordered zirconia nanowire arrays by sol–gel template method. Materials Chemistry and Physics 2003;80:524–8. https://doi.org/10.1016/S0254-0584(03)00002-6.
[94] Li K, Wang S-L, Li H-J, et al. Microstructure and growth mechanism of ZrO2 nanorod network via oxyacetylene torch ablation. Materials Letters 2014;123:217–20. https://doi.org/10.1016/j.matlet.2014.03.012.
[95] Baek MK, Park SJ, Choi DJ. Synthesis of zirconia (ZrO2) nanowires via chemical vapor deposition. Journal of Crystal Growth 2017;459:198–202. https://doi.org/10.1016/j.jcrysgro.2016.12.033.
[96] Chen Y, Gu J, Zhu S, et al. Synthesis of naturally cross-linked polycrystalline ZrO2 hollow nanowires using butterfly as templates. Materials Chemistry and Physics 2012;134:16–20. https://doi.org/10.1016/j.matchemphys.2012.02.064.
[97] Ali U, Karim KJBtA, Buang NA. A Review of the Properties and Applications of Poly (Methyl Methacrylate) (PMMA). Polymer Reviews 2015;55:678–705. https://doi.org/10.1080/15583724.2015.1031377.
[98] Lee W-J, Smyrl WH. Zirconium Oxide Nanotubes Synthesized via Direct Electrochemical Anodization. Electrochemical and Solid-State Letters 2005;8:B7. https://doi.org/10.1149/1.1857115.
[99] Tański T, Smok W, Matysiak W. Characterization of morphology and optical properties of SnO_2 nanowires prepared by electrospinning. Bulletin of the Polish Academy of

Sciences Technical Sciences 2021:137507–137507. https://doi.org/10.24425/bpasts.2021.137507.
[100] Xu Z, Wang F, Yin X, et al. Recent advances in ZrO2 nanofibers: From structural design to emerging applications. Science China Materials 2023;66:421–40. https://doi.org/10.1007/s40843-022-2245-y.
[101] Wang H, Lin S, Yang S, et al. High-Temperature Particulate Matter Filtration with Resilient Yttria-Stabilized ZrO 2 Nanofiber Sponge. Small 2018;14. https://doi.org/10.1002/smll.201800258.
[102] Chen S, Chen Y, Zhao Y, et al. Status and strategies for fabricating flexible oxide ceramic micro-nanofiber materials. Materials Today 2022;61:139–68. https://doi.org/10.1016/j.mattod.2022.11.004.
[103] Balinova YuA, Varrik NM, Istomin A V., et al. Electrospinning of Zirconia Fibers. Glass and Ceramics 2020;77:313–7. https://doi.org/10.1007/s10717-020-00296-3.
[104] Wang Y, Li Z, Fu W, et al. Core–Sheath CeO2/SiO2 Nanofibers as Nanoreactors for Stabilizing Sinter-Resistant Pt, Enhanced Catalytic Oxidation and Water Remediation. Advanced Fiber Materials 2022;4:1278–89. https://doi.org/10.1007/s42765-022-00177-0.
[105] Xia J, Guo H, Cheng M, et al. Electrospun zirconia nanofibers for enhancing the electrochemical synthesis of ammonia by artificial nitrogen fixation. Journal of Materials Chemistry A 2021;9:2145–51. https://doi.org/10.1039/D0TA08089F.
[106] Cheng Z, Wang H, Li Z, et al. Processing Nomex Nanofibers by Ionic Solution Blow-Spinning for Efficient High-Temperature Exhausts Treatment. Advanced Fiber Materials 2023;5:497–513. https://doi.org/10.1007/s42765-022-00231-x.
[107] Jing P, Liu M, Wang P, et al. Flexible nonwoven ZrO2 ceramic membrane as an electrochemically stable and flame-resistant separator for high-power rechargeable batteries. Chemical Engineering Journal 2020;388:124259. https://doi.org/10.1016/j.cej.2020.124259.
[108] Dang W, Wang B, Xu Z, et al. Pore structure, thermal insulation and compressive property of ZrO2 nanofiber aerogels with carbon junction fabricated by freeze drying. Journal of Non-Crystalline Solids 2023;600:122031. https://doi.org/10.1016/j.jnoncrysol.2022.122031.
[109] Ding Y, Yang L, Yang M, et al. Optimization of ultralight SiO2/TiO2 nanofibrous aerogel for high-temperature application. Ceramics International 2023;49:38058–69. https://doi.org/10.1016/j.ceramint.2023.09.136.
[110] Zhang X, Lu Y. Centrifugal Spinning: An Alternative Approach to Fabricate Nanofibers at High Speed and Low Cost. Polymer Reviews 2014;54:677–701. https://doi.org/10.1080/15583724.2014.935858.
[111] Zhang X, Wang F, Dou L, et al. Ultrastrong, Superelastic, and Lamellar Multiarch Structured ZrO 2 –Al 2 O 3 Nanofibrous Aerogels with High-Temperature Resistance over 1300 °C. ACS Nano 2020;14:15616–25. https://doi.org/10.1021/acsnano.0c06423.
[112] Li M, Xiao L, Guo P, et al. Resilient and Antipuncturing Si 3 N 4 Nanofiber Sponge. Nano Letters 2023;23:1289–97. https://doi.org/10.1021/acs.nanolett.2c04475.
[113] Peng Y, Xie Y, Wang L, et al. High-temperature flexible, strength and hydrophobic YSZ/SiO2 nanofibrous membranes with excellent thermal insulation. Journal of the European Ceramic Society 2021;41:1471–80. https://doi.org/10.1016/j.jeurceramsoc.2020.09.071.
[114] Jia C, Liu Y, Li L, et al. A Foldable All-Ceramic Air Filter Paper with High Efficiency and High-Temperature Resistance. Nano Letters 2020;20:4993–5000. https://doi.org/10.1021/acs.nanolett.0c01107.

[115] Li L, Jia C, Liu Y, et al. Nanograin–glass dual-phasic, elasto-flexible, fatigue-tolerant, and heat-insulating ceramic sponges at large scales. Materials Today 2022;54:72–82. https://doi.org/10.1016/j.mattod.2022.02.007.
[116] Zhang Y, Liu S, Yan J, et al. Superior Flexibility in Oxide Ceramic Crystal Nanofibers. Advanced Materials 2021;33. https://doi.org/10.1002/adma.202105011.
[117] Li S, Zhang X, Cheng X, et al. Flexible and compressive Al2O3/ZrO2/Y2O3 nanofibrous membranes for thermal insulation at 1400 °C. Composites Communications 2022;35:101290. https://doi.org/10.1016/j.coco.2022.101290.
[118] Wang L, Feng L, Sun Z, et al. Flexible, self-cleaning, and high-performance ceramic nanofiber-based moist-electric generator enabled by interfacial engineering. Science China Technological Sciences 2022;65:450–7. https://doi.org/10.1007/s11431-021-1969-y.
[119] Yekta R, Abedi-Firoozjah R, Azimi Salim S, et al. Application of cellulose and cellulose derivatives in smart/intelligent bio-based food packaging. Cellulose 2023;30:9925–53. https://doi.org/10.1007/s10570-023-05520-1.
[120] Peranidze K, Safronova T V., Kildeeva NR. Electrospun Nanomaterials Based on Cellulose and Its Derivatives for Cell Cultures: Recent Developments and Challenges. Polymers 2023;15:1174. https://doi.org/10.3390/polym15051174.
[121] Shao C, Guan H, Liu Y, et al. A novel method for making ZrO2 nanofibres via an electrospinning technique. Journal of Crystal Growth 2004;267:380–4. https://doi.org/10.1016/j.jcrysgro.2004.03.065.
[122] Azad A-M, Matthews T, Swary J. Processing and characterization of electrospun Y2O3-stabilized ZrO2 (YSZ) and Gd2O3-doped CeO2 (GDC) nanofibers. Materials Science and Engineering: B 2005;123:252–8. https://doi.org/10.1016/j.mseb.2005.08.070.
[123] Formo E, Camargo PHC, Lim B, et al. Functionalization of ZrO2 nanofibers with Pt nanostructures: The effect of surface roughness on nucleation mechanism and morphology control. Chemical Physics Letters 2009;476:56–61. https://doi.org/10.1016/j.cplett.2009.05.075.
[124] Su M, Wang J, Du H, et al. Characterization and humidity sensitivity of electrospun ZrO2:TiO2 hetero-nanofibers with double jets. Sensors and Actuators B: Chemical 2012;161:1038–45. https://doi.org/10.1016/j.snb.2011.12.005.
[125] Abdel-Karim U, Kenawy E-R. Synthesis of zirconia, organic and hybrid nanofibers for reinforcement of polymethyl methacrylate denture base: evaluation of flexural strength and modulus, fracture toughness and impact strength. Tanta Dental Journal 2019;16:12. https://doi.org/10.4103/tdj.tdj_23_18.
[126] Çetinkaya Z, Güneş E, Şavkliyildiz İ. Investigation of biochemical properties of flash sintered ZrO2–SnO2 nanofibers. Materials Chemistry and Physics 2023;293:126900. https://doi.org/10.1016/j.matchemphys.2022.126900.
[127] Sun G-X, Liu F-T, Bi J-Q, et al. Electrospun zirconia nanofibers and corresponding formation mechanism study. Journal of Alloys and Compounds 2015;649:788–92. https://doi.org/10.1016/j.jallcom.2015.03.068.
[128] Li W, Ren Y, Guo Y. ZrO2/ZnO nanocomposite materials for chemiresistive butanol sensors. Sensors and Actuators B: Chemical 2020;308:127658. https://doi.org/10.1016/j.snb.2020.127658.
[129] Yasin AS, Obaid M, El-Newehy MH, et al. Influence of TixZr(1−x)O2 nanofibers composition on the photocatalytic activity toward organic pollutants degradation and water splitting. Ceramics International 2015;41:11876–85. https://doi.org/10.1016/j.ceramint.2015.05.156.

[130] Yu G, Zhu L, Zhang G, et al. Preparation and characterization of the continuous titanium-doped ZrO2 mesoporous fibers with large surface area. Journal of Porous Materials 2014;21:105–12. https://doi.org/10.1007/s10934-013-9753-8.
[131] Song J, Wang X, Yan J, et al. Soft Zr-doped TiO2 Nanofibrous Membranes with Enhanced Photocatalytic Activity for Water Purification. Scientific Reports 2017;7:1636. https://doi.org/10.1038/s41598-017-01969-w.
[132] Barakat NAM, Hassan AAY, Matar SME-S, et al. ZrO 2 /TiO 2 nanofiber catalyst for effective liquefaction of agricultural wastes in subcritical methanol. Separation Science and Technology 2018;53:2628–38. https://doi.org/10.1080/01496395.2018.1458876.
[133] Rodaev V V., Razlivalova SS, Zhigachev AO, et al. Preparation of Zirconia Nanofibers by Electrospinning and Calcination with Zirconium Acetylacetonate as Precursor. Polymers 2019;11:1067. https://doi.org/10.3390/polym11061067.
[134] Li Y, He J-H. Fabrication and characterization of ZrO 2 nanofibers by critical bubble electrospinning for high-temperature-resistant adsorption and separation. Adsorption Science & Technology 2019;37:425–37. https://doi.org/10.1177/0263617419828268.
[135] Huang Q, He J, Lin Z, et al. Physical and chemical properties of an antimicrobial Bis-GMA free dental resin with quaternary ammonium dimethacrylate monomer. Journal of the Mechanical Behavior of Biomedical Materials 2016;56:68–76. https://doi.org/10.1016/j.jmbbm.2015.10.028.
[136] Walters NJ, Xia W, Salih V, et al. Poly(propylene glycol) and urethane dimethacrylates improve conversion of dental composites and reveal complexity of cytocompatibility testing. Dental Materials 2016;32:264–77. https://doi.org/10.1016/j.dental.2015.11.017.
[137] Saen P, Atai M, Nodehi A, et al. Physical characterization of unfilled and nanofilled dental resins: Static versus dynamic mechanical properties. Dental Materials 2016;32:e185–97. https://doi.org/10.1016/j.dental.2016.06.001.
[138] Chen Q, Zhao Y, Wu W, et al. Fabrication and evaluation of Bis-GMA/TEGDMA dental resins/composites containing halloysite nanotubes. Dental Materials 2012;28:1071–9. https://doi.org/10.1016/j.dental.2012.06.007.
[139] Yang Q, Lin Y-H, Li M, et al. Characterization of mesoporous silica nanoparticle composites at low filler content. Journal of Composite Materials 2016;50:715–22. https://doi.org/10.1177/0021998315580830.
[140] Miao X, Li Y, Zhang Q, et al. Low shrinkage light curable dental nanocomposites using SiO2 microspheres as fillers. Materials Science and Engineering: C 2012;32:2115–21. https://doi.org/10.1016/j.msec.2012.05.053.
[141] Zafar M, Najeeb S, Khurshid Z, et al. Potential of Electrospun Nanofibers for Biomedical and Dental Applications. Materials 2016;9:73. https://doi.org/10.3390/ma9020073.
[142] Deitzel JM, Kleinmeyer J, Harris D, et al. The effect of processing variables on the morphology of electrospun nanofibers and textiles. Polymer 2001;42:261–72. https://doi.org/10.1016/S0032-3861(00)00250-0.
[143] Zhang X, Reagan MR, Kaplan DL. Electrospun silk biomaterial scaffolds for regenerative medicine. Advanced Drug Delivery Reviews 2009;61:988–1006. https://doi.org/10.1016/j.addr.2009.07.005.
[144] Li D, Wang Y, Xia Y. Electrospinning of Polymeric and Ceramic Nanofibers as Uniaxially Aligned Arrays. Nano Letters 2003;3:1167–71. https://doi.org/10.1021/nl0344256.
[145] Subbiah T, Bhat GS, Tock RW, et al. Electrospinning of nanofibers. Journal of Applied Polymer Science 2005;96:557–69. https://doi.org/10.1002/app.21481.

[146] Dersch R, Liu T, Schaper AK, et al. Electrospun nanofibers: Internal structure and intrinsic orientation. Journal of Polymer Science Part A: Polymer Chemistry 2003;41:545–53. https://doi.org/10.1002/pola.10609.
[147] Meechaisue C, Wutticharoenmongkol P, Waraput R, et al. Preparation of electrospun silk fibroin fiber mats as bone scaffolds: a preliminary study. Biomedical Materials 2007;2:181–8. https://doi.org/10.1088/1748-6041/2/3/003.
[148] Chronakis IS. Novel nanocomposites and nanoceramics based on polymer nanofibers using electrospinning process—A review. Journal of Materials Processing Technology 2005;167:283–93. https://doi.org/10.1016/j.jmatprotec.2005.06.053.
[149] Fong H, Chun I, Reneker DH. Beaded nanofibers formed during electrospinning. Polymer 1999;40:4585–92. https://doi.org/10.1016/S0032-3861(99)00068-3.
[150] Garg K, Bowlin GL. Electrospinning jets and nanofibrous structures. Biomicrofluidics 2011;5. https://doi.org/10.1063/1.3567097.
[151] Megelski S, Stephens JS, Chase DB, et al. Micro- and Nanostructured Surface Morphology on Electrospun Polymer Fibers. Macromolecules 2002;35:8456–66. https://doi.org/10.1021/ma020444a.
[152] Tong HW, Wang M. Effects of Processing Parameters on the Morphology and Size of Electrospun PHBV Micro- and Nano-Fibers. Key Engineering Materials 2007;334–335:1233–6. https://doi.org/10.4028/www.scientific.net/KEM.334-335.1233.
[153] Macossay J, Marruffo A, Rincon R, et al. Effect of needle diameter on nanofiber diameter and thermal properties of electrospun poly(methyl methacrylate). Polymers for Advanced Technologies 2007;18:180–3. https://doi.org/10.1002/pat.844.
[154] Zong X, Kim K, Fang D, et al. Structure and process relationship of electrospun bioabsorbable nanofiber membranes. Polymer 2002;43:4403–12. https://doi.org/10.1016/S0032-3861(02)00275-6.
[155] Jung YH, Kim HY, Lee DR, et al. Characterization of PVOH nonwoven mats prepared from Surfactant-Polymer system via electrospinning. Macromolecular Research 2005;13:385–90. https://doi.org/10.1007/BF03218470.
[156] Sill TJ, von Recum HA. Electrospinning: Applications in drug delivery and tissue engineering. Biomaterials 2008;29:1989–2006. https://doi.org/10.1016/j.biomaterials.2008.01.011.
[157] Pillay V, Dott C, Choonara YE, et al. A Review of the Effect of Processing Variables on the Fabrication of Electrospun Nanofibers for Drug Delivery Applications. Journal of Nanomaterials 2013;2013:1–22. https://doi.org/10.1155/2013/789289.
[158] Lannutti J, Reneker D, Ma T, et al. Electrospinning for tissue engineering scaffolds. Materials Science and Engineering: C 2007;27:504–9. https://doi.org/10.1016/j.msec.2006.05.019.
[159] Bottino MC, Kamocki K, Yassen GH, et al. Bioactive Nanofibrous Scaffolds for Regenerative Endodontics. Journal of Dental Research 2013;92:963–9. https://doi.org/10.1177/0022034513505770.
[160] Dodda JM, Azar MG, Bělský P, et al. Bioresorbable films of polycaprolactone blended with poly(lactic acid) or poly(lactic-co-glycolic acid). International Journal of Biological Macromolecules 2023;248:126654. https://doi.org/10.1016/j.ijbiomac.2023.126654.
[161] Xue J, Wu T, Dai Y, et al. Electrospinning and Electrospun Nanofibers: Methods, Materials, and Applications. Chemical Reviews 2019;119:5298–415. https://doi.org/10.1021/acs.chemrev.8b00593.
[162] Ding Z, Li X. Electrospun Nanofibers for Biomedical Applications. Electrospinning, Wiley; 2024, p. 317–37. https://doi.org/10.1002/9783527841479.ch18.

[163] Chen S, Li R, Li X, et al. Electrospinning: An enabling nanotechnology platform for drug delivery and regenerative medicine. Advanced Drug Delivery Reviews 2018;132:188–213. https://doi.org/10.1016/j.addr.2018.05.001.
[164] Wang X, Cai Q, Zhang X, et al. Improved performance of Bis-GMA/TEGDMA dental composites by net-like structures formed from SiO 2 nanofiber fillers. Materials Science and Engineering: C 2016;59:464–70. https://doi.org/10.1016/j.msec.2015.10.044.
[165] Amiri P, Talebi Z, Semnani D, et al. Improved performance of Bis-GMA dental composites reinforced with surface-modified PAN nanofibers. Journal of Materials Science: Materials in Medicine 2021;32:82. https://doi.org/10.1007/s10856-021-06557-z.
[166] Han M-K. Advances and challenges in zirconia-based materials for dental applications. Journal of the Korean Ceramic Society 2024;61:783–99. https://doi.org/10.1007/s43207-024-00416-7.
[167] Denry I, Kelly JR. State of the art of zirconia for dental applications. Dental Materials 2008;24:299–307. https://doi.org/10.1016/j.dental.2007.05.007.
[168] Wang J, Li J, Li Y, et al. One-step synthesis and low-temperature rapid sintering of alumina-zirconia ceramics by flash sintering combined with phase transformation. Materials Characterization 2024;209:113771. https://doi.org/10.1016/j.matchar.2024.113771.
[169] Kurihara A, Nakamura K, Shishido S, et al. Mechanism underlying ultraviolet-irradiation-induced discoloration of dental zirconia ceramics stabilized with 3 and 5 mol% yttria. Ceramics International 2024;50:12136–45. https://doi.org/10.1016/j.ceramint.2024.01.117.
[170] Prati C, Gandolfi MG. Calcium silicate bioactive cements: Biological perspectives and clinical applications. Dental Materials 2015;31:351–70. https://doi.org/10.1016/j.dental.2015.01.004.
[171] Leprince JG, Palin WM, Hadis MA, et al. Progress in dimethacrylate-based dental composite technology and curing efficiency. Dental Materials 2013;29:139–56. https://doi.org/10.1016/j.dental.2012.11.005.
[172] Ferracane JL, Hilton TJ, Stansbury JW, et al. Academy of Dental Materials guidance—Resin composites: Part II—Technique sensitivity (handling, polymerization, dimensional changes). Dental Materials 2017;33:1171–91. https://doi.org/10.1016/j.dental.2017.08.188.
[173] Ilie N, Hilton TJ, Heintze SD, et al. Academy of Dental Materials guidance—Resin composites: Part I—Mechanical properties. Dental Materials 2017;33:880–94. https://doi.org/10.1016/j.dental.2017.04.013.
[174] Aminoroaya A, Esmaeely Neisiany R, Nouri Khorasani S, et al. A Review of Dental Composites: Methods of Characterizations. ACS Biomaterials Science & Engineering 2020;6:3713–44. https://doi.org/10.1021/acsbiomaterials.0c00051.
[175] Barszczewska-Rybarek IM. Characterization of urethane-dimethacrylate derivatives as alternative monomers for the restorative composite matrix. Dental Materials 2014;30:1336–44. https://doi.org/10.1016/j.dental.2014.09.008.
[176] Tokar N, Tokar E, Mavis B, et al. Evaluation of Mechanical Properties of Various Nanofiber Reinforced BisGMA/TEGDMA Bbased Dental Composite Resins. West Indian Medical Journal 2016. https://doi.org/10.7727/wimj.2016.243.
[177] Li Y, Shi J, Li C, et al. Synergistic improvement of strength and toughness of zirconia ceramics by introducing zirconia nanofibers. Journal of Alloys and Compounds 2026;1056:186592. https://doi.org/10.1016/j.jallcom.2026.186592.

[178] Stern T, Marom G. Fracture Mechanisms and Toughness in Polymer Nanocomposites: A Brief Review. Journal of Composites Science 2024;8:395. https://doi.org/10.3390/jcs8100395.
[179] Alshabib A, Silikas N, Watts DC. Hardness and fracture toughness of resin-composite materials with and without fibers. Dental Materials 2019;35:1194–203. https://doi.org/10.1016/j.dental.2019.05.017.
[180] Meng Q, Wang Z. Theoretical analysis of interfacial debonding and fiber pull-out in fiber-reinforced polymer-matrix composites. Archive of Applied Mechanics 2015;85:745–59. https://doi.org/10.1007/s00419-015-0987-6.
[181] Fu S-Y, Feng X-Q, Lauke B, et al. Effects of particle size, particle/matrix interface adhesion and particle loading on mechanical properties of particulate–polymer composites. Composites Part B: Engineering 2008;39:933–61. https://doi.org/10.1016/j.compositesb.2008.01.002.
[182] Noworyta M, Topa-Skwarczyńska M, Jamróz P, et al. Influence of the Type of Nanofillers on the Properties of Composites Used in Dentistry and 3D Printing. International Journal of Molecular Sciences 2023;24:10549. https://doi.org/10.3390/ijms241310549.
[183] Mair LH, Stolarski TA, Vowles RW, et al. Wear: mechanisms, manifestations and measurement. Report of a workshop. Journal of Dentistry 1996;24:141–8. https://doi.org/10.1016/0300-5712(95)00043-7.
[184] Tsujimoto A, Barkmeier WW, Fischer NG, et al. Wear of resin composites: Current insights into underlying mechanisms, evaluation methods and influential factors. Japanese Dental Science Review 2018;54:76–87. https://doi.org/10.1016/j.jdsr.2017.11.002.
[185] Morresi AL, D'Amario M, Capogreco M, et al. Thermal cycling for restorative materials: Does a standardized protocol exist in laboratory testing? A literature review. Journal of the Mechanical Behavior of Biomedical Materials 2014;29:295–308. https://doi.org/10.1016/j.jmbbm.2013.09.013.
[186] Gale MS, Darvell BW. Thermal cycling procedures for laboratory testing of dental restorations. Journal of Dentistry 1999;27:89–99. https://doi.org/10.1016/S0300-5712(98)00037-2.
[187] Zhang J, Yang Y, Chen Y, et al. A review of new generation of dental restorative resin composites with antibacterial, remineralizing and self-healing capabilities. Discover Nano 2024;19:189. https://doi.org/10.1186/s11671-024-04151-0.
[188] Sideridou ID, Karabela MM. Effect of the amount of 3-methacyloxypropyltrimethoxysilane coupling agent on physical properties of dental resin nanocomposites. Dental Materials 2009;25:1315–24. https://doi.org/10.1016/j.dental.2009.03.016.
[189] Miyazaki CL, Medeiros IS, Matos J do R, et al. Thermal characterization of dental composites by TG/DTG and DSC. Journal of Thermal Analysis and Calorimetry 2010;102:361–7. https://doi.org/10.1007/s10973-010-0739-3.
[190] Syed Asif SA, Wahl KJ, Colton RJ, et al. Quantitative imaging of nanoscale mechanical properties using hybrid nanoindentation and force modulation. Journal of Applied Physics 2001;90:1192–200. https://doi.org/10.1063/1.1380218.
[191] Sideridou ID, Karabela MM, Vouvoudi ECh. Dynamic thermomechanical properties and sorption characteristics of two commercial light cured dental resin composites. Dental Materials 2008;24:737–43. https://doi.org/10.1016/j.dental.2007.08.004.
[192] Sideridou I, Tserki V, Papanastasiou G. Effect of chemical structure on degree of conversion in light-cured dimethacrylate-based dental resins. Biomaterials 2002;23:1819–29. https://doi.org/10.1016/S0142-9612(01)00308-8.

[193] R E Dinnebier. Powder Diffraction: Theory and Practice. Illustrate. Royal Society of Chemistry; 2008.
[194] Perdigão J, Zatt FP, Lopes GC, et al. Characterization of Universal Composite Resin Filler Particles. Journal of Esthetic and Restorative Dentistry 2025;37:2472–80. https://doi.org/10.1111/jerd.70009.
[195] Bustamante-Torres M, Romero-Fierro D, Arcentales-Vera B, et al. Interaction between Filler and Polymeric Matrix in Nanocomposites: Magnetic Approach and Applications. Polymers 2021;13:2998. https://doi.org/10.3390/polym13172998.
[196] Hajdu AI, Dumitrescu R, Balean O, et al. Microscopic and Color Changes in Direct Dental Restorative Composite Resins upon Immersion in Beverages: Characterization by Scanning Electron Microscopy (SEM) and Energy-Dispersive X-ray Spectroscopy (EDS). Biomedicines 2024;12:1740. https://doi.org/10.3390/biomedicines12081740.
[197] Butera A, Pascadopoli M, Gallo S, et al. SEM/EDS Evaluation of the Mineral Deposition on a Polymeric Composite Resin of a Toothpaste Containing Biomimetic Zn-Carbonate Hydroxyapatite (microRepair®) in Oral Environment: A Randomized Clinical Trial. Polymers 2021;13:2740. https://doi.org/10.3390/polym13162740.
[198] Paqué PN, Özcan M. A Review on Biocompatibility of Dental Restorative and Reconstruction Materials. Current Oral Health Reports 2024;11:68–77. https://doi.org/10.1007/s40496-023-00358-9.
[199] Williams DF. On the mechanisms of biocompatibility. Biomaterials 2008;29:2941–53. https://doi.org/10.1016/j.biomaterials.2008.04.023.
[200] Mosmann T. Rapid colorimetric assay for cellular growth and survival: Application to proliferation and cytotoxicity assays. Journal of Immunological Methods 1983;65:55–63. https://doi.org/10.1016/0022-1759(83)90303-4.
[201] Geurtsen W. Biocompatibility of Resin-Modified Filling Materials. Critical Reviews in Oral Biology & Medicine 2000;11:333–55. https://doi.org/10.1177/10454411000110030401.
[202] El-Morsy MT, Khafaga DSR, Diab AH, et al. Recent advancements in multifunctional nanomaterials for dental applications. RSC Advances 2025;15:49009–29. https://doi.org/10.1039/D5RA07176C.
[203] Fariñas JC. Microwave-assisted hydrothermal synthesis of nanocrystalline zirconia. Boletín de La Sociedad Española de Cerámica y Vidrio 2025;64:100445. https://doi.org/10.1016/j.bsecv.2025.100445.
[204] Portillo FRL, Urias AEV, Arredondo TG, et al. Electrospun nanofibers and their potential in dental applications: an updated review. International Surgery Journal 2025. https://doi.org/10.18203/2349-2902.isj20251413.
[205] Gamoudi H, Stajcic I, Stojanovic D, et al. Mechanical reinforcement of polyetherimide with electrospun zirconia nanofibers. Science of Sintering 2025:39–39. https://doi.org/10.2298/SOS250924039G.
[206] Machatschek R, Heuchel M, Lendlein A. Hydrolytic stability of polyetherimide investigated in ultrathin films. Journal of Materials Research 2021;36:2987–94. https://doi.org/10.1557/s43578-021-00267-6.
[207] Omiyale BO, Ogbeyemi A, Rasheed AA, et al. Influence of electrospinning parameters on the development of high-quality electrospun nanofibers: A brief critical assessment. Next Nanotechnology 2025;8:100295. https://doi.org/10.1016/j.nxnano.2025.100295.
[208] ISO 10993-1:2020. Biological evaluation of medical devices — Part 1: Evaluation and testing within a risk management process. 2020.
[209] Saligheh O, Khajavi R, Yazdanshenas ME, et al. Production and Characterization of Zirconia (ZrO_2) Ceramic Nanofibers by Using Electrospun Poly(Vinyl

Alcohol)/Zirconium Acetate Nanofibers as a Precursor. Journal of Macromolecular Science, Part B 2016;55:605–16. https://doi.org/10.1080/00222348.2016.1179165.
[210] Reinders L, Pfeifer S, Kröner S, et al. Development of mullite fibers and novel zirconia-toughened mullite fibers for high temperature applications. Journal of the European Ceramic Society 2021;41:3570–80. https://doi.org/10.1016/j.jeurceramsoc.2020.12.048.
[211] Jayakumar S, Ananthapadmanabhan PV, Perumal K, et al. Characterization of nano-crystalline ZrO2 synthesized via reactive plasma processing. Materials Science and Engineering: B 2011;176:894–9. https://doi.org/10.1016/j.mseb.2011.05.013.
[212] Kumari L, Li W, Wang D. Monoclinic zirconium oxide nanostructures synthesized by a hydrothermal route. Nanotechnology 2008;19:195602. https://doi.org/10.1088/0957-4484/19/19/195602.
[213] Liu D, Gao Y, Liu J, et al. SiC whisker reinforced ZrO 2 composites prepared by flash-sintering. Journal of the European Ceramic Society 2016;36:2051–5. https://doi.org/10.1016/j.jeurceramsoc.2016.02.014.
[214] Zhao W, Su Y, Wang D. Synergetic effects of interfacial and spatial confinement in polymer nanocomposites. Mod Phys Lett B 2017;31:1730003. https://doi.org/10.1142/S0217984917300034.
[215] Rodaev VV, Zhigachev AO, Korenkov VV, et al. The influence of zirconia precursor/binding polymer mass ratio in the intermediate electrospun composite fibers on the phase transformation of final zirconia nanofibers. Physica Status Solidi (a) 2016;213:2352–5. https://doi.org/10.1002/pssa.201600047.
[216] Sharma SK, Sudarshan K, Pujari PK. Unraveling the sub-nanoscopic structure at interphase in a poly(vinyl alcohol)–MOF nanocomposite, and its role in thermo-mechanical properties. Phys Chem Chem Phys 2016;18:25434–42. https://doi.org/10.1039/C6CP04872B.
[217] Rovira JJR, Piqué EJ, Anglada Gomila MJ. Nanoindentation of Advanced Ceramics: Applications to ZrO_2 Materials. In: Tiwari A, Natarajan S, editors. Applied Nanoindentation in Advanced Materials. 1st ed., Wiley; 2017, p. 459–80. https://doi.org/10.1002/9781119084501.ch19.
[218] Sarker SD, Nahar L. Characterization of nanoparticles. Advances in Nanotechnology-Based Drug Delivery Systems, Elsevier; 2022, p. 45–82. https://doi.org/10.1016/B978-0-323-88450-1.00011-9.
[219] Saini BS, Kaur R. X-ray diffraction. Handbook of Modern Coating Technologies, Elsevier; 2021, p. 85–141. https://doi.org/10.1016/B978-0-444-63239-5.00003-2.
[220] Herrmann V, Unseld K, Fuchs H-B. The scale behavior of fillers in elastomers by means of indentation tests. Colloid Polym Sci 2002;280:267–73. https://doi.org/10.1007/s00396-001-0605-8.
[221] Sonika, Kumar Verma S, Sharma G, et al. Interfacial interaction of controlled poly(ether-imide) (PEI) - titanium dioxide-based nanocomposites. Materials Today: Proceedings 2024;106:134–8. https://doi.org/10.1016/j.matpr.2023.07.353.
[222] Takkalkar P, Nizamuddin S, Griffin G, et al. Thermal Properties of Sustainable Thermoplastics Nanocomposites Containing Nanofillers and Its Recycling Perspective. In: Inamuddin, Thomas S, Kumar Mishra R, et al., editors. Sustainable Polymer Composites and Nanocomposites, Cham: Springer International Publishing; 2019, p. 915–33. https://doi.org/10.1007/978-3-030-05399-4_31.
[223] Zhao B, Liu Q, Tang G, et al. Microstructure and Biocompatibility of Graphene Oxide/BCZT Composite Ceramics via Fast Hot-Pressed Sintering. Coatings 2024;14:689. https://doi.org/10.3390/coatings14060689.

[224] Moradi R, Vaseghi M, Sohrabian M, et al. Optimized bioactive glass/PLA nanocomposites for bone tissue engineering: balancing mechanical strength and biodegradability. International Journal of Polymeric Materials and Polymeric Biomaterials 2025;74:1596–609. https://doi.org/10.1080/00914037.2025.2477164.
[225] Tolosa L, Donato MT, Gómez-Lechón MJ. General Cytotoxicity Assessment by Means of the MTT Assay. In: Vinken M, Rogiers V, editors. Protocols in In Vitro Hepatocyte Research, vol. 1250, New York, NY: Springer New York; 2015, p. 333–48. https://doi.org/10.1007/978-1-4939-2074-7_26.
[226] Essmeister J, Taublaender MJ, Koch T, et al. High modulus polyimide particle-reinforcement of epoxy composites. Mater Adv 2021;2:2278–88. https://doi.org/10.1039/D0MA00980F.
[227] Serra-Gómez R, González-Gaitano G, González-Benito J. Composites based on EVA and barium titanate submicrometric particles: Preparation by high-energy ball milling and characterization. Polymer Composites 2012;33:1549–56. https://doi.org/10.1002/pc.22291.
[228] Arandiyan H, S. Mofarah S, Sorrell CC, et al. Defect engineering of oxide perovskites for catalysis and energy storage: synthesis of chemistry and materials science. Chem Soc Rev 2021;50:10116–211. https://doi.org/10.1039/D0CS00639D.
[229] Ricca C, Aschauer U. Mechanisms for point defect-induced functionality in complex perovskite oxides. Appl Phys A 2022;128:1083. https://doi.org/10.1007/s00339-022-06210-8.

Biography

Houda Ali Madani Gamoudi was born on February 12, 1982 in Tripoli, Libya. She completed her undergraduate studies in 2006 at the University of Tripoli, Libya, Department of Dentistry. She completed her Master's studies at the University of Belgrade, Faculty of Technology and Metallurgy, study program Materials Engineering, in 2021. She enrolled in her doctoral studies in 2022 at the University of Belgrade, Faculty of Technology and Metallurgy, study program Materials Engineering. Since 2007, she has been employed at the General Hospital in Tripoli, Libya.

Biografija

Houda Ali Madani Gamoudi rođena je 12. februara 1982. godine u Tripoliju, Libija. Osnovne akademske studije je završila 2006. godine na Univerzitetu u Tripoliju, Libija, Departman za stomatologiju. Master akademske studije na Univerzitetu u Beogradu, Tehnološko-metalurški fakultet, studijski program Inženjerstvo materijala, završila je 2021. godine. Doktorske akademske studije upisala je 2022. godine na Univerzitetu u Beogradu, Tehnološko-metalurški fakultet, studijski program Inženjerstvo materijala. Od 2007. godine zaposlena je u Opštoj bolnici u Tripoliju, Libija.

Изјава о ауторству

Име и презиме аутора ___Houda Ali Madani Gamoudi_____
Број индекса _____2022/4031_____

Изјављујем

да је докторска дисертација под насловом

Синтеза и карактеризација денталних композитних имплантата са ојачањима на бази цирконијума

Synthesis and characterization of dental composite implants with zirconium-based reinforcements

- резултат сопственог истраживачког рада;
- да дисертација у целини ни у деловима није била предложена за стицање друге дипломе према студијским програмима других високошколских установа;
- да су резултати коректно наведени и
- да нисам кршио/ла ауторска права и користио/ла интелектуалну својину других лица.

Потпис аутора

Београду, ___04.05.2026.___

_____

Изјава о истоветности штампане и електронске верзије докторског рада

Име и презиме аутора _____Houda Ali Madani Gamoudi_____
Број индекса ____2022/4031_____
Студијски програм _Инжењерство материјала_____
Наслов рада Синтеза и карактеризација денталних композитних имплантата са ојачањима на бази цирконијума

Synthesis and characterization of dental composite implants with zirconium-based reinforcements

Ментори ____Весна Радојевић_____
____Ивана Стајчић_____

Изјављујем да је штампана верзија мог докторског рада истоветна електронској верзији коју сам предао/ла ради похрањена у **Дигиталном репозиторијуму Универзитета у Београду.**
Дозвољавам да се објаве моји лични подаци везани за добијање академског назива доктора наука, као што су име и презиме, година и место рођења и датум одбране рада.
Ови лични подаци могу се објавити на мрежним страницама дигиталне библиотеке, у електронском каталогу и у публикацијама Универзитета у Београду.

Потпис аутора

У Београду, ___04.05.2026.___

_____

Изјава о коришћењу

Овлашћујем Универзитетску библиотеку „Светозар Марковић“ да у Дигитални репозиторијум Универзитета у Београду унесе моју докторску дисертацију под насловом:

Синтеза и карактеризација денталних композитних имплантата са ојачањима на бази цирконијума

Synthesis and characterization of dental composite implants with zirconium-based reinforcements

која је моје ауторско дело.
Дисертацију са свим прилозима предао/ла сам у електронском формату погодном за трајно архивирање.
Моју докторску дисертацију похрањену у Дигиталном репозиторијуму Универзитета у Београду и доступну у отвореном приступу могу да користе сви који поштују одредбе садржане у одабраном типу лиценце Креативне заједнице (Creative Commons) за коју сам се одлучио/ла.

1. Ауторство (CC BY)
2. Ауторство – некомерцијално (CC BY-NC)
(3). Ауторство – некомерцијално – без прерада (CC BY-NC-ND)
4. Ауторство – некомерцијално – делити под истим условима (CC BY-NC-SA)
5. Ауторство – без прерада (CC BY-ND)
6. Ауторство – делити под истим условима (CC BY-SA)

(Молимо да заокружите само једну од шест понуђених лиценци.
Кратак опис лиценци је саставни део ове изјаве).

Потпис аутора

У Београду, ___04.05.2026.___

_____

1. **Ауторство**. Дозвољавате умножавање, дистрибуцију и јавно саопштавање дела, и прераде, ако се наведе име аутора на начин одређен од стране аутора или даваоца лиценце, чак и у комерцијалне сврхе. Ово је најслободнија од свих лиценци.
2. **Ауторство – некомерцијално**. Дозвољавате умножавање, дистрибуцију и јавно саопштавање дела, и прераде, ако се наведе име аутора на начин одређен од стране аутора или даваоца лиценце. Ова лиценца не дозвољава комерцијалну употребу дела.
3. **Ауторство – некомерцијално – без прерада**. Дозвољавате умножавање, дистрибуцију и јавно саопштавање дела, без промена, преобликовања или употребе дела у свом делу, ако се наведе име аутора на начин одређен од стране аутора или даваоца лиценце. Ова лиценца не дозвољава комерцијалну употребу дела. У односу на све остале лиценце, овом лиценцом се ограничава највећи обим права коришћења дела.
4. **Ауторство – некомерцијално – делити под истим условима**. Дозвољавате умножавање, дистрибуцију и јавно саопштавање дела, и прераде, ако се наведе име аутора на начин одређен од стране аутора или даваоца лиценце и ако се прерада дистрибуира под истом или сличном лиценцом. Ова лиценца не дозвољава комерцијалну употребу дела и прерада.
5. **Ауторство – без прерада**. Дозвољавате умножавање, дистрибуцију и јавно саопштавање дела, без промена, преобликовања или употребе дела у свом делу, ако се наведе име аутора на начин одређен од стране аутора или даваоца лиценце. Ова лиценца дозвољава комерцијалну употребу дела.
6. **Ауторство – делити под истим условима**. Дозвољавате умножавање, дистрибуцију и јавно саопштавање дела, и прераде, ако се наведе име аутора на начин одређен од стране аутора или даваоца лиценце и ако се прерада дистрибуира под истом или сличном лиценцом. Ова лиценца дозвољава комерцијалну употребу дела и прерада. Слична је софтверским лиценцама, односно лиценцама отвореног кода.